



**Politecnico
di Torino**

Politecnico di Torino

Corso di Laurea in INGEGNERIA ENERGETICA E NUCLEARE

A.a. 2021/2022

Sessione di Laurea Marzo 2022

Multiphysics Modelling and experimental analysis of low temperature electrolysis

Relatori:

prof. Massimo Santarelli
Mohsen Mansourkiaei

Candidati:

Roberto Ruggeri

Ringraziamenti

Ringrazio la mia famiglia e i miei amici per essermi stati vicini durante questo periodo di studi.

Ringraziamenti speciali per il Professore Massimo Santarelli che mi ha permesso di svolgere la tesi in uno dei settori che preferisco, e al mio supervisore Mohsen Mansourkiaei che mi ha supportato durante lo svolgimento di questo lavoro.

Abstract

The main cause of climate change is the combustion of fossil fuels such as coal and natural gas, which emit greenhouse gases into the atmosphere. To counteract this phenomenon, there is a need for a green transition, in which renewable energies and related energy storage systems play the leading role. In this perspective, green hydrogen, i.e. hydrogen produced through electrolysis, using electricity from renewable sources, is certainly an important resource. Electrolysis can be done in an electrolyser which consists of an electrochemical cell capable of producing hydrogen through feeding of current, and water, from which the hydrogen is drawn. Among the electrolysers, one of the most interesting from the point of view of research is Proton Exchange Membrane Electrolysers Cell (PEMEC), which has a membrane capable of conducting ions. In this work, after a deep review of the electrolysis reaction and the major electrolysers on the market, the production of hydrogen is studied through two approaches, experimental and modelling. The experimental approach involves a series of experiments carried out during my internship at Environment Park on a PEMEC electrolyser which consist of preliminary tests on the polarization of the cell and degradation tests. The modelling approach concerns the development and validation of a model of the cell used in the experiments in COMSOL Multiphysics, where 2D and 3D models are developed. The results achieved in the experiments consist in the polarization curves of the cell, with different configurations of temperature, pressure, mass flows and comparison of open and closed cathode configurations, and for what regards the degradation tests, in the monitoring of voltage, pressure and temperature with focus on the production of hydrogen throughout all duration of the experiment. The outcomes obtained in COMSOL Multiphysics concern the validation of the results accomplished in the polarization tests and the application of turbulent and multiphase models at both 2D and 3D configurations. Possible future developments of this work, with regard to improvements in the experimental side, are building an automatic refilling system, to avoid having manual refills during long degradation tests as well as having a system to control and monitor the pressure in the connection between mass spectrometer and the rig, to avoid high pressures that cause an interruption of the scan with relative loss of data until a new scan is manually performed. Regarding the modelling side, a possible improvement is the deepening of the turbulent motion applied to 2D and 3D models, in order to have a better understanding of the multiphase processes that are present in the cell.

Contents

Introduction	10
1 Literature Review	14
1.1 Hydrogen production	14
1.2 Water Electrolysis Technologies Comparison	16
<i>1.2.1 Alkaline water electrolysis</i>	17
<i>1.2.2 Solid oxide electrolysis</i>	18
<i>1.2.3 Proton exchange membrane water electrolysis</i>	19
1.3 PEM Water electrolysis	20
<i>1.3.1 Activation overpotential</i>	22
<i>1.3.2 Mass transport overpotential</i>	23
<i>1.3.3 Ohmic and ionic transport overpotential</i>	24
<i>1.3.4 Polarization Curve</i>	26
1.4 State of the art	27
<i>1.4.1 Membrane electrode assemblies</i>	27
<i>1.4.2 Current collectors</i>	28
<i>1.4.3 Separator plates</i>	28
<i>1.4.4 Hydrogen evolution process electrocatalysts</i>	29
<i>1.4.5 Oxygen evolution process electrocatalysts</i>	29
1.5 Turbulent Dispersed Multiphase Flow in PEM water electrolyzers	30
<i>1.5.1 Turbulent Flow</i>	30
1.5.2 Multiphase flows	31
<i>1.5.3 Two-phase turbulent flow in PEM electrolyser cells</i>	33
2 Experiments	35
2.1 Test Bench and Electrochemical Cell	36
2.2 Mass spectrometer	40
2.3 Experiments performed	46
<i>2.3.1 Polarization test</i>	46
<i>2.3.2 Degradation test</i>	49
<i>2.3.3 Water consumption</i>	57
3 Modelling	58
3.1 Geometry	58
3.2 Mesh	62

3.3 Physics	66
3.3.1 Water Electrolyser	66
3.3.2 Free and Porous Media Flow	72
3.3.3 Transported of Diluted Species	75
3.3.4 Darcy's Law	77
3.3.5 Heat Transfer in Porous Media	79
3.3.6 Bubbly Flow, $k - \omega$	81
4 Results	85
4.1 Validation of models	85
4.2 2D Single-phase Laminar flow model	87
4.3 3D Single-phase Laminar flow model	101
4.4 2D Multi-phase Turbulent Flow Model	107
4.5 3D Single Phase Turbulent Flow Model	110
4.5.1 Differences with laminar model	112
4.6 3D Laminar Flow Model Open/Closed Cathode Comparison	118
5 Conclusions	124
Bibliography	126

List of Figures

Chapter 1 – Literature Review

<i>Figure 1. 1 Climate change effects [2]</i>	11
<i>Figure 1.2 Hydrogen from renewables [5]</i>	12
<i>Figure 1.3 Blue and green hydrogen comparison [7]</i>	14
<i>Figure 1. 4 Characteristics of main electrolysis technologies [8]</i>	16
<i>Figure 1. 5 Operating principle of alkaline water electrolyzers. [9]</i>	17
<i>Figure 1. 6 Operating principle of solid oxide electrolyte electrolyzers. [9]</i>	18
<i>Figure 1. 7 Operating principle of proton exchange membrane electrolyzers. [9]</i>	19
<i>Figure 1. 8 Water electrolysis [17]</i>	20
<i>Figure 1. 9 Ohmic resistance model for a single channel/land area [19]</i>	24
<i>Figure 1. 10 Polarization curves with all contributes [24]</i>	26
<i>Figure 1. 11 Structure of PEM [25]</i>	27
<i>Figure 1. 12 Development of turbulent flow in a jet [38]</i>	30
<i>Figure 1. 13 Influence of Reynolds number on flow types [40]</i>	31
<i>Figure 1. 14 Different types of Gas-Liquid flows</i>	33
<i>Figure 1.15 Ito et al bubble evolution phenomena [46]</i>	33
<i>Figure 1.16 Min li et al, vortex structure distribution using different model [47]</i>	34

Chapter 2 – Experiments

<i>Figure 2. 1 EnviPark Logo [48]</i>	35
<i>Figure 2. 2 HysyLab logo [48]</i>	35
<i>Figure 2. 3 Test bench</i>	37
<i>Figure 2. 4 LabVIEW screenshot</i>	39
<i>Figure 2. 5 HPR-20 system</i>	40
<i>Figure 2. 6 HPR-20 Vacuum Schematic</i>	41
<i>Figure 2. 7 Hiden HAL 3F Series Triple Filter Mass Spectrometer</i>	42
<i>Figure 2. 8 Inlet of HPR 20</i>	43
<i>Figure 2. 9 Ion Source</i>	43
<i>Figure 2. 10 Detector with Dual Faraday/Secondary Electron Multiplier</i>	44

<i>Figure 2. 11 Polarization curve with closed cathode configuration, $T = 80\text{ }^{\circ}\text{C}$, $p = 0.5\text{ bar}$, mass flow rate = 20 %</i>	<i>47</i>
<i>Figure 2. 12 Polarization curve with closed cathode configuration, $T = 60\text{ }^{\circ}\text{C}$, $p = 0.5\text{ bar}$, mass flow rate = 10 %</i>	<i>47</i>
<i>Figure 2. 13 Polarization curve with open cathode configuration, $T = 60\text{ }^{\circ}\text{C}$, $p = 0.5\text{ bar}$, mass flow rate = 10 %.....</i>	<i>48</i>
<i>Figure 2. 14 Spectrometer data of N2, O2, H2 and H2O.....</i>	<i>49</i>
<i>Figure 2. 15 Spectrometer data of Nitrogen</i>	<i>50</i>
<i>Figure 2. 16 Spectrometer data of Oxygen</i>	<i>50</i>
<i>Figure 2. 17 Spectrometer data of Water</i>	<i>51</i>
<i>Figure 2. 18 Spectrometer data of Hydrogen.....</i>	<i>51</i>
<i>Figure 2. 19 Spectrometer data of Hydrogen of the first two days</i>	<i>52</i>
<i>Figure 2. 20 Spectrometer data of Hydrogen during the last two days</i>	<i>52</i>
<i>Figure 2. 21 Concentration ratio of N2, O2, H2 and H2</i>	<i>53</i>
<i>Figure 2. 22 Hydrogen percentage.....</i>	<i>53</i>
<i>Figure 2. 23 Hydrogen percentage in one hour of steady functioning.....</i>	<i>54</i>
<i>Figure 2. 24 Voltage values in one hour of steady functioning.....</i>	<i>54</i>
<i>Figure 2. 25 Hydrogen percentage in one hour of steady functioning.....</i>	<i>55</i>
<i>Figure 2. 26 Pressure at cathode side, one hour</i>	<i>55</i>
<i>Figure 2. 27 Separation tank charge/discharge in 1 hour. When the valve is at 1, the water is discharged.....</i>	<i>56</i>
<i>Figure 2. 28 Water consumption from 21 of January to 02 of February.....</i>	<i>57</i>

Chapter 3- Modelling

<i>Figure 3. 1 2D Geometry</i>	<i>58</i>
<i>Figure 3. 2 Closeup of the 2D Geometry.....</i>	<i>59</i>
<i>Figure 3. 3 Geometry of the 3D Model.....</i>	<i>59</i>
<i>Figure 3. 4 Geometry of the 3D Model with transparency.....</i>	<i>60</i>
<i>Figure 3. 5 Overview of the 3D geometry.....</i>	<i>60</i>
<i>Figure 3. 6 Anodic channels detail.....</i>	<i>61</i>
<i>Figure 3. 7 Electrolyte membrane with anodic channels.....</i>	<i>61</i>
<i>Figure 3. 8 2D Mesh</i>	<i>62</i>

<i>Figure 3. 9 2D Mesh, close up</i>	63
<i>Figure 3. 10 2D Mesh, close up of the inner part</i>	63
<i>Figure 3. 11 3D Mesh</i>	64
<i>Figure 3. 12 3D Mesh, XY view</i>	64
<i>Figure 3. 13 3D Mesh, YZ view</i>	65
<i>Figure 3. 14 3D mesh, XY view</i>	65

Chapter 4- Results

<i>Figure 4. 1 Polarization curves, open cathode, $T=60^{\circ}$, $p=0.5$ bar</i>	85
<i>Figure 4. 2 Polarization curves, closed cathode, $T=60^{\circ}$, $p=0.5$ bar</i>	86
<i>Figure 4. 3 Polarization curves, closed cathode, $T=80^{\circ}$, $p=0.5$ bar</i>	86
<i>Figure 4. 4 Polarization curve, 2D Laminar Flow</i>	87
<i>Figure 4. 5 Electric Potential at anode and cathode (left) and Electrolyte Potential (right) for different voltage values, from top to bottom respectively: 1,27-1,5-1,8-2,1 V</i>	88
<i>Figure 4.6 Electrolyte field vector, with arrow that indicates the external bias</i>	89
<i>Figure 4.7 Relative Humidity</i>	89
<i>Figure 4.8 Electrode Current Density [A/cm²] at anode and cathode (left) and Electrolyte Current Density at membrane (right) for different voltage values, from top to bottom respectively: 1,27-1,5-1,8-2,1 V</i>	90
<i>Figure 4.9 Oxygen concentration at anode, $V = 2,1$</i>	91
<i>Figure 4. 10 Oxygen concentration at anode, $V = 2,1$, outlet closeup</i>	91
<i>Figure 4.11 Oxygen Concentration at anode/membrane surface</i>	92
<i>Figure 4.12 Hydrogen distribution with different input voltages [up left 1,27-up right 1,5-bottom left 1,8-bottom right 2,1]</i>	93
<i>Figure 4. 13 Hydrogen Concentration at the cathode/membrane interface</i>	93
<i>Figure 4.14 Local current density at Anode/Membrane interface</i>	94
<i>Figure 4.15 Local current density at Anode/Membrane interface</i>	94
<i>Figure 4.16 Distribution of water in the anodic compartment with different voltages. Top left 1,27 V-Top right 1,5 V-Bottom left 2,1 V- Bottom right 2,1 V overview</i>	95
<i>Figure 4. 17 Anodic concentration of water at anode/membrane interface</i>	95
<i>Figure 4. 18 Distribution of water in the cathodic compartment with different voltages. Top left 1,27 V-Top right 1,5 V-Bottom left 1,8 V- Bottom right 2,1 V</i>	96

<i>Figure 4.19 Cathodic concentration of water at cathode/membrane interface.....</i>	<i>96</i>
<i>Figure 4.20 Distribution of water in the electrolyte with different voltages. Top left 1,27 V-Top right 1,5 V-Bottom left 1,8 V- Bottom right 2,1 V.....</i>	<i>97</i>
<i>Figure 4.21 Membrane Electroosmotic Drag Molar Flow.....</i>	<i>98</i>
<i>Figure 4.22 Membrane Diffusion Molar Flow.....</i>	<i>98</i>
<i>Figure 4.23 Temperature Distribution for different voltage values: Top left 1,27 V-Top right 1,5 V-Bottom left 1,8 V- Bottom right 2,1 V.....</i>	<i>99</i>
<i>Figure 4.24 Temperature profile at Anode in function of arch length.....</i>	<i>99</i>
<i>Figure 4.25 Temperature profile at Cathode in function of arch length.....</i>	<i>100</i>
<i>Figure 4.26 Temperature gradients.....</i>	<i>100</i>
<i>Figure 4.27 Polarization curve $T=60^{\circ}\text{C}$ $p=0.5$ bar</i>	<i>101</i>
<i>Figure 4.28 Electric Potential (left) and Electrolyte potential (right) for different value of voltages: from top to bottom, for each row, 1,27 – 1,6 – 2 – 2,4 V</i>	<i>102</i>
<i>Figure 4.29 Relative Humidity</i>	<i>103</i>
<i>Figure 4.30 Oxygen Concentration in anodic channels for different voltage values: Top left 1,27-Top right 1,6-Botto left 2-Bottom right 2,6 V.....</i>	<i>103</i>
<i>Figure 4.31 Oxygen Concentration at anode/membrane interface</i>	<i>104</i>
<i>Figure 4.32 Hydrogen concentration in cathodic channels for different voltage values: Top left 1,27-Top right 1,6-Bottom left 2-Bottom right 2,6 V</i>	<i>105</i>
<i>Figure 4. 33 Hydrogen Concentration at cathode/membrane interface.....</i>	<i>105</i>
<i>Figure 4.34 Water concentration in anodic channels</i>	<i>106</i>
<i>Figure 4. 35 Velocity distribution of liquid (left) and gas (right) phase.</i>	<i>107</i>
<i>Figure 4. 36 Vortex formation.....</i>	<i>107</i>
<i>Figure 4. 37 Volume fraction in function of the height.....</i>	<i>108</i>
<i>Figure 4. 38 Overpotential due to bubble formation</i>	<i>108</i>
<i>Figure 4. 39 Bubble overpotential in function of the applied voltage</i>	<i>109</i>
<i>Figure 4. 40 Turbulent kinetic energy distribution</i>	<i>110</i>
<i>Figure 4. 41 Specific dissipation rate distribution.....</i>	<i>110</i>
<i>Figure 4. 42 Turbulent dynamic viscosity distribution.....</i>	<i>111</i>
<i>Figure 4. 43 Velocity magnitude distribution in turbulent flow model.....</i>	<i>112</i>
<i>Figure 4. 44 Velocity magnitude distribution in laminar flow model.....</i>	<i>112</i>
<i>Figure 4. 45 Vorticity magnitude distribution in turbulent flow model.....</i>	<i>113</i>
<i>Figure 4. 46 Vorticity magnitude distribution in laminar flow model.....</i>	<i>113</i>
<i>Figure 4. 47 Oxygen concentration in turbulent flow model.....</i>	<i>114</i>

<i>Figure 4. 48 Oxygen concentration in turbulent flow model, inlet closeup</i>	<i>114</i>
<i>Figure 4. 49 Oxygen concentration in laminar flow model</i>	<i>114</i>
<i>Figure 4. 50 Oxygen concentration at interface, in function of arch length</i>	<i>115</i>
<i>Figure 4. 51 Water concentration at anode, turbulent flow model.....</i>	<i>115</i>
<i>Figure 4. 52 Water concentration at anode, turbulent flow model, inlet closeup</i>	<i>115</i>
<i>Figure 4. 53 Water concentration at anode, laminar flow model</i>	<i>116</i>
<i>Figure 4. 54 Hydrogen concentration at cathode/membrane interface, turbulent flow model ...</i>	<i>116</i>
<i>Figure 4. 55 Hydrogen concentration at cathode/membrane interface, laminar flow model</i>	<i>117</i>
<i>Figure 4. 56 Turbulent kinetic energy distribution at interface, in function of arch length.....</i>	<i>117</i>
<i>Figure 4. 57 Water concentration at cathode, closed cathode configuration.....</i>	<i>118</i>
<i>Figure 4. 58 Water concentration at cathode, open cathode configuration.....</i>	<i>118</i>
<i>Figure 4. 59 Temperature distribution in closed cathode configuration (left) and open (right). Value of voltages, from top to bottom, for each row: 1,27 - 1,6 - 2 - 2,4 V.....</i>	<i>119</i>
<i>Figure 4. 60 Temperature at interfaces. Left column, closed cathode configuration, right column open one. Top row, temperature at anode/membrane interface, bottom cathode/membrane.....</i>	<i>120</i>
<i>Figure 4. 61 Hydrogen concentration in closed cathode configuration (left) and open (right). Value of voltages, from top to bottom, for each row: 1,27 - 1,6 - 2 - 2,4 V.....</i>	<i>121</i>
<i>Figure 4. 62 Hydrogen concentration at electrode/electrolyte interface, closed cathode configuration.....</i>	<i>122</i>
<i>Figure 4. 63 Hydrogen concentration at electrode/electrolyte interface, open cathode configuration</i>	<i>122</i>
<i>Figure 4. 64 Polarization curve, closed cathode configuration, T = 60 ° C, relative pressure = 0.5 bar</i>	<i>123</i>
<i>Figure 4. 65 Polarization curve, open cathode configuration, T = 60 ° C, relative pressure = 0.5 bar</i>	<i>123</i>

Introduction

Since computer simulation offers a potential technique to obtain knowledge of the process parameters involved, Multiphysics models have been used for a broad range of applications in several industrial and academic sectors.

The hydrogen generation process will be studied using a simulation technique in the framework of this thesis study, and the findings will be compared to experimental data.

As a consequence, the work's main focus will be on several Multiphysics models, which are required to accurately mimic the electrolysis process, as well as an experimental portion to compare the findings.

The necessity to model and test hydrogen manufacturing processes is tied to the current climatic change, which has pushed renewable energy and efficient storage systems into the energy supply chain.

The proper distance from the sun, the presence of an atmosphere, and the existence of the water cycle are the prerequisites for the existence of life on earth. The sun's energy triggered the greenhouse effect about 4 billion years ago: the sun's energetic rays penetrate the atmosphere (an outer layer of about 300 kilometres of mixed gasses), are partly absorbed by the ground or the sea, partly bounce back and are trapped by some gasses (greenhouse gasses, especially carbon dioxide, methane, but also water vapor) which retain the sun's heat. Without the natural greenhouse effect, the average global temperature would be -15 degrees Celsius instead of about +18 degrees Celsius.

Climate change has always been a part of our planet's history. However, the global warming that we have witnessed in the last 150 years is unusual because it is caused by humans. It is known as the man-made greenhouse effect, which occurs in conjunction with the natural greenhouse effect. With the industrial revolution, humans have spewed millions of tons of carbon dioxide and other greenhouse gasses into the atmosphere, more than doubling the amount of CO₂ in the atmosphere over the last 700 thousand years. [1]

This can be observed daily. Over the past 15 years, data collected by thousands of scientists around the world has been analysed and systematized by the Intergovernmental Panel on Climate Change (IPCC). The IPCC concluded that 97 percent of global warming is caused by the anthropogenic greenhouse effect, or human-induced warming. [1]

The average temperature on Earth has increased by 0.98 degrees Celsius since pre-industrial times, and the trend recorded from 2000 to the present indicates that it could reach +1.5 degrees Celsius between 2030 and 2050 without intervention. Global warming is already having an effect: Arctic Sea ice has declined by an average of 12.85% each decade since 1870, while coastal tidal records show an average annual sea level rise of 3.3 millimetres. The most recent decade (2009-2019) was the warmest on record, and 2020 was the second warmest year on record, behind only the record set in 2016. "Fire seasons" have become longer and more severe, like 2019 in Australia, and extreme weather events like hurricanes and flooding have become more frequent.

Weather disasters such as hurricanes and floods have increased every year since 1990. They occur at times of year that were previously unheard of and are becoming increasingly deadly, causing severe droughts in areas already prone to chronic drought, such as East Africa, while the Gulf Stream is

Introduction

slowing down and possibly changing its route. Plant and animal species are migrating from one ecosystem to the next, causing great damage around the world.



Figure 1. 1 Climate change effects [2]

Human activities such as the burning of fossil fuels and deforestation of rainforests are having an increasingly negative impact on the Earth's climate and temperature. They exacerbate the greenhouse effect and global warming by adding massive amounts of greenhouse gasses to those already in the atmosphere. The consumption of coal, oil, and gas, which are responsible for the majority of greenhouse gas emissions, causes the most damage. According to McKinsey's Global Energy Perspective 2019, fossil fuels account for 83 percent of all energy consumption [3].

In December 2015, the Conference of the Parties (COP21) to the United Nations Framework Convention on Climate Change (UNFCCC) signed the long-awaited Paris Agreement on Climate Change, providing a credible framework for achieving decarbonisation with long-term goals to address climate change and a flexible structure based on individual governments' contributions. The signatories agreed to limit the temperature increase to below 2° Celsius above pre-industrial levels, seeking to stay below 1.5°, to limit emissions as soon as possible and to achieve carbon neutrality in the second half of the century.

The energy transition, i.e. the transition from an energy mix based on fossil fuels to one based on renewable sources with low or no carbon emissions, is the most important instrument for achieving this goal.

The energy transition is not a new phenomenon in history. There have been other major epochal shifts in the past, such as the shift from wood to coal in the 19th century or from coal to oil in the 20th century. The need to save the planet from the greatest danger it has ever faced, and to do so as quickly as possible, distinguishes this transition from the last.

This push has accelerated improvements in the energy sector: Renewable technology prices have fallen by 80% for solar PV and 60% for onshore wind in the last ten years (2010-2019)[4].

Introduction

The energy transition, on the other hand, is more than just the gradual closure of coal-fired power plants and the expansion of sustainable energies: it is a system-wide paradigm shift. Electrification, which also makes other sectors such as transport cleaner, and the digitalisation of grids, which increases energy efficiency, both make an important contribution to decarbonisation.

The technologies for decarbonisation are available, they are efficient, and they must be selected at all levels. Science provides reliable facts, estimates of the extensively researched future possibilities.

Renewable energy is both the present and the future of global power generation. The name "renewable" sums up the essence of this type of energy: the ability to occur in nature and regenerate indefinitely without human intervention.

The production of renewable energy means that electricity is obtained from sun, wind, or water, as well as heat from the ground. These components are numerous and widespread in nature, so they can be used to generate electricity. An energy that can cause significantly fewer emissions compared to energy obtained from traditional sources.

All nations of the world share the need to generate more renewable energy and reject traditional sources. According to statistics from the International Renewable Energy Agency (IRENA), renewable energy alone covered three-quarters of new global energy capacity in 2019. Green energy currently accounts for more than a third of global electricity generation[4].

Renewable energy has the potential to become the most beneficial source of energy for the planet and for economic growth. This is because renewable energy is truly and fully sustainable when it is produced within an integrated vision that covers the entire value chain - from production sites to suppliers - and reduces the impact on territory and communities.

Having gone through a cyclical wave of great enthusiasm and deep scepticism over the past decades, hydrogen has undoubtedly established itself as a key element for the energy transition and is at the centre of the political agendas and energy strategies of many countries around the world as well as the European Commission.

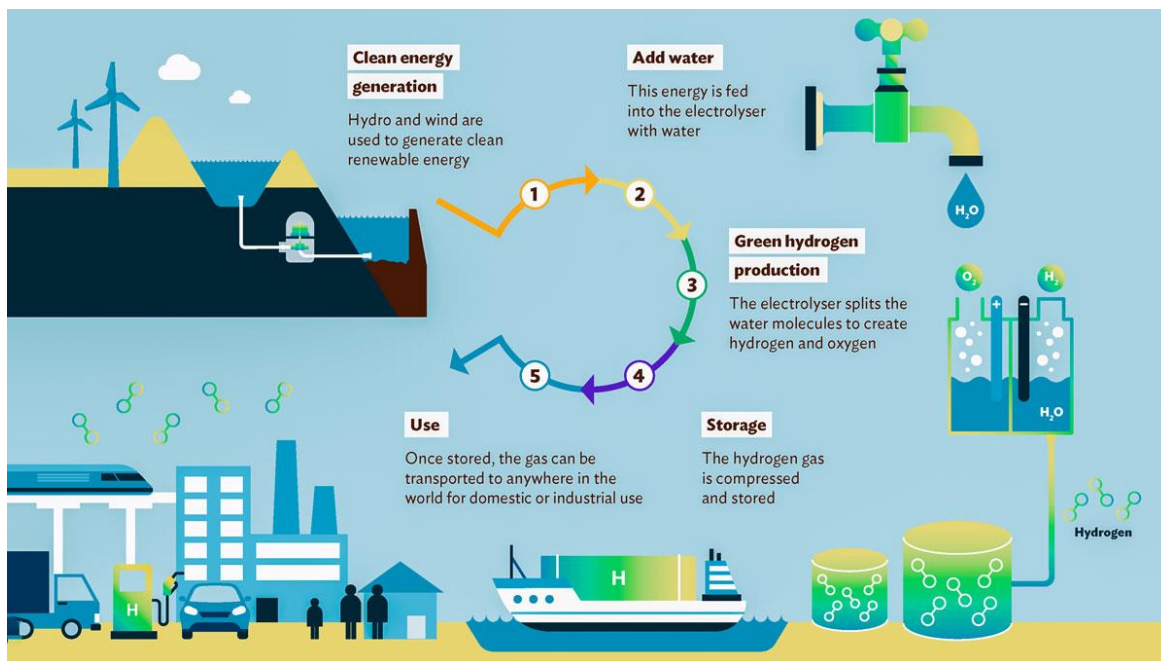


Figure 1.2 Hydrogen from renewables [5]

Introduction

Hydrogen has always attracted attention as an energy vector due to some of its unique properties: it is light, more storable than electricity in the long term, reactive, has a high energy content per unit mass and can be produced cheaply on an industrial scale. Another important aspect is the possibility of using hydrogen to generate "clean" electricity. Indeed, the combustion of hydrogen does not involve the production of carbon dioxide (CO₂) and therefore does not lead to direct emissions. Furthermore, the combustion of hydrogen can be done electrochemically in fuel cells, where the efficiency of the fuel cells is higher than that of combustion and no nitrogen oxides are emitted. Finally, hydrogen can be produced from a variety of renewable energy sources, facilitating the development of robust, resilient energy systems.

Chapter 1

Literature Review

1.1 Hydrogen production

Having introduced hydrogen as a path to decarbonisation of energy supply, now a deeper resume about hydrogen and electrolysis is presented.

Only "green" hydrogen, i.e. hydrogen produced from renewable sources without emitting greenhouse gases, can play the important role in leading towards decarbonisation.

In reality, hydrogen from natural gas reforming ("grey"), coal gasification ("black") and lignite gasification ("brown"), which account for almost 99 percent of the hydrogen produced worldwide, involves massive carbon dioxide emissions [6]. It is therefore clear that traditional manufacturing processes based on the use of raw materials and fossil fuels will have to be phased out over time and give way to creative processes based on the use of renewable resources.

By the time the European Union reaches this goal in 2050, "blue" hydrogen produced using traditional techniques combined with carbon capture and storage devices will help meet the growing demand for hydrogen while minimising the impact on the environment.

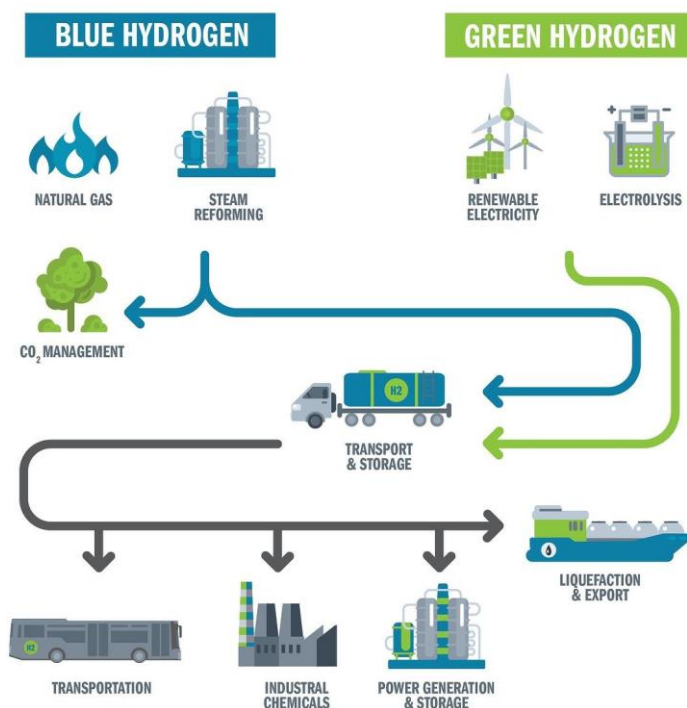


Figure 1.3 Blue and green hydrogen comparison [7]

At the same time, it will promote the development of the infrastructure needed to introduce green hydrogen into energy systems without harming the environment.

Hydrogen is an energy vector, not an energy source, and as such it plays a crucial role in the decarbonisation of various sectors, including the energy industry and the transport sector, due to its properties.

In reality, "green" hydrogen is an inherently clean energy carrier when produced by electrolysis from renewable energy sources and is now seen as one of the key players in the transition to a low carbon economy.

As it is produced using renewable electrical energy, it also supports the integration of electricity and gas from electricity and gas. By using hydrogen produced in this way, it is possible to decarbonise those sectors of the economy that cannot be easily or directly electrified, such as heavy industry, aircraft, road, and sea transport over long distances.

Electrolysis of water fed with energy from renewable sources such as wind and solar is currently the most established and technologically mature technology for producing green hydrogen. The main strategy for integration is to connect the electrolyser to a grid with a high share of renewable energy, with the possibility of using hydrogen production as a grid balancing mechanism.

Green hydrogen may be used as it is, in H₂-CH₄ mixture (hydrogen-methane) mixture or turned into synthetic CH₄ by a process of CO₂ methanation.

In addition to energy usage, green hydrogen may help to the decarbonization of industrial processes by being as a raw ingredient or process fluid.

For example, green hydrogen may be used instead of carbon coke as a reducing agent in steel manufacturing, making it feasible to fulfil the expanding demand for steel with decreased carbon dioxide emissions.

Natural gas is currently the primary source of hydrogen: with approximately 70 million tons of hydrogen produced using about 205 billion cubic meters of natural gas (6 percent of the global consumption of natural gas), it represents about three quarters of the annual world production dedicated to hydrogen. Coal follows second, owing to its major role in China and contributes for around 23 percent of worldwide hydrogen generation utilizing 107 Mt of coal (2 percent of global coal consumption). Oil and electricity contribute for the remaining output. [6]

The electrolysis of water supplied with energy generated by renewable technologies such as wind and solar is now the most consolidated, technologically established, and technologically mature technology for producing green hydrogen. The basic integration plan is connecting the electrolyser to a network with a high proportion of renewables, with the prospect of using hydrogen generation to balance the grid in mind.

It is feasible to enhance the penetration of the same non-programmable renewable sources in the energy system this manner, among other things.

1.2 Water Electrolysis Technologies Comparison

Alkaline water electrolysis, proton exchange membranes and solid oxide water electrolysis are some of the electrolyte's systems created for water electrolysis.

These systems employ a variety of materials and working circumstances, but the operational principles remain the same. Low and high temperature water electrolysis are also conceivable based on varied operating temperatures.

	Low Temperature Electrolysis			High Temperature Electrolysis		
	Alkaline (OH ⁻) electrolysis	Proton Exchange (H ⁺) electrolysis		Oxygen ion(O ²⁻) electrolysis		
	Liquid	Polymer Electrolyte Membrane		Solid Oxide Electrolysis (SOE)		
Operation principles	Conventional	Solid alkaline	H ⁺ - PEM	H ⁺ - SOE	O ²⁻ - SOE	Co-electrolysis
Charge carrier	OH ⁻	OH ⁻	H ⁺	H ⁺	O ²⁻	O ²⁻
Temperature	20-80°C	20-200°C	20-200°C	500-1000°C	500-1000°C	750-900°C
Electrolyte	liquid	solid (polymeric)		solid (ceramic)		
Anodic Reaction (OER)	4OH ⁻ → 2H ₂ O + O ₂ + 4e ⁻	4OH ⁻ → 2H ₂ O + O ₂ + 4e ⁻	2H ₂ O → 4H ⁺ + O ₂ + 4e ⁻	2H ₂ O → 4H ⁺ + 4e ⁻ + O ₂	O ²⁻ → 1/2O ₂ + 2e ⁻	O ²⁻ → 1/2O ₂ + 2e ⁻
Anodes	Ni > Co > Fe (oxides) Perovskites: Ba _{0.5} Sr _{0.5} Co _{0.8} Fe _{0.2} O _{3-δ} , LaCoO ₃	Ni-based	IrO ₂ , RuO ₂ , Ir _x Ru _{1-x} O ₂ Supports: TiO ₂ , ITO, TiC	Perovskites with protonic-electronic conductivity	La _{0.5} Sr _{1.5} MnO ₃ + Y-Stabilized ZrO ₂ (LSM-YSZ)	La _{0.5} Sr _{1.5} MnO ₃ + Y-Stabilized ZrO ₂ (LSM-YSZ)
Cathodic Reaction (HER)	2H ₂ O + 4e ⁻ → 4OH ⁻ + 2H ₂	2H ₂ O + 4e ⁻ → 4OH ⁻ + 2H ₂	4H ⁺ + 4e ⁻ → 2H ₂	4H ⁺ + 4e ⁻ → 2H ₂	H ₂ O + 2e ⁻ → H ₂ + O ²⁻	H ₂ O + 2e ⁻ → H ₂ + O ²⁻ CO ₂ + 2e ⁻ → CO + O ²⁻
Cathodes	Ni alloys	Ni, Ni-Fe, NiFe ₂ O ₄	Pt/C MoS ₂	Ni-cermets	Ni-YSZ Subst. LaCrO ₃	Ni-YSZ perovskites
Efficiency	59-70%		65-82%	up to 100%	up to 100%	-
Applicability	commercial	laboratory scale	near-term commercialization	laboratory scale	demonstration	laboratory scale
Advantages	low capital cost, relatively stable, mature technology	combination of alkaline and H ⁺ -PEM electrolysis	compact design, fast response/start-up, high-purity H ₂	enhanced kinetics, thermodynamics: lower energy demands, low capital cost		+ direct production of syngas
Disadvantages	corrosive electrolyte, gas permeation, slow dynamics	low OH ⁻ conductivity in polymeric membranes	high cost polymeric membranes; acidic: noble metals	mechanically unstable electrodes (cracking), safety issues: improper sealing		
Challenges	Improve durability/reliability; and Oxygen Evolution	Improve electrolyte	Reduce noble-metal utilization	microstructural changes in the electrodes: delamination, blocking of TPBs, passivation		C deposition, microstructural change electrodes

Figure 1. 4 Characteristics of main electrolysis technologies [8]

1.2.1 Alkaline water electrolysis

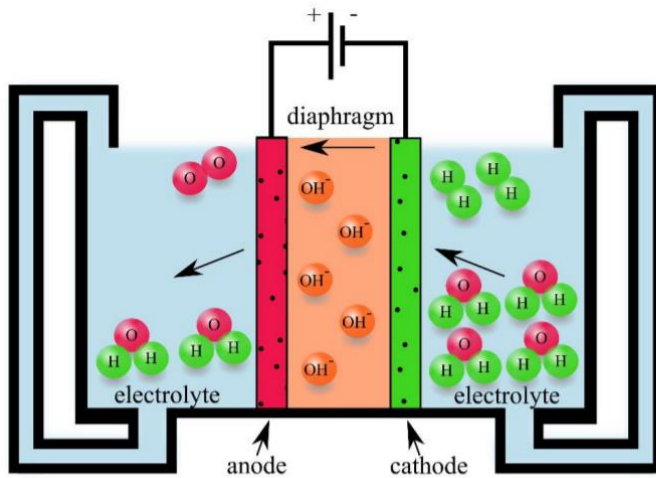


Figure 1. 5 Operating principle of alkaline water electrolyzers. [9]

Alkaline electrolysis has evolved into a well-developed technique for hydrogen generation up to the megawatt range since Troostwijk and Diemann discovered the electrolysis phenomenon in 1789 [10], and it now represents the most extensive electrolytic technology at a commercial level globally. Two electrodes are submerged in a liquid alkaline electrolyte containing a caustic potash solution at a concentration of 25 % KOH. [11]

A diaphragm separates the two electrodes and serves to keep the product gases separate for efficiency and safety. The hydroxide ions and water molecules must be allowed to pass through the diaphragm.

Low partial load range, restricted current density, and low working pressure are three key difficulties with alkaline electrolyzers.

The diaphragm, for starters, does not totally prevent product gases from seeping through it. Because oxygen will be converted back to water with the hydrogen present on the cathode side, diffusion of oxygen into the cathode chamber diminishes the electrolyser's efficiency.

Extensive mixing (especially hydrogen diffusion to the oxygen evolution chamber) occurs as well, which must be prevented to maintain efficiency and safety. This is especially bad at low loads (under 40%), since the oxygen generation rate drops, causing the hydrogen concentration to rise to unwelcome and hazardous levels (lower explosion limit >4 mol % H₂). [12]

Because of the substantial ohmic losses between the liquid electrolyte and diaphragm, alkaline electrolyzers have a low maximum attainable current density. The inability to function at high pressure, which necessitates a bulky stack design configuration, is the third issue, which is also linked to the liquid electrolyte.

1.2.2 Solid oxide electrolysis

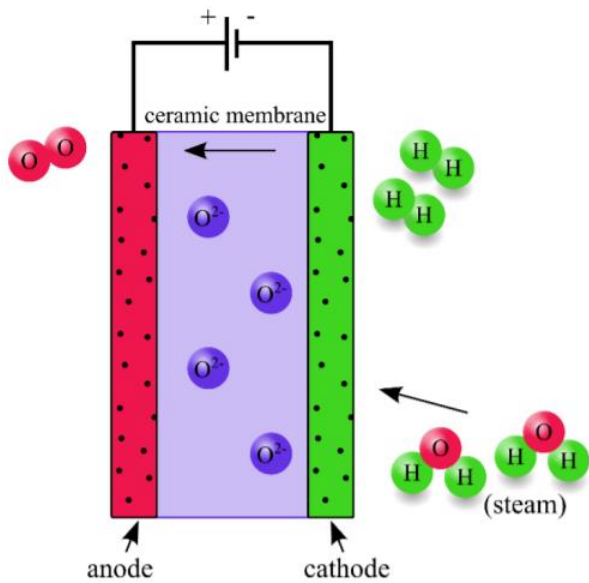


Figure 1. 6 Operating principle of solid oxide electrolyte electrolyzers. [9]

Donitz and Erdle were the first to publish data using a solid oxide electrolyser (SOEC) developed as part of the HotElly project at Dornier System GmbH in 1985[13].

SOECs have piqued attention since then due to their ability to transform electrical energy into chemical energy, resulting in high-efficiency hydrogen production.

SOEC is still in its early stages of development, but research has exploded in the past decade, with firms, research institutes, and universities from all over the globe expressing interest.

SOECs might also be utilized for electrolysis of CO_2 to CO , as well as co-electrolysis of $\text{H}_2\text{O}/\text{CO}_2$ to H_2/CO , owing to their chemical flexibility and high operating temperature (syngas). If concerns relating to the durability of ceramic materials at high temperatures and long-term operation are addressed, the SOEC technology offers a lot of promise for future industrial generation of hydrogen. Understanding the structure and electrochemistry of materials is critical for future advances in order to overcome these shortcomings.

1.2.3 Proton exchange membrane water electrolysis

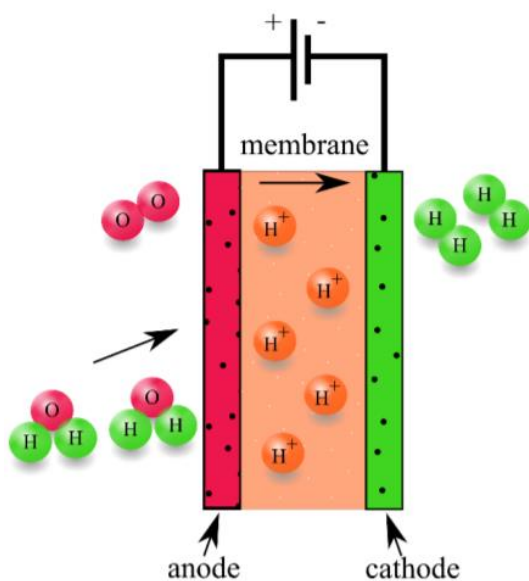


Figure 1. 7 Operating principle of proton exchange membrane electrolysers. [9]

Leonard Niedrach and Thomas Grubb, chemists with the General Electric Company, invented the first proton-exchange membrane technology in the early 1960s [14]. The research and development of these membranes for use in NASA's Project Gemini spaceflight program, Grubb idealized this notion by using a solid sulfonated polystyrene membrane as an electrolyte.

PEM electrolysis, unlike alkaline electrolysis, covers almost the whole nominal power density range (10 to 100 percent).

PEM electrolysis might theoretically achieve values more than 100% of nominal rated power density, where nominal rated power density is determined from a set current density and matching cell voltage. This is owing to the poor hydrogen permeability of Nafion [15].

High operating pressures (equal or differential throughout the electrolyte) may be achieved using a solid electrolyte, allowing for a compact system design with strong/resistant structural features. Some commercial versions claim to be capable of reaching pressures of up to 350 bar [16].

An electrolyser's high-pressure operation provides the benefit of delivering hydrogen at a high pressure (also known as electrochemical compression) to the end user, needing less energy to compress and store the hydrogen. It also reduces the volume of the gaseous phase near the electrodes, resulting in a considerable improvement in product gas removal according to Fick's law of diffusion.

A deep focus on proton exchange membrane electrolysis is introduced in the next chapter.

1.3 PEM Water electrolysis

When a potential difference is forced between two electrodes immersed in an electrolyte containing water, an electric field is generated, pushing negative ions (anions) toward the anode (positive pole) and positive ions (cations) toward the cathode (negative pole).

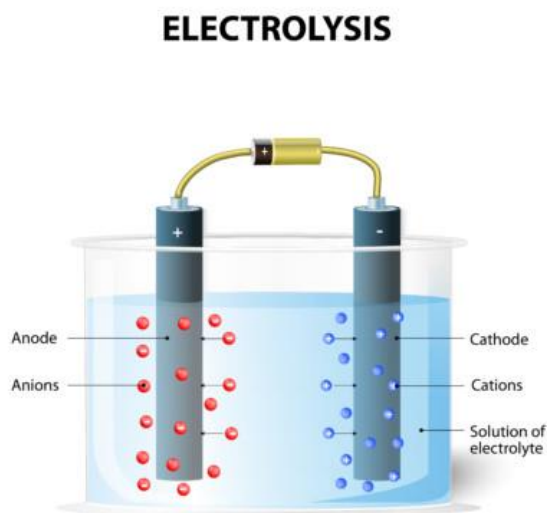


Figure 1. 8 Water electrolysis [17]

At the same time, the ions already existing in the vicinity of the electrodes react in a variety of ways: at the cathode, they take electrons from the metal circuit and reduce themselves; at the anode, they give up electrons to the metal circuit and oxidize themselves. Because each of the two electrodes develops independently, hydrogen and oxygen are produced individually.

Furthermore, a diaphragm placed between the two compartments of the cell inhibits gas mixing, enabling ions in solution to flow through. The only ingredient consumed is water since there are no salts or alkalis that must be added to water to improve its conductivity.

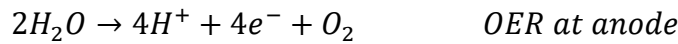
Electrolysis increases the oxidizing power at the anode and the reducing power at the cathode in the chemical system contained in the cell, transforming the electrolysis cell into a battery in which the anode and cathode are respectively positive and negative poles with respect to the external circuit.

The electromotive force generated by the electrolysis in the cell opposes that of the external generator. Because the electrolysis occurs, it is necessary that the electromotive force of the external generator be at least equal to the counter electromotive force generated inside the cell.

In these conditions, the two electromotive forces balance out, and the electrolysis at the limit occurs in a reversible manner. In practice, this occurs with limited electric currents, which need a further increase in the generator's electromotive force to compensate for the overpotentials caused by the activation of electrode reactions and ohmic dissipation.

Oxygen Evolution Reaction, or OER, is the common term for the water splitting semi-reaction. The HER, or Hydrogen Evolution Reaction, occurs when protons generated at anodic reaction sites cross the membrane and decrease to H₂ at the membrane-cathode electrode contact. Anodic and cathodic catalytic semi-reactions are reported below:

Literature Review



(1.1)



(1.2)



(1.3)

Water is pumped to the anode and split into oxygen (O₂), protons (H⁺), and electrons (e) in the water electrolysis process. Protons are transported to the cathode side using a proton conducting membrane.

The electrons leave the anode through the external power circuit, which supplies the reaction with the necessary driving force (cell voltage).

Water is divided into hydrogen and oxygen during the electrolysis process; nevertheless, some energy is needed for this water splitting, whereas the same energy is released with the creation of water molecules into hydrogen and oxygen gases. [18]

It is essential to supply a voltage to the ends of the electrodes that is greater than the reversible voltage V that corresponds to the free energy of creation of the water for the water to decompose. The amount of voltage needed is given by the Nernst equation:

$$V^0 = + \frac{\Delta G}{2F}$$

(1.4)

Where:

- G is the reaction's molar Gibbs free energy change
- F is Faraday's constant (96485 C/mol)
- 2 is the number of electrons exchanged in the process for each water molecule

The Gibbs free energy of the reaction at normal circumstances (25°C and 1atm) is equal to 237.3 kJ/mol, indicating that the minimum voltage at which the reaction occurs is 1.23 V.

The following equation is used to compensate for non-standard temperature and pressure [19]:

$$\Delta G = \Delta G^0 + RT_{avg} \ln \left(\frac{P_{H_2} \cdot P_{O_2}^{1/2}}{P_{H_2O}} \right)$$

(1.5)

The Gibbs Free Energy equation can further be adjusted for the process taking place in the PEM electrolyser by adjusting the temperature and pressure:

$$\Delta G^0 = \left[H_{H_2}(T_{cat}) + \frac{1}{2} H_{O_2}(T_{an}) - H_{H_2O}(T_{an}) \right] - T_{avg} \left[S_{H_2}(T_{cat}, P_0) + \frac{1}{2} S_{O_2}(T_{an}, P_0) - S_{H_2O}(T_{an}, P_0) \right]$$

(1. 6)

where $Hi(T)$ and $Si(T, P_0)$ are the enthalpy and entropy of species, respectively, as measured at the cathode or anode temperature, depending on where the species reduction process occurs[19].

Due to activation overvoltage's at the anode and cathode, ohmic overvoltage in the electrolyte, and mass transport overvoltage, the actual voltage V to be delivered to a cell will be larger than the reversible voltage:

$$V = V^o + V_{act} + V_{trans} + V_{ohm}$$

(1. 7)

V_{act} is the voltage loss due to triggering the electrochemical process and is required to break the molecular bonds.

V_{trans} losses are generated by flow restrictions to the catalyst sites, such as current collector and separator plate morphology, as well as gas bubbles created by the reaction products.

Finally, ohmic losses, or V_{ohm} , are caused by the resistance to electron flow via current collectors and separator plates, as well as protons conduction across membranes. [18]

1.3.1 Activation overpotential

The activation overpotential is a reaction's energy loss that may be characterized as the amount of energy required to start the reaction.

Temperature, catalyst material, usage, and loading all have an impact on this loss. Material processing, temperature, active catalyst regions, use, distribution, age, pressure, morphology, and many other characteristics, some of which are difficult to measure, all play a part in effectively modelling this phenomenon. [20]

The Butler-Volmer equation is an electrochemical model that is widely used in the fuel cell and electrolyser fields to explain the activation overpotential. [19]

$$V_{act,an} = \frac{RT_{an}}{\alpha_{an}F} \operatorname{arcsinh} \left(\frac{i}{i_{0,an}} \right)$$

(1. 8)

$$V_{act,cat} = \frac{RT_{cat}}{\alpha_{cat}F} \operatorname{arcsinh} \left(\frac{i}{i_{0,cat}} \right)$$

(1.9)

The charge transfer coefficients at the anode and cathode are commonly $\alpha_{an} = 2$ and $\alpha_{cat} = 0.5$ in the Butler-Volmer equation. [19], [21].

The value selected for the exchange current densities, $i_{0,an}$ for the anode and $i_{0,cat}$ for the cathode, tends to vary widely across the literature.

Garcia-Valverde et al. [20] used an Arrhenius formula to simulate the temperature dependency of the exchange current density, reported below:

$$i_0 = i_{0,ref} \exp \left[\frac{-E_{exc}}{R} \left(\frac{1}{T_{avg}} - \frac{1}{T_{ref}} \right) \right]$$

(1.10)

1.3.2 Mass transport overpotential

Though there are different theories, mass flow via porous current collectors is usually described as a diffusion process in electrolysis. This is accomplished computationally by using Fick's Law, which for diffusion in the x-axis direction is:

$$J = -D_{eff} \left(\frac{\partial C_i}{\partial x} \right)$$

(1.11)

Where:

- J is the diffusion flow
- D_{eff} is the transport media's effective diffusivity
- C_i is the species i molar concentration.

The Nernst equation may be paired with Fick's law to construct a diffusion rate that restricts the reaction rate at higher current densities, predicting voltage loss owing to a surplus of reaction products at the catalyst sites impeding the reactants.

This method is used for both the cathode and the anode, compensating for the vast differences in hydrogen and oxygen diffusion rates.

$$V_{trans,an} = \frac{RT_{an}}{nF} \ln \frac{C_{O_2,mem}}{C_{O_2,mem,0}}$$

(1.12)

$$V_{trans,cat} = \frac{RT_{cat}}{nF} \ln \frac{C_{O_2,mem}}{C_{O_2,mem,0}}$$

(1.13)

When calculating the voltage drop caused by mass transfer, $C_{i,mem}$ denotes the concentration of species i at the membrane-electrode interface, and $C_{i,mem,0}$ denotes a reference working condition. [18]

1.3.3 Ohmic and ionic transport overpotential

The ohmic overpotential of the current collectors and separator plates is represented using a basic Ohm's Law equivalent resistor model, as seen in Figure 1.9.

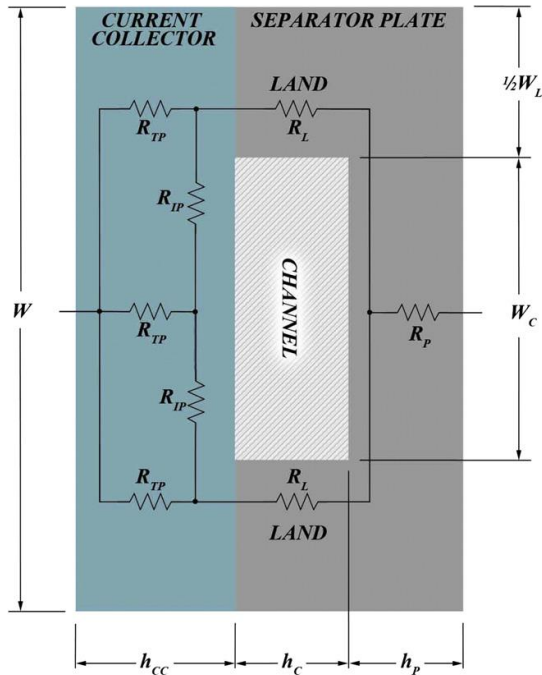


Figure 1.9 Ohmic resistance model for a single channel/land area [19]

The resistors RTP and RIP in Fig. 1.9 represent the current collector's through-plane and in-plane resistances, respectively.

The resistances to land and plate backing are denoted by RL and RP, respectively.

This method is well known and can be predicted quite precisely given the material, temperature, and, in the case of the current collector, sintered particle size and porosity.[22]

At high current densities, the voltage loss owing to the conductivities of the separator plate and current collectors may be significant, therefore as the necessity to operate an electrolyser in an overvoltage situation develops, so does this loss.

The use of Ohm's Law is the modelling method used by practically all models for this sort of loss:

$$V_{ohm} = R_{tot}I + \delta_{mem} \frac{I}{A\delta_{mem}}$$

(1.14)

Where:

- R_{tot} is the cell's total resistance (catalyst and anode sides)
- I is the cell current
- δ_{mem} is the membrane thickness
- A is the membrane's surface area.

Ohm's law is used to a circuit similar to that depicted in Fig. 1.9 to determine R_{tot} . Many ways to simulating proton conductivity across the membrane exist, the majority of which were developed for fuel cell modelling.

For what regards δ_{mem} Choi et colleagues. created a considerably more detailed model for membrane conductivity based on Grotthuss diffusion and conventional mass diffusion of the hydronium ions.

This model is superior to the traditional empirical relationship since it eliminates the need for fitting parameters for proton transport and instead relies purely on membrane physical properties.

The proton transfer is characterized as follows [23]:

$$\delta_{mem} = \frac{\varepsilon_i}{\tau} \left[\frac{F^2}{RT_{avg}} \left(D_H^\Sigma + C_H^\Sigma + D_H^G + C_H + \frac{D_{H^+}^W}{1 + \delta_c} C_{H^+} \right) \right]$$

(1.15)

Where:

- ε_i is the porosity factor
- τ is the tortuosity factor
- D_H^Σ is the surface diffusion coefficient
- C_H^Σ is the concentration of surface protons
- D_H^G is the Grotthuss diffusion coefficient
- C_H is the bulk proton concentration
- $D_{H^+}^W$ is the mass diffusion coefficient
- δ_c is the Stefane-Maxwell diffusion ratio.

1.3.4 Polarization Curve

The Polarization Curve is shown in a more general version in equation 1.17 and figure 1.10, which considers the three separate contributions on both the anodic and cathodic sides.

$$V = V^0 + V_{act,an}(i) + V_{act,cat}(i) + V_{ohm}(i) + V_{trans,an}(i) + V_{trans,cat}(i)$$

(1.16)

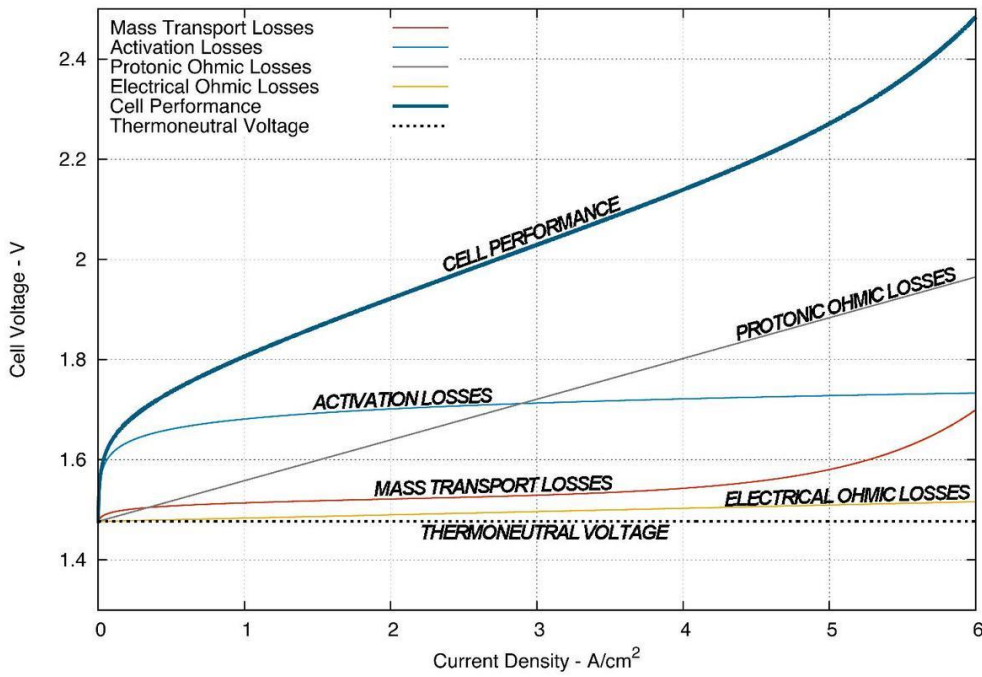


Figure 1.10 Polarization curves with all contributes [24]

1.4 State of the art

Membrane electrode assemblies (MEAs), current collectors (gas diffusion layers), and separator plates are the main components of a PEM water electrolysis cell.

The electrolytic cell's heart is MEA, which divides the cell into two halves (anode and cathode).

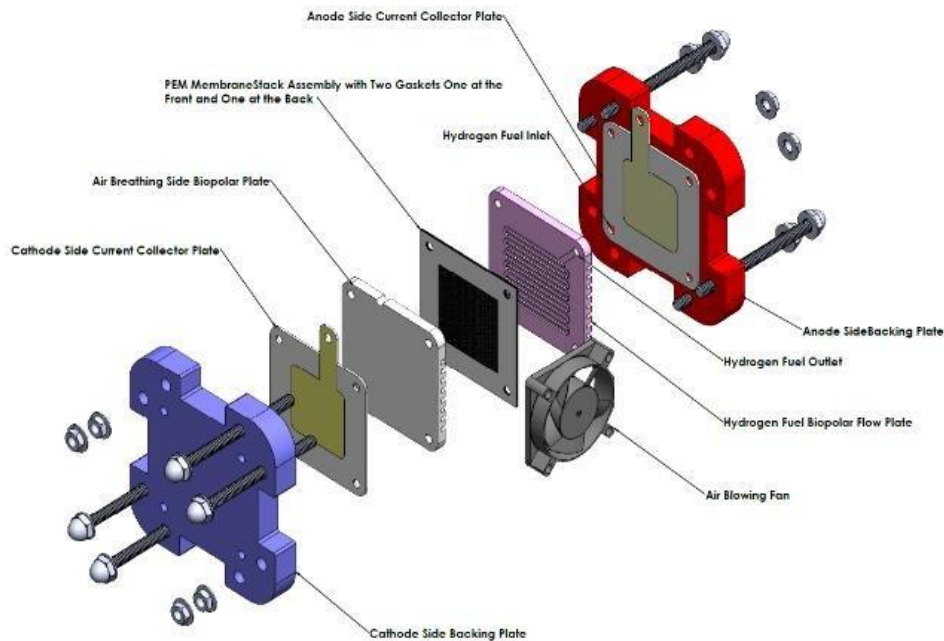


Figure 1. 11 Structure of PEM [25]

1.4.1 Membrane electrode assemblies

Membrane electrode assemblies are made up of membrane, ionomer solution, anode and cathode electrocatalysts, and they account for around a quarter of the entire cell cost.

Membranes comprise the PEMWE cell's backbone; the most popular membranes are perfluorosulfonic acid polymer membranes like Nafion, Fumapem, Flemion, and Aciplex [26].

One of the remarkable qualities of these membranes is that they have excellent mechanical strength, high efficiency, and long-lasting durability, as well as strong proton conductivity.

However, Nafion membranes (Nafion 115, 117, and 212) are now the most often utilized in PEM water electrolyzers because of their robust advantages, such as functioning at greater current densities ($2 A/cm^2$), high durability, strong proton conductivity, and superior mechanical stability. [27]

1.4.2 Current collectors

Water is pumped to the anode side of the PEM cell, where oxygen evolution reaction occurs, and the feed water goes via separator plates and diffuses through current collectors in the PEM water electrolysis process. The water molecule is broken into oxygen, protons, and electrons when the feed water reaches the electrode surface. Through the electrode surface, current collectors, and separator plates, oxygen is returned to the cell.

The proton conducting membrane transports protons from the anode electrode surface to the cathode side. The electrons go from the current collectors to the separator plates, then to the cathode side, where they are recombined with protons and released as hydrogen.

Cathode current collector and separator plates are used to remove the hydrogen from the cell. As a result, current collectors play a crucial part in the entire process of PEM water electrolysis as well as cell efficiency [28]. Due to the acidic environment, current collectors must have corrosion resistance, strong electrical conductivity, a high over potential, and the presence of oxygen. The membrane is also given significant mechanical strength by the current collectors.

Furthermore, because the produced gases must be effectively expelled and water must reach the catalytic sites of the electrode surface, current collectors with optimized porosity and pore volumes are required.

Titanium plates are often used as prospective current collectors in PEM water electrolysis systems because these materials have unique qualities such as strong electrical conductivity, mechanical stability, and corrosion resistance in acidic media [29].

1.4.3 Separator plates

PEM water electrolysis separator plates are composed of titanium, stainless steel, and graphite; however, these materials are expensive and have a variety of operating limitations.

The research and development of separator plates is facing substantial hurdles due to the disadvantages as well as the need of cost reduction. Furthermore, the surface structure of the separator plates is particularly important for the PEM water electrolysis cell since they need to provide a conduit for pumping water and generated gases out of the electrolysis cell [30].

For improved performance, several electrolyser's systems use various designs of separator plates, but the straight parallel flow field design has demonstrated good electrochemical activity, particularly in PEM water electrolysis [31].

Titanium materials typically have excellent strength, thermal conductivity, permeability, and resistivity; however, anode side (oxygen) titanium corrodes and forms an inert oxide layer. As a result, the electrolyser's performance suffers.

Precious metal coatings and alloys have been investigated to overcome these concerns and preserve titanium plates. This coating significantly reduced corrosion rates, but it required more processing, costly coating ingredients, and a pricey base titanium. As a result, finding cost-effective separator plates remains a difficulty.

1.4.4 Hydrogen evolution process electrocatalysts

Platinum (Pt) based materials is a standard catalyst for the hydrogen evolution reaction because Pt has excellent HER activity and is stable in acidic environments, as a consequence, highly dispersed carbon supported Pt-based materials are now benchmark catalysts for HER in PEM water electrolysis [32].

However, since platinum-based catalysts are more costly, the majority of research has concentrated on improving the particular performance and durability of electrocatalysts in order to reduce the cost of electrocatalysts and operating expenses.

Although it is important to reduce the Pt loading on carbon or discover an alternative to Pt-based electrocatalysts for economic viability the electrochemical active surface area is typically generated using scattered carbon nanoparticles to increase surface area and hence reduce Pt loadings. The electrocatalyst is then housed in gas diffusion electrodes made of carbon nanotubes/carbon black, which have a vast surface area and are inexpensive electronic carriers [16].

Cathode side metal loading is currently controlled at about $0.5\text{--}1\text{ mg/cm}^2$, and additional reductions will be required to get possible values below 0.2 mg/cm^2 [33].

Palladium, which is plentiful on Earth and less expensive than platinum, has exhibited outstanding electrocatalytic activity for numerous oxidation and reduction prompting increased interest in Pd-based electrocatalysts for the hydrogen evolution reaction [34].

1.4.5 Oxygen evolution process electrocatalysts

As an electrocatalyst for the oxygen evolution process (OER) in a PEM water electrolyser, metal oxides at the cutting edge of technology are being used.

Metal oxides IrO_2 and RuO_2 have the highest metallic conductivity of $10^4 / \text{cm } \Omega$ among these metal oxides.

The electrons of d-orbitals in these d-bands are responsible for the electron conductivity in these oxides. As a result, the OER performance of RuO_2 is superior to that of other metal oxides [35].

The corrosion of the perfluorosulfonic membrane and the high anodic potential during OER make RuO_2 more active than IrO_2 but less stable, while IrO_2 is the most resistant material to OER in acidic environments but has a lower performance. Researchers have been working on OER alternative catalysts for the last several years in an effort to solve these limitations while also increasing efficiency and lowering the cost [36].

1.5 Turbulent Dispersed Multiphase Flow in PEM water electrolysers

In this section of the chapter the major aspects that regards the multiphase turbulent gas flow in a PEMEC will be analysed, in order to explain the CFD simulations performed later in this thesis.

Before going deeply in the analysis of the flow inside a PEMEC, a brief review about Laminar/Turbulent flow, Multiphase flow and bubbly flow is presented.

1.5.1 Turbulent Flow

A turbulent regime in fluid dynamics refers to irregular flows including eddies, swirls, and flow instabilities. High momentum convection and low momentum diffusion dominate it.

The laminar regime, on the other hand, arises when a fluid flows in parallel layers with no interruption between them. Turbulence occurs often in both natural and human events; examples include the rising of cigarette smoke, waterfalls, blood flow in arteries, and the majority of terrestrial atmospheric recirculation.

The turbulence regime occurs in human uses such as vehicle aerodynamics, but also in numerous industrial applications such as heat exchangers, quenching operations, and continuous steel casting [37].

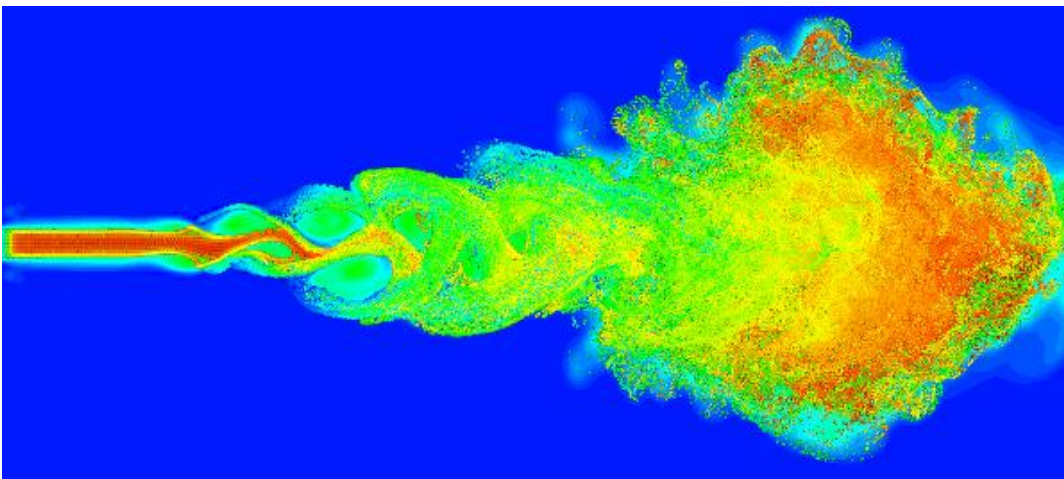


Figure 1. 12 Development of turbulent flow in a jet [38]

The Reynolds number is a useful metric for forecasting whether a flow will be laminar or turbulent. It represents the ratio of inertial forces to viscous forces. It may be deduced that when viscous forces are dominant (low Re , slow flow), they are sufficient to maintain all fluid particles in line, resulting in a laminar flow. Even extremely low Re suggests sluggish creeping motion with no inertia effects. The flow is turbulent when inertial forces prevail over viscous forces (when the fluid is moving faster and Re is bigger).

It is a dimensionless number made up of the flow's physical features. A higher Reynolds number implies more turbulence in the flow.

It is defined as follows:

$$Re = \frac{\rho u d}{\mu} = \frac{u d}{\nu}$$

(1.17)

Where:

- ρ is the density of the fluid
- u is the macroscopic velocity of the flow
- d is the characteristic length (or hydraulic diameter)
- μ is the dynamic viscosity of the fluid
- ν is the kinematic viscosity of the fluid.

Turbulent flows occur when Re surpasses a particular threshold, known as the "Critical Reynolds number," which varies depending on the application's topology and flow mechanics [39].

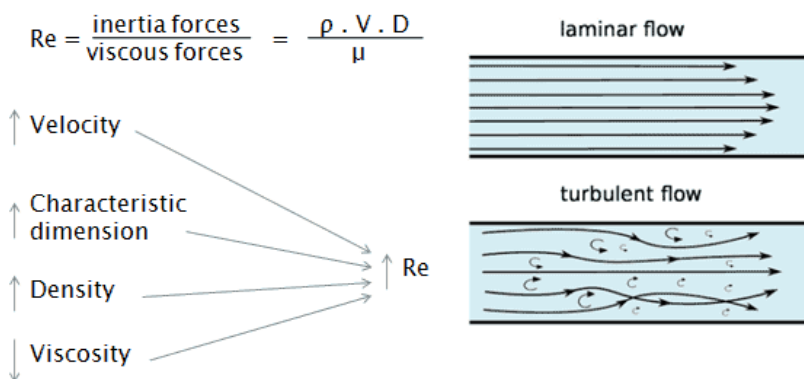


Figure 1.13 Influence of Reynolds number on flow types [40]

1.5.2 Multiphase flows

Multiphase flows include a wide range of topics, including a variety of technological settings, a wide range of sizes, a large range of engineering disciplines, and a variety of analytical techniques.

Any fluid flow that contains more than one phase or component is referred to as multiphase flow. As a result, the flows exhibit some amount of phase or component separation on a scale that is much larger than the molecular size. This still leaves a huge range of multiphase flows to choose from.

Disperse flows and segregated flows are two typical topologies of multiphase flow that may be advantageously determined from the beginning.

- Dispersion flows are flows that include finite particles, droplets, or bubbles (the disperse phase) that are spread throughout a linked volume of the continuous phase.

- Separated flows, on the other hand, are made up of two or more continuous streams of distinct fluids that are separated by interfaces [41].

Two kinds of models are often used in dispersed flows: trajectory models and two-fluid models. The velocity of the dispersion phase is examined in trajectory models by tracing the motion of either the real particles or the motion of bigger, representative particles. The intricacies of the flow surrounding each particle are obfuscated by presumed drag, lift, and moment forces acting on and modifying their trajectory.

The dispersion phase is handled as a second continuous phase mixed and interacting with the continuous phase in the alternative method, two-fluid models.

Separated flows, on the other hand, have much less difficulties. In principle, the single-phase fluid flow equations in the two streams must be solved, and the two streams must be coupled via proper kinematic and dynamic conditions at the interface [41].

Considering a PEM electrolyser, the interaction we are interested in are related to gas-liquid multiphase.

Gas-liquid flows are the most difficult of the four types of two-phase flows (Gas-Liquid, Gas-Solid, Liquid-Liquid, and Liquid-Solid) since they combine the features of a deformable interface with the compressibility of one of the phases.

The gas-liquid interfacial distribution may adopt any of an unlimited number of shapes for given fluxes of the two phases in a particular channel.

However, various varieties of interfacial distribution [42] [43] [44], also known as flow regimes or flow patterns, may be categorized:

- Bubble Flow, in which the liquid is continuous and has a dispersion of bubbles within it.
- Slug or Plug Flow, in which the bubbles have coalesced to form larger bubbles that approach the tube's diameter.
- Churn Flow, in which the slug flow bubbles have broken down to give an oscillating churn regime.
- Annular Flow, in which the liquid flows on the tube's wall as a film (with some liquid entrained in the core).
- Wispy Annular Flow, in which the concentration of droplets in the gas core rises as the liquid flow rate rises, resulting in the development of huge lumps or streaks (wisps) of liquid.

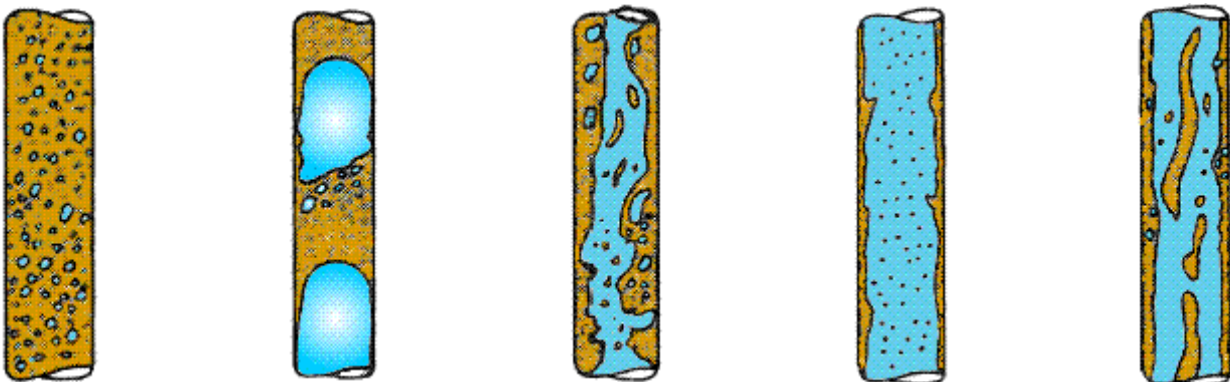


Figure 1. 14 Different types of Gas-Liquid flows

1.5.3 Two-phase turbulent flow in PEM electrolyser cells

For Mo et al [45] there are typically four kinds of two-phase flow regimes in PEMEC microchannels: bubbly, plug, slug, and annulus. According to the visualization findings, the most prevalent phenomena are bubbly, annular, and slug.

Li et al find out that [46] the performance and efficiency of proton exchange membrane electrolyser cells are influenced by gas bubble dynamics and two-phase flow.

In particular, Li et al demonstrate that temperature and current density have a significant impact on bubble growth rate and response locations, whereas flow rate has a little impact.

Temperature and/or current density increase the quantity, growth rate, nucleation site, and slug flow regime of oxygen gas bubbles, indicating that increasing temperature and/or current density may improve oxygen generation efficiency.

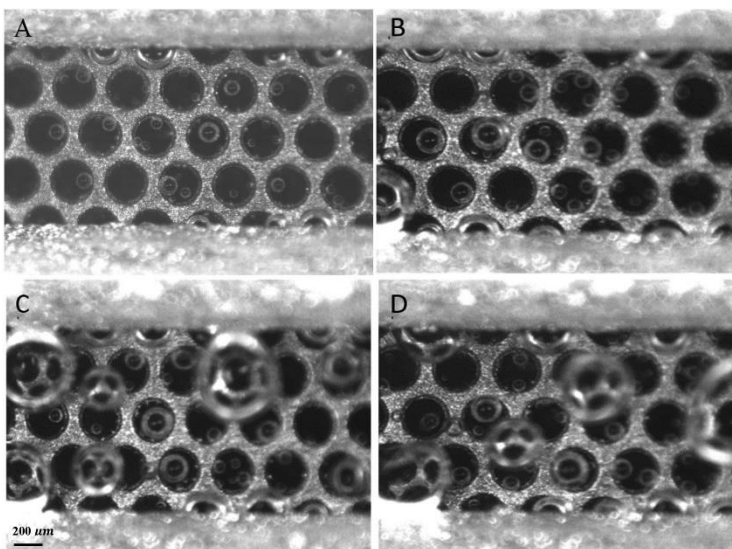


Figure 1.15 Ito et al bubble evolution phenomena [46]

Another interesting study by Min Li et al [47] compared different simulation approaches to analyse flow characteristics in a model stack and investigate the influence of operational circumstances on flow sharing.

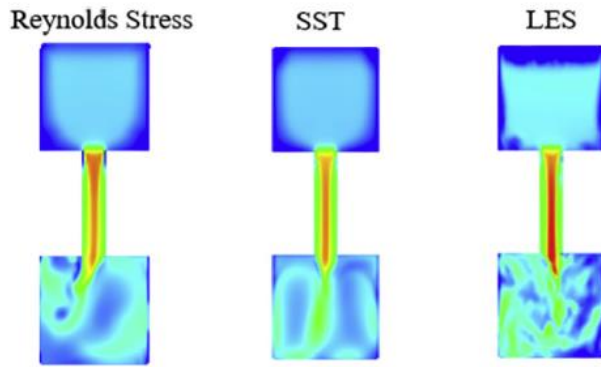


Figure 1.16 Min li et al, vortex structure distribution using different model [47]

Min Li compared three types of models of two-phase multiphase flow, the RANS model, the Shear stress transport (SST) model and the DNS/LES time-variant models, obtaining the most accurate results with the Large Eddy Simulation one.

In the modelling chapter of this thesis a more accurate review of this turbulent models will be discussed as well as the performing of the CFD simulations, in order to validate the models of the articles mentioned above.

Chapter 2

Experiments

In this chapter of the thesis all the experiments made on the PEM test bench during my stage will be reported, as well as an accurate description of the test bench and the mass spectrometer, the instrument I used during the stage to measure the hydrogen production.



Figure 2. 1 EnviPark Logo [48]

The stage was performed at HysyLab, in the Environment Park, that is Turin's environmental scientific and technology park.

In conjunction with Politecnico di Torino and IIT, Italian Institute of Technology, HysyLab is a laboratory specialized to hydrogen technology.

HysyLab has been supporting the system of enterprises and research on problems of hydrogen generation, storage, and usage as an energy carrier, as well as the numerous uses of fuel cell systems in various industries, including mobility, since 2002.



Figure 2. 2 HysyLab logo [48]

The laboratory disposes of 11 testing stations containing the following gases: H₂, CH₄, CO₂, CO, O₂, N₂, and compressed air at a pressure of 30 bar.

Currently, the stations perform the following tasks: using H₂ as a carrier to test PEM/SOFC single cells, fuel cell stacks, electrolysers, and fuel cell power systems; using H₂ as a chemical reagent in the conversion and enhancement of CO₂; and using H₂ as a chemical reagent in the conversion and enhancement of CO₂ (CO₂ CIRCLE LAB).

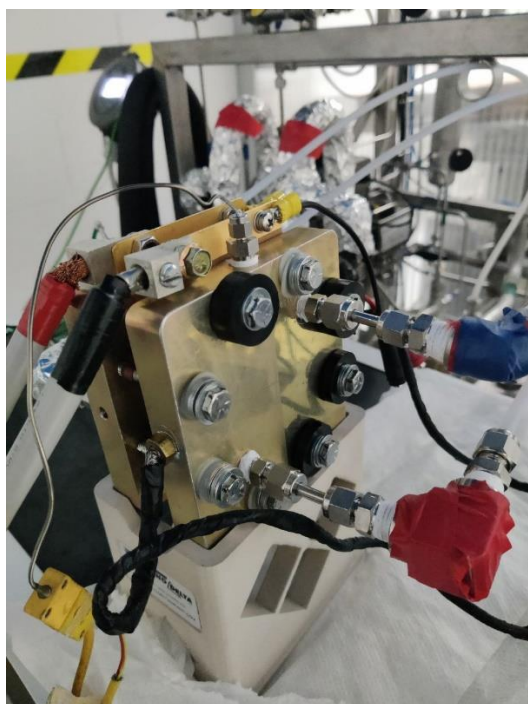
2.1 Test Bench and Electrochemical Cell

Regarding the electrochemical cell used, the following were the specifics.

Area of Membrane Electrode Assembly	25 cm ²
Material of membrane	Nafion 117
Anode Catalyst Layer	2 mg Ir/cm ² catalyst loading,
Cathode catalyst layer	Advanced carbon with 1 mg Pt/cm ² catalyst loading
Gas Diffusion Layers, anode side	Titanium mesh, 180 μm with a thickness
Gas Diffusion Layers, cathode side	Freudenberg H23C6 carbon paper GDL with MPL of 250 μm and E15 GDL of 124 μm
Back plate, anode side	Titanium block 8.47 mm thick, triple serpentine shaped
Back plate, cathode side	Graphite Poco block, 12.45 mm thick, triple serpentine shaped
Current collectors	Gold-plated copper, isolated from end plates thanks to a Teflon's layer
End Plates	Aluminium, sealed with six bolts

Table 1 Electrochemical cell specifics

Below, the electrochemical cell used in the experiments



Experiments

The test bench used is made by Tecnodelta S.r.l., a company that specializes in designing systems and equipment for special fluids and can test single electrolytic cells as well as tiny assemblies of several cells (stack).



Figure 2. 3 Test bench

Experiments

Two external lines, one for nitrogen and the other for compressed air, provide power to the rig. The first is required for cleaning and pressurization, while the second is required for proper pneumatic valve functioning. The nitrogen line is used to pressurize the system, as well as to hold water. Ion exchange resins situated downstream of the pumping system further demineralize water, lowering its conductivity to less than 1 S/cm.

A storage tank of 10 litres is included in the system since the electrolysis process requires a large volume of demineralized water.

For the anode and cathode, there are two major loops in the tank, one on each side. The anode side feeds the electrochemical cell, while the cathode side feeds the cooling system.

Anodic and cathodic outputs are characterized by biphasic mixtures; therefore, they must be filtered out separately:

1. The first step is cooling, and condensers are positioned directly at the end of the different channels to aid in this process. A tube-in-tube condenser has a hot mixture flowing in the inner tube while cooling water flows in the annular area, which may be regarded to be around 15 degrees Celsius.
2. The gas/liquid separators, two 1-liter containers with two outlets each, one in the top section for the gas-rich combination and one in the bottom part for the liquid-rich mixture, are used for the separation process' second step.

For maximum regulation of demineralized water levels, the two separators are arranged at the same height. Fill and drain valves in the separators are regulated by level meters to maintain the cell's appropriate operating level.

Unnecessary pressure unbalancing between the electrolyser's two sides results in excessive water consumption and unrealistic working conditions.

At both cathode and anode side, is present also:

- Pressure transducers, that transforms pressure into an analog electrical signal. The type used is the strain-gage base transducer, in which the physical deformation of strain gages glued into the diaphragm of the pressure transducer and coupled into a Wheatstone bridge arrangement is used to convert pressure into an electrical signal. When pressure is applied to the pressure transducer, the diaphragm deflects, putting strain on the gages. The strain will cause a proportionate change in electrical resistance to the pressure. The data are sent in real time to the LabView software.
- Back pressure controller, a device that maintains a constant pressure upstream of its own input. The regulator opens to alleviate excess pressure when the fluid pressure in the process at the back pressure controller's intake reaches the setpoint. Is used to control the pressure on both sides.

After the separators, two more 250-ml containers are added for maximum separation efficiency. With a maximum flow rate of 10 litres per minute, the volumetric pump is used to bring water into the circuit. Redundancy and stack operations are both supported by an additional high-flow volumetric pump in the system.

For optimal performance, warm water is pushed via an external electrical heater. A plate heat exchanger transfers the heat to the fluid, and a PID temperature controller ensures that the fluid's temperature remains almost constant.

Experiments

Electrochemical impedance spectroscopy (EIS) analysis is part of the rig and allows the test bench to describe electrochemical devices by examining voltage-current curves and detecting impedance. Only the polarization curve is assessed in this thesis; the EIS process is not used.

The test bench enables for experiments with both anionic (alkaline cells) and cationic (PEM) electrolytic cells using low temperature electrolysis devices (up to 150 ° C).

All the data are collected through LabVIEW.

LabVIEW is a system design tool for creating test, measurement, and control applications that need quick access to hardware and data.

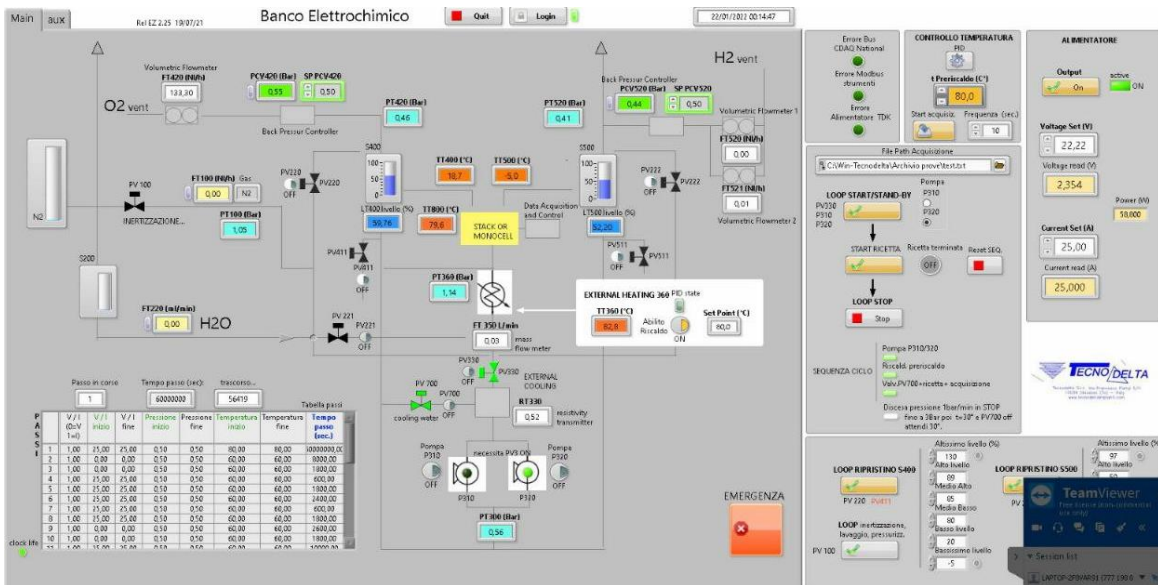


Figure 2. 4 LabVIEW screenshot

2.2 Mass spectrometer

As mentioned above, my internship objective at Environment Park was focused on collecting and analysing the data from the mass spectrometer, in particular regarding the production of Hydrogen.

The mass spectrometer used was Hiden HPR-20 QIC R&D by Hiden Analytical, a quadrupole mass spectrometer for advanced research. The Hiden RGA Mass Spectrometer consists of an Ion Source, a Quadrupole Filter and Detector.

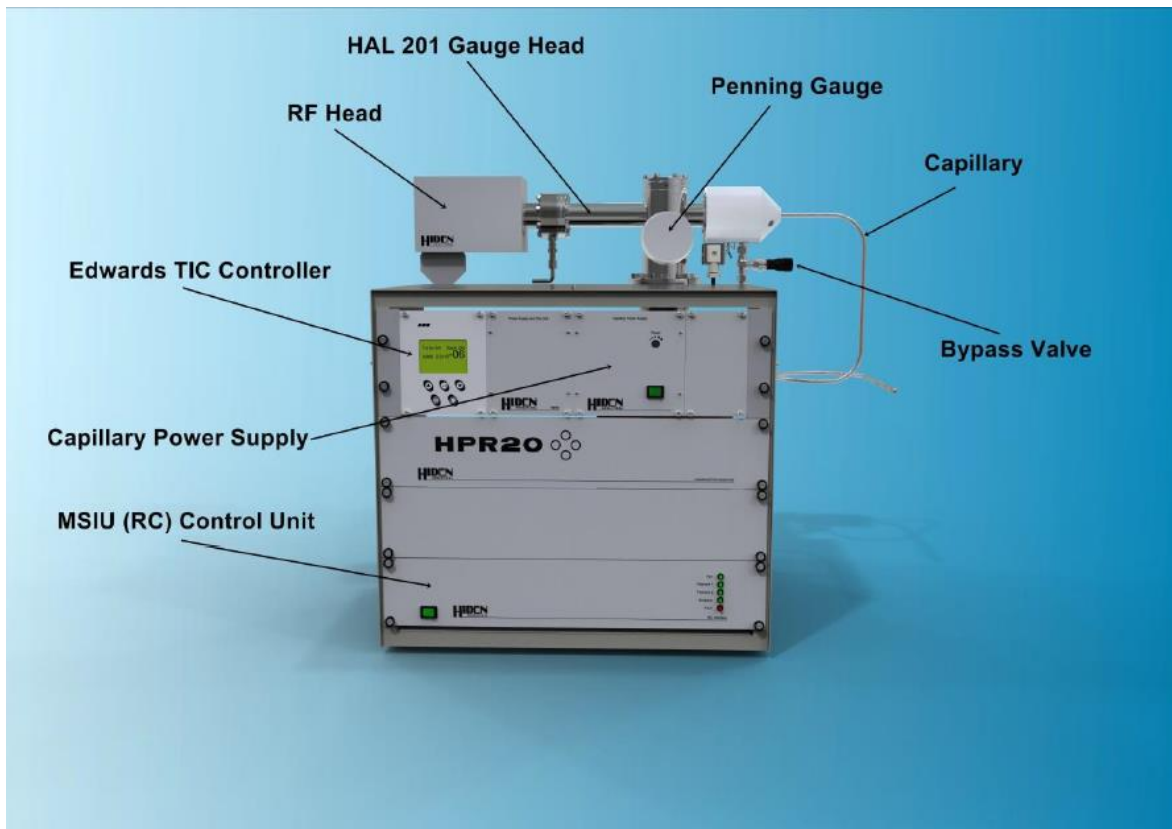


Figure 2. 5 HPR-20 system

The following components are part of the Hiden HPR-20 system:

- **MSIU** The MSIU, also known as the RC Controller Unit, is the key link between the PC and the gauge head. RS232, LAN (Local Area Network), or USB are used to connect to the PC. It also uses the RF Head to regulate the voltages that are delivered to the Gauge Head.
- The **RF Head** provides RF (Radio Frequency) and DC to the Gauge Head for the Mass Filter, which 'filters out' the Ions of Interest. All other ions are eliminated because each ion has a unique DC and RF voltage that allows it to pass through the Mass Filter.
- The Mass Filter, Ion Source, Filaments, and Detector are all found in the Gauge Head, which is located within the Vacuum Housing (s).
- The **Capillary** is a heated inlet with an inert silica coated glass liner. With a minimum pressure of 1atm, the Capillary is linked to the 'T' at the sample end.

Experiments

- Bypass-Valve, that allows for adjustment of the flow rate into the Mass Spectrometer. Only around 1% of the sample is accepted into the system after it is pumped out by the Bypass Pump.
- CPS: The Capillary Power Supply provides the energy to heat the capillary.
- Penning Gauge: the total pressure gauge, which is reliant on gas, is the Penning Gauge. Total Pressure is shown on the Edwards TIC and can be transferred into MASsoft (software related to the mass spectrometer, focus on the next paragraph) in certain situations.
- Edwards TIC (Technical Information Centre): the vacuum pumps and the Penning Gauge are controlled by the Edwards TIC (Turbo Instrument Controller). It also includes the ability to manage the MSIU controller's External Trip for further Vacuum Gauge Head protection.

The HPR 20-QIC Vacuum System is shown below and it consist in the UHV housing houses, the Mass Spectrometer Probe and the total pressure gauge.

The UHV turbo molecular pumping set includes:

- Turbo pump, which is coupled to the UHV housing.
- A two-stage rotary pump or a diaphragm (membrane) pump used as a turbo backup pump.
- Operate electronic devices.
- Vacuum regulator and venting device

The turbo pump has a typical pumping speed of 60 L/s.

The vacuum controller connects with the turbo pump controller, backup pump, and venting operations, as well as allowing the pumping set to be started with a single switch. It also offers interlocking to protect the ionisation source filaments in the Mass Spectrometer.

When the turbo pump is not functioning, automatic venting protects the Mass Spectrometer and UHV housing from pump oil pollution.

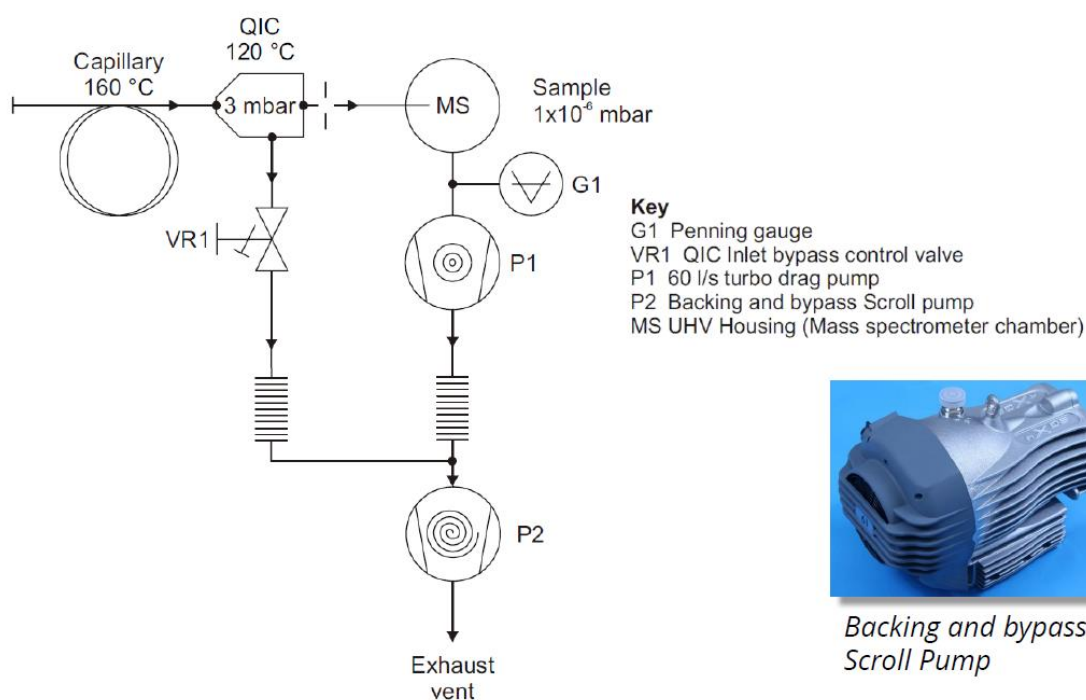


Figure 2. 6 HPR-20 Vacuum Schematic

Experiments

For what regards the filter, the Hiden HPR 20 has a triple filter, for two major benefits:

- Enhanced sensitivity for high mass transmission and greater abundance sensitivity are provided by strict management of the quadrupole entrance and exit fields.
- Improve of long-term stability. The majority of the quadrupole ioniser's deselected ions deposit harmlessly on the RF-only pre-filter stage, reducing contamination on the mass selective main filter.

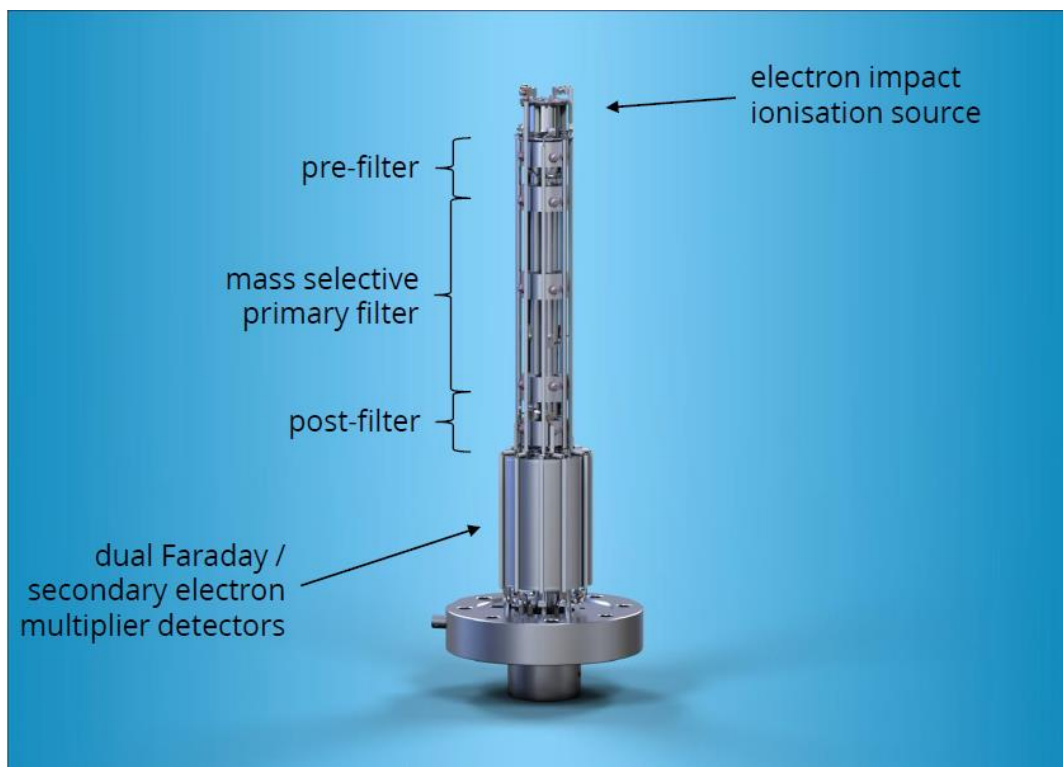


Figure 2. 7 Hiden HAL 3F Series Triple Filter Mass Spectrometer

At the inlet of the Hiden HPR 20, as we can see in figure 19, the following parts are found:

- Heated Capillary, to avoid condensation effects. It matches the flow of the species under analysis for an optimum response and minimum time of recovery.
- Platinum and Quartz wetted surfaces, to avoid memory effects.
- Interchangeable sampling capillaries, that consent analysis from 10 Torr to 2 bar.
- Minimum internal volume that can detect PPB (part per billion).

Experiments

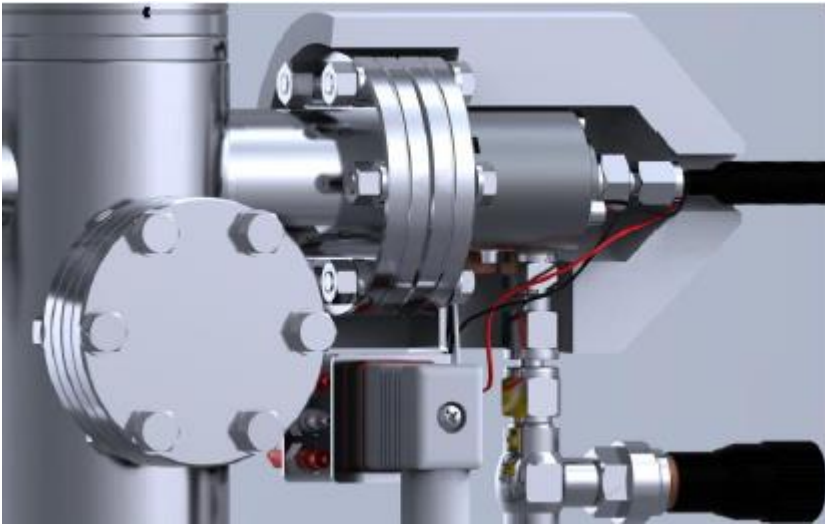


Figure 2. 8 Inlet of HPR 20

Having listed all the components of the Hiden HPR20 mass spectrometer, the working principles of the machine are now explained.

An Ion Source, a Quadrupole Filter, and a Detector, as said above, make up the Hiden RGA Mass Spectrometer. The Filaments in the Ion Source are employed to produce an Electron Beam, which turns gas molecules into charged particles, or +ve Ions, by Electron Impact within the Source Cage.

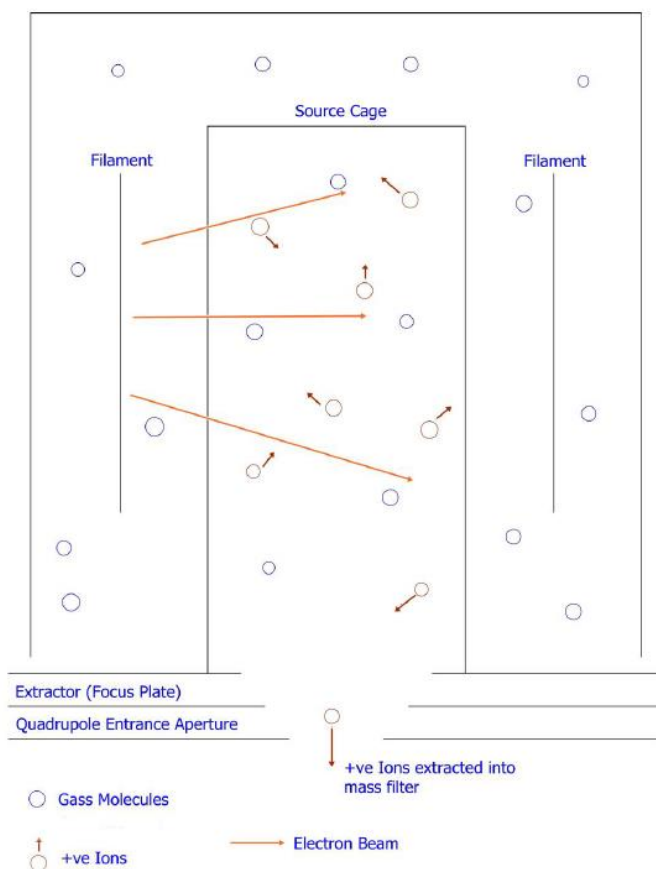


Figure 2. 9 Ion Source

Experiments

The +ve ions produced within the Ion Source are retrieved using the Focus plate, which has a potential of -90V, and then passed via the Quadrupole Mass Filter. Electrons are likewise repelled back into the Ion Source by the Focus plate, preventing them from entering the Mass filter. Mass Separation is enabled by applying RF and DC voltages to the basic Mass filter, or Single Filter. On the mass filter, each mass has a unique RF and DC voltage that allows it to pass through to the detector.

The Faraday Bucket is the most basic detector. It is just a passive conductor in the form of a cup that gathers the +ve Ions that pass past the mass filter.

When the +ve Ions reach the Faraday Bucket, they produce a charge equal to 10^{-4} Amps/Torr for Nitrogen, which implies that 1 Torr (Partial Pressure) of Nitrogen will generate a 10^{-4} Amps Ion Beam.

With a Faraday bucket, the least observable partial pressure is in the range of 10-11 Torr, which is comparable to 10-15 Amps of Ion Current.

The HAL 201-gauge head contains two detectors: a Faraday Bucket and a Secondary Electron Multiplier (SEM).

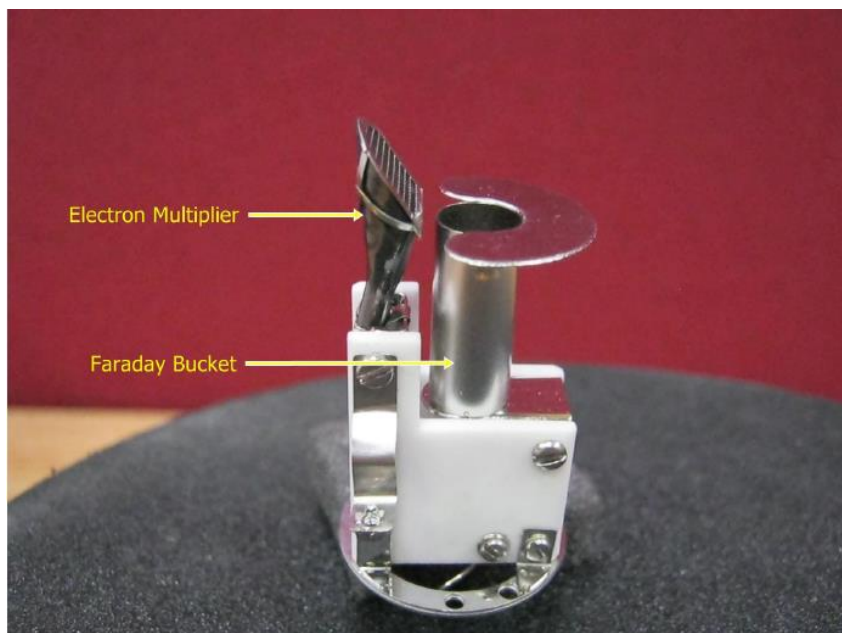


Figure 2. 10 Detector with Dual Faraday/Secondary Electron Multiplier

The surface of the Electron Multiplier is intended to create secondary electrons. A single ion colliding with the surface creates (potentially) two or three electrons, which then move down the detector's 'trumpet,' causing further collisions with the surface, which generate more Electrons in a cascade effect until it reaches the collector.

A voltage delivered to the SEM provides the power for the cascade generation. The total gain gained by the SEM above is normally 103 or 1000 gain. Depending on the system type and application, the voltage used to generate this gain ranges from 800V to 3000V.

Each gas molecule has a unique breaking pattern, often known as a spectral fingerprint. When a molecule is ionized, it fragments, resulting in practically every species being represented by a family of ions with different mass/charge ratios. As a result, the spectra generated may be decoded by determining which family groupings they belong to.

Experiments

Consider Carbon Monoxide (CO), a basic molecule composed of Carbon (C) and Oxygen (O): the molecular weight of carbon is 12 and the molecular weight of oxygen is 16. As a result, since Carbon Monoxide (CO) has a molecular weight of 28, it will be detected by the Mass Spectrometer at that molecular weight, however there are other elements to consider, such as Doubly Charged Peaks.

CO loses an electron in the Ion Source when it generates a +ve ion, which is denoted as CO⁺. The ratio of CO⁺⁺/CO⁺ is repeatable for a particular instrument because some of these ions will lose an extra electron and become doubly charged CO⁺⁺. This ratio is quite tiny for CO (0.005% of Mass 28), but it is closer to 0.1 percent for other species, such as Nitrogen and Argon. The molecular weight of these Doubly Charged Peaks Ions is half that of the 'Parent' ion.

Fragmentation peaks emerge when gas molecules fragment; in CO, the fragmentation process produces Carbon Ions (C⁺ at mass 12) and Oxygen Ions (O⁺ at mass 16).

Most atomic species have related Isotope Peaks; for example, Carbon has an Isotope Peak at mass 13 (C13 0.011 percent of mass 12) and also at mass 14, although the latter is so minor that it is usually overlooked. O17 (0.0004 percent of mass 16) and O18 (0.0004 percent of mass 18) are isotopes of oxygen (0.002 percent of mass 16).

As a result, the fragmentation of a simple molecule like CO may be complicated, with numerous distinct peaks seen at the 1% component level.

The existence of the distinctive cracking pattern may therefore be used to determine the presence of CO.

This is quite straightforward for basic RGA applications, with the major goal being to ensure that the vacuum system state is constant. Hydrogen, Helium, Water, Air, and Argon are readily recognised as components of interest.

More complicated species may be more difficult to understand, but there are a variety of tools available, ranging from Cracking Pattern tables to sophisticated spectrum libraries, some of which are built into the Mass Spectrometer.

All the data collected by the mass spectrometer are analysed through MASsoft, the relative software of Hiden for the use of the instrument.

After the mass spectrometer is connected to the outlet of the hydrogen separator with a T connection a new scan can be started in MASsoft.

There are different types of scan mode to choose, the one chosen for our experiments is the MID mode scan.

MID mode, (Many Ion Detection) brings up the MID Mode box, which let set up a trend scan with a single or multiple masses, as well as design a scan using components from the internal library.

All data and photos of mass spectrometer are taken from direct experience and from the user manuals. [49], [50]

2.3 Experiments performed

During my stage at Environmental Park, the following experiments were carried out in the electrochemical electrolyser described above:

- Polarization test
- Degradation test

2.3.1 Polarization test

Before starting the degradation, a series of experiments for obtaining the polarization curves of the cell were performed and are reported in this chapter.

Polarization tests are part of the experimental measurements, the primary goal is to identify the change in voltage induced by a change in the provided current under steady-state circumstances. The tests were carried out at a constant temperature and outlet gas pressure, and the results were obtained by interfacing the power supply with the LabView user interface and specifying the major parameters for each step: current, pressure, and temperature.

Because the voltage changes throughout the time step, the time step length was set equal to 270 s, an interval of time long enough to let the voltage converge.

To stabilize the voltage curve, all tests were performed ascending the input current density from 0 to 2 A/cm² and descending from 2 to 0 A/cm².

The divergence between the two curves is owed to hysteresis events associated to the stability of the key thermodynamic parameters throughout the experiments.

Some of the Polarization test showed in this chapter are performed with the closed cathode.

In the electrochemical cell used, both anode and cathode have the water inlet to improve the thermal stability.

PEM electrolyser works better at higher temperatures and lower pressures, closing the cathode water inlet the temperature is higher keeping constant the pressure.

Because high temperatures lower the potential needed to break the water molecule, the mass flow of hydrogen rises as the temperature and electrolyte concentration rise. At the various currents examined, the resistance also decreases with increasing electrolyte content and temperature. This is explained by the mass transfer events that occur in the electrolyzer, which favour molecular collisions between electrolyte ions as temperature rises.

In this thesis only the Polarization curves tests are reported for what regards the open/closed cathode comparison, in order to validate the Comsol model.

Experiments

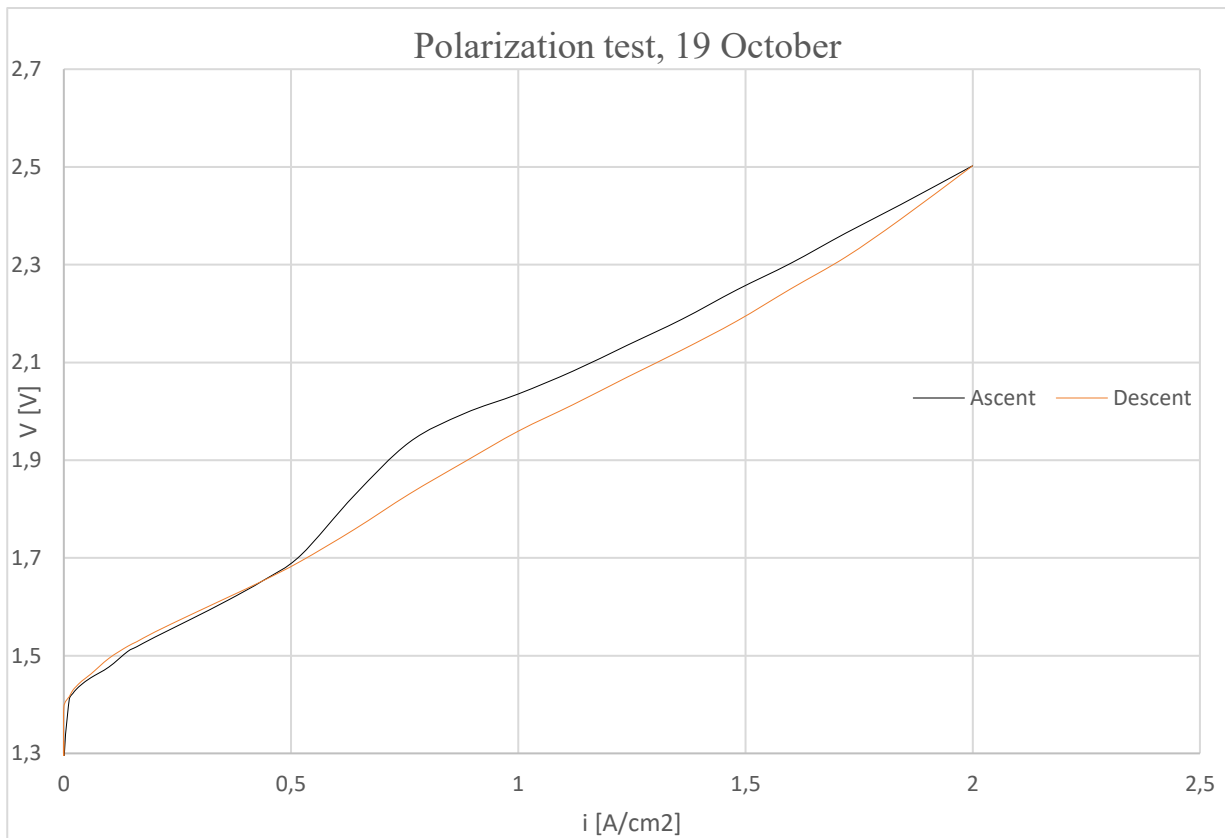


Figure 2. 11 Polarization curve with closed cathode configuration, $T = 80$ °C, $p = 0.5$ bar, mass flow rate = 20 %

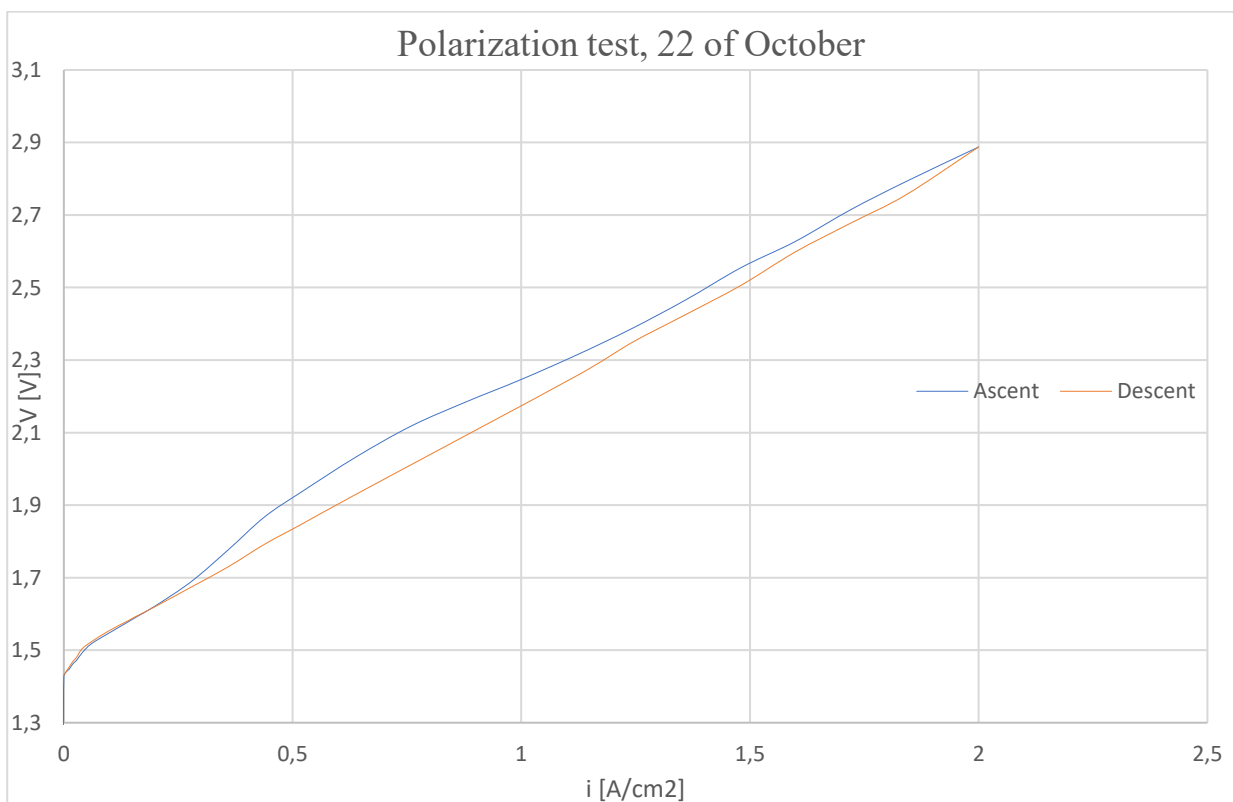


Figure 2. 12 Polarization curve with closed cathode configuration, $T = 60$ °C, $p = 0.5$ bar, mass flow rate = 10 %

Experiments

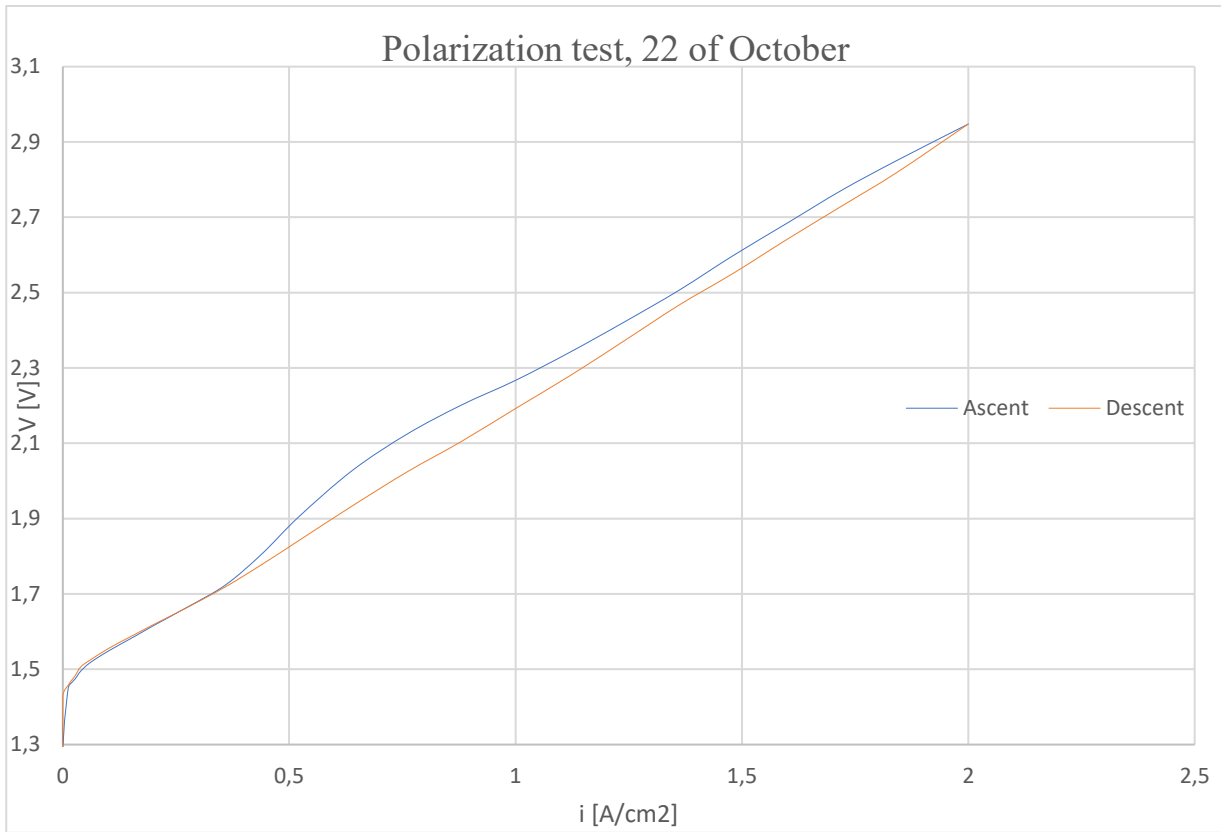


Figure 2. 13 Polarization curve with open cathode configuration, $T = 60$ °C, $p = 0.5$ bar, mass flow rate = 10 %

2.3.2 Degradation test

The objective of the degradation test is to get a better knowledge of the key operation phenomena, such as electrochemistry, transport phenomena, thermodynamics, and the processes leading to cell component degradation, in order to allow prediction of their performance and durability.

The degradation test started on the 20th of January and ended on the 10th of March. The test was stopped from the 4th of February until the 8th of March for maintenance of one Back Pressure Controller of the test bench. For the complete duration of the test, the water tank was refilled with distilled water every 10 to 12 hours.

The objective of the experiment is to test the correct functioning of the mass spectrometer.

The mass spectrometer was turned on the 25th of January and run until the 10th of March 2022, (except during the stop for maintenance) when the degradation test ended.

When the production is zero is because the machine tripped: to work properly, the pressure at the inlet of the spectrometer must be under 9×10^{-5} Pa, when the pressure rises upon this value the scan stops.

This rise of pressure is mainly due to leakage in the T connection of the spectrometer and can be resolved by simply starting a new scan, or manually by reducing the pressure at the connection.

The species scanned were nitrogen, oxygen, hydrogen, and water.

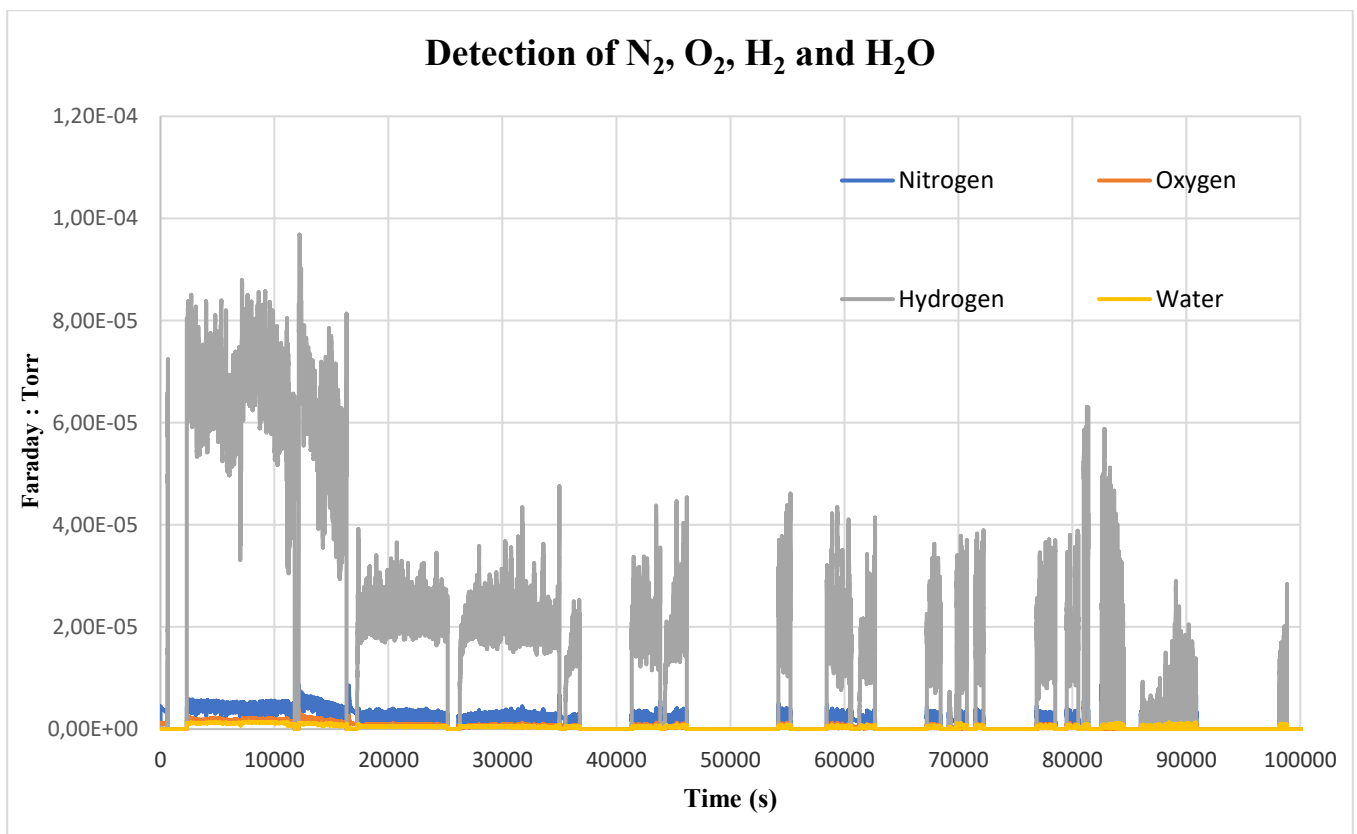


Figure 2. 14 Spectrometer data of N₂, O₂, H₂ and H₂O

Experiments

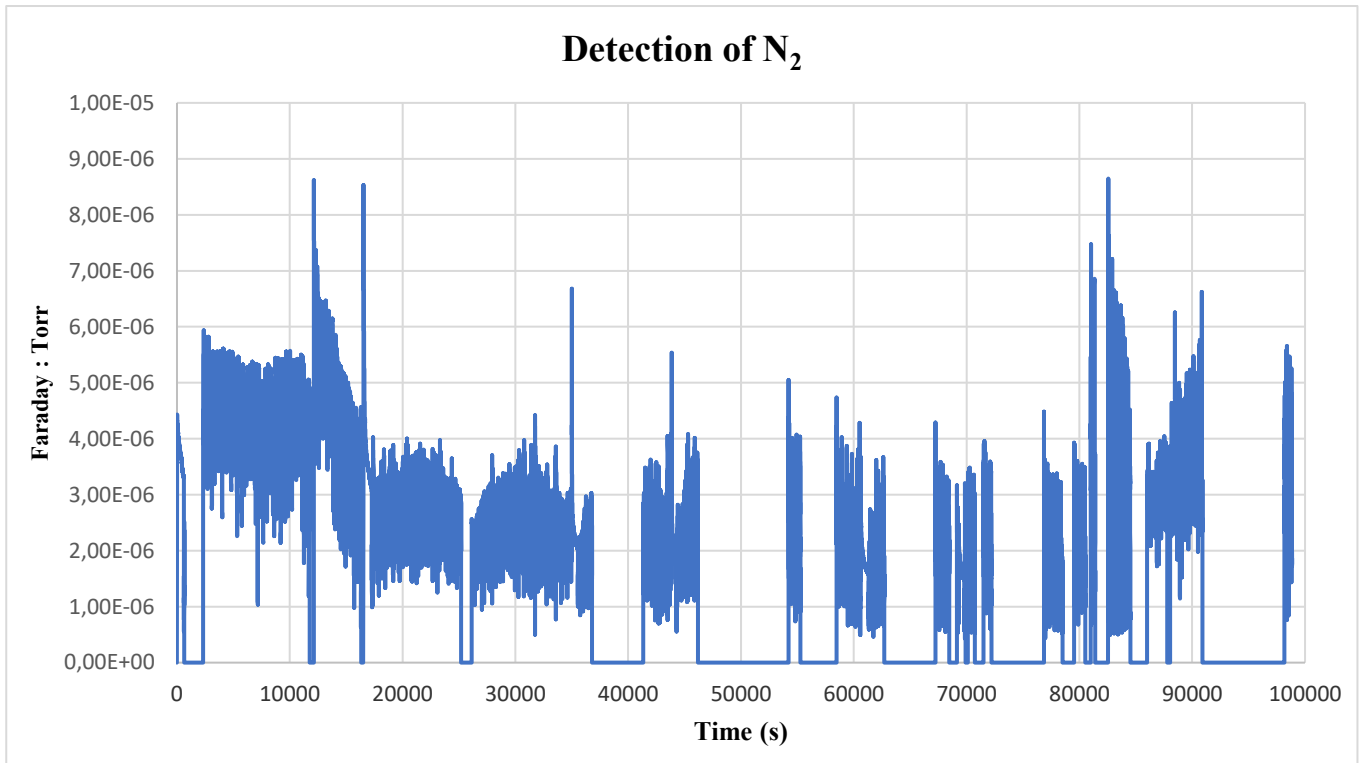


Figure 2. 15 Spectrometer data of Nitrogen

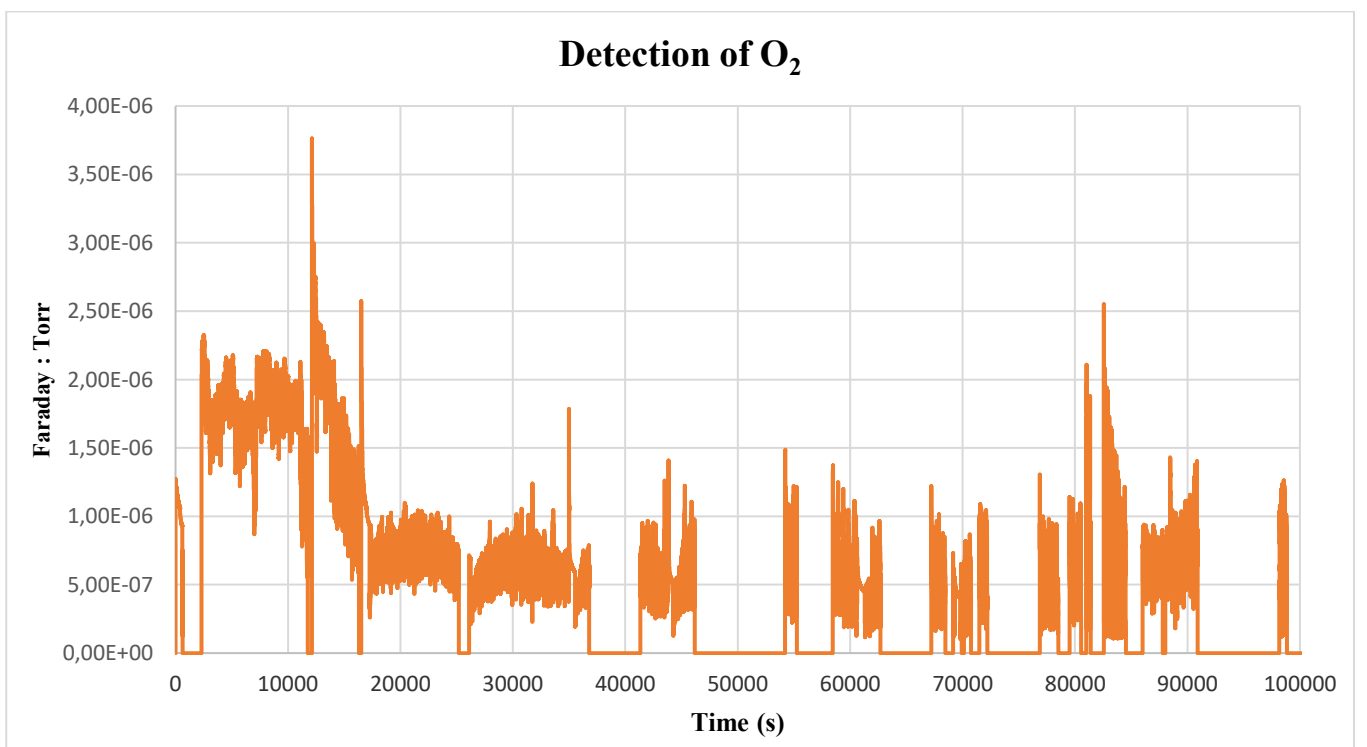


Figure 2. 16 Spectrometer data of Oxygen

Experiments

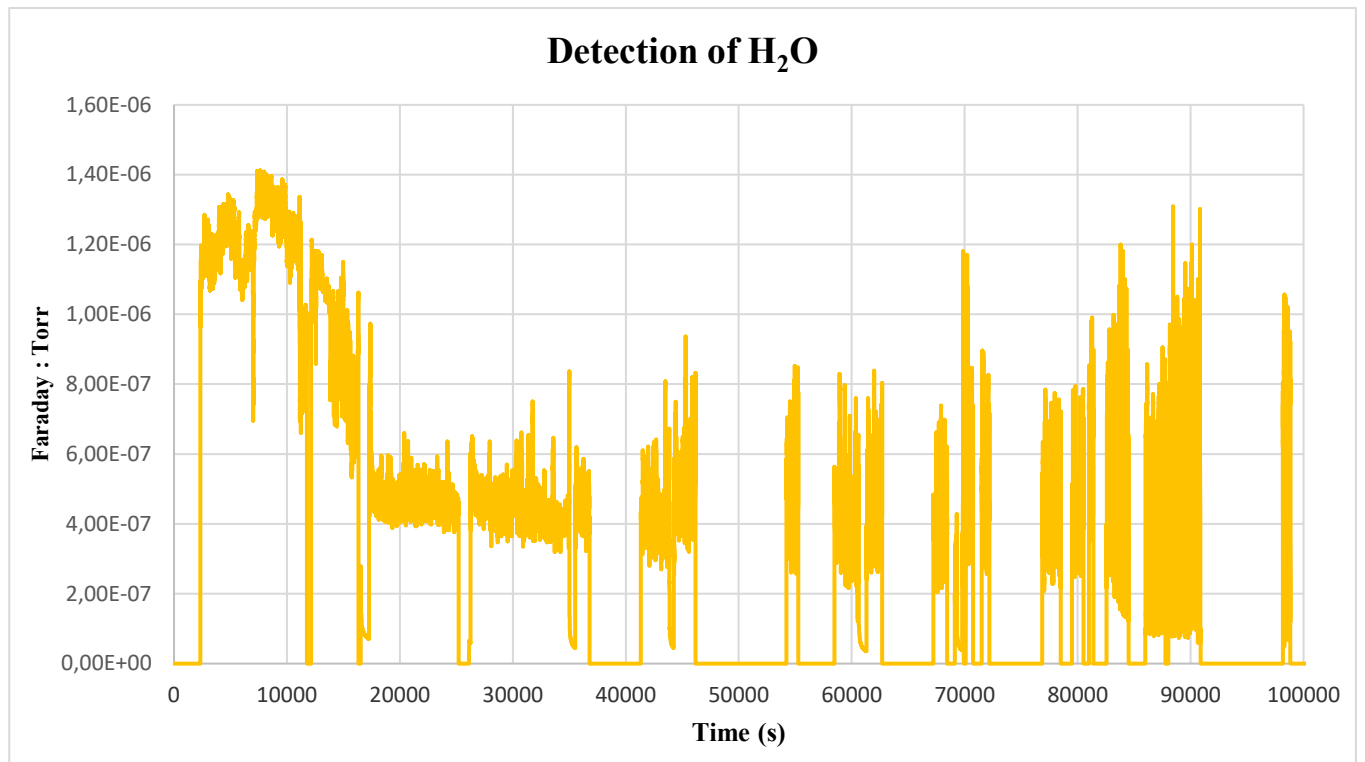


Figure 2. 17 Spectrometer data of Water

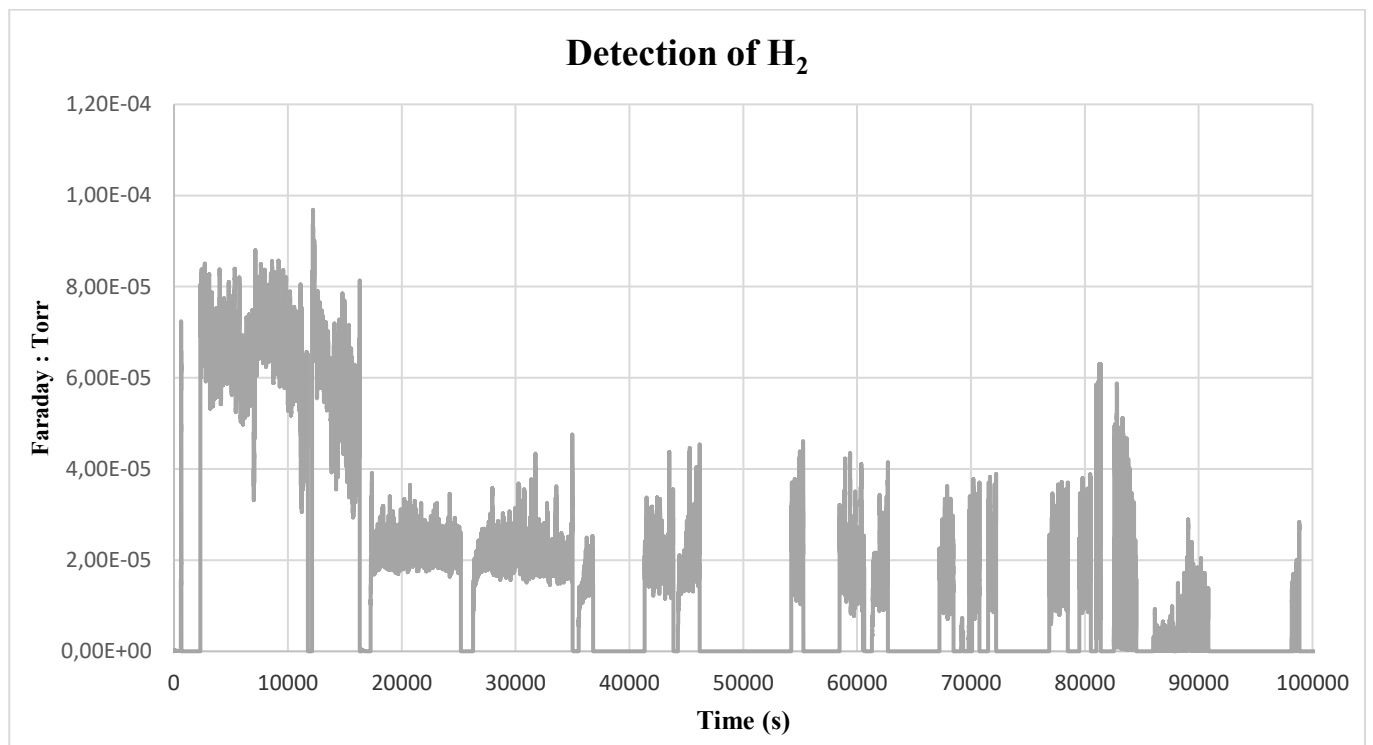


Figure 2. 18 Spectrometer data of Hydrogen

Experiments

A first interesting data to analyse is the comparison between the hydrogen output at the beginning of the test versus the last week:

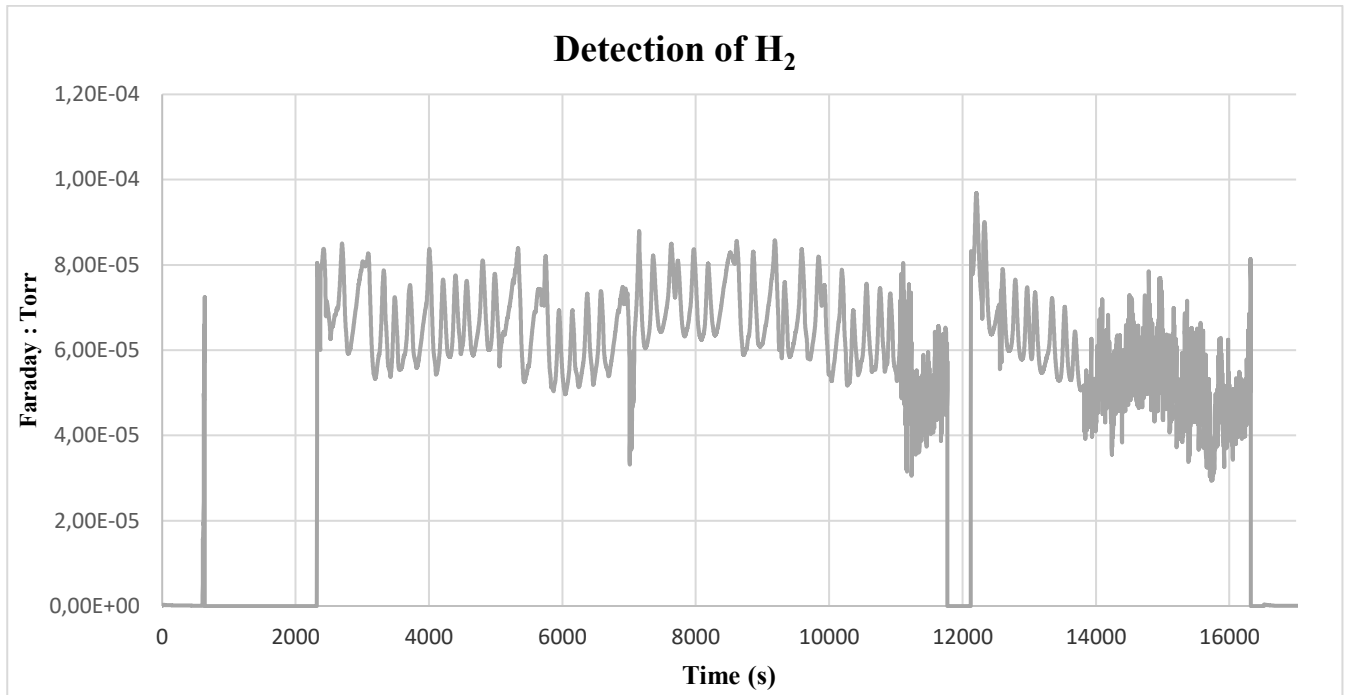


Figure 2. 19 Spectrometer data of Hydrogen of the first two days

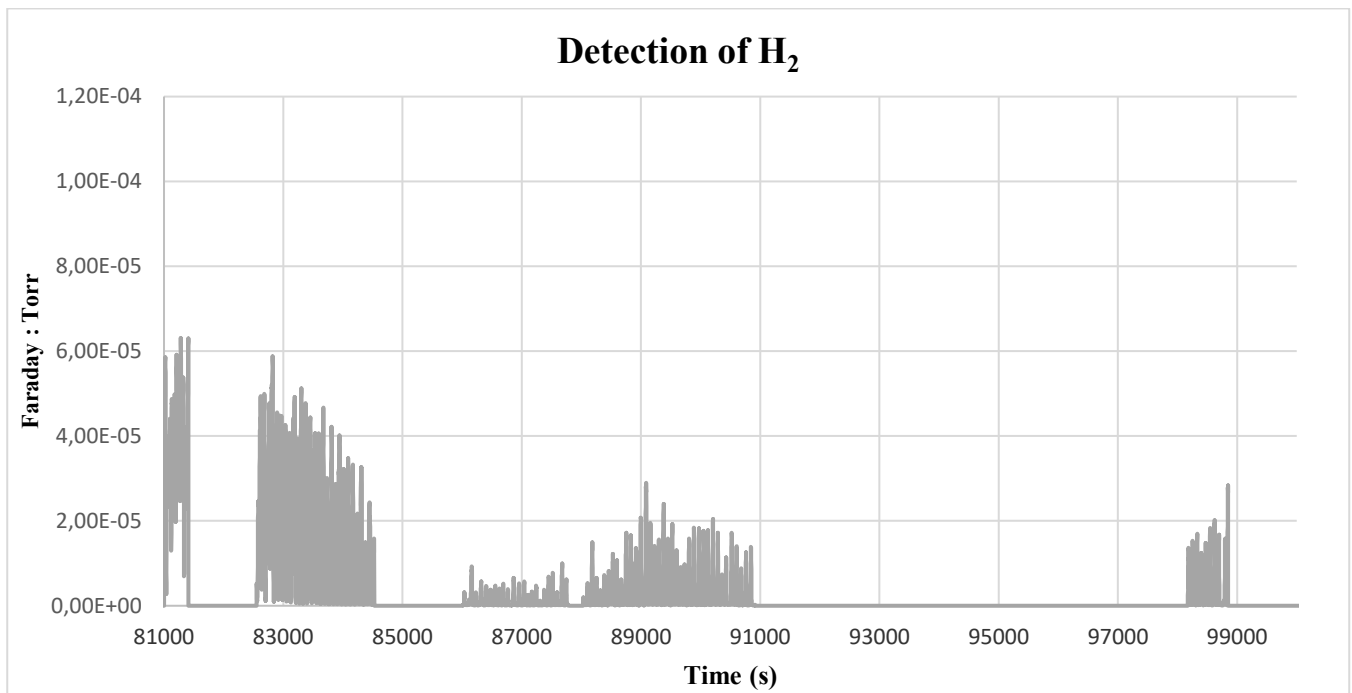


Figure 2. 20 Spectrometer data of Hydrogen during the last two days

As shown in figure 2.19 e 2.20 the Hydrogen detection is significantly lower in the last two days of the test since the cell is degrading.

Experiments

Water is detected since a percentage of evaporated water is present in the separation tank.

Oxygen and Nitrogen are scanned because they are included in air, that flows in the tube, if the production of hydrogen is higher than oxygen and nitrogen, it means that the spectrometer is working, since we are producing hydrogen.

To prove it, the previous plots are presented below now with the concentration ratio on the y-axis, that is the percentage of the species under study versus the total species at the outlet of the separator at cathode side.

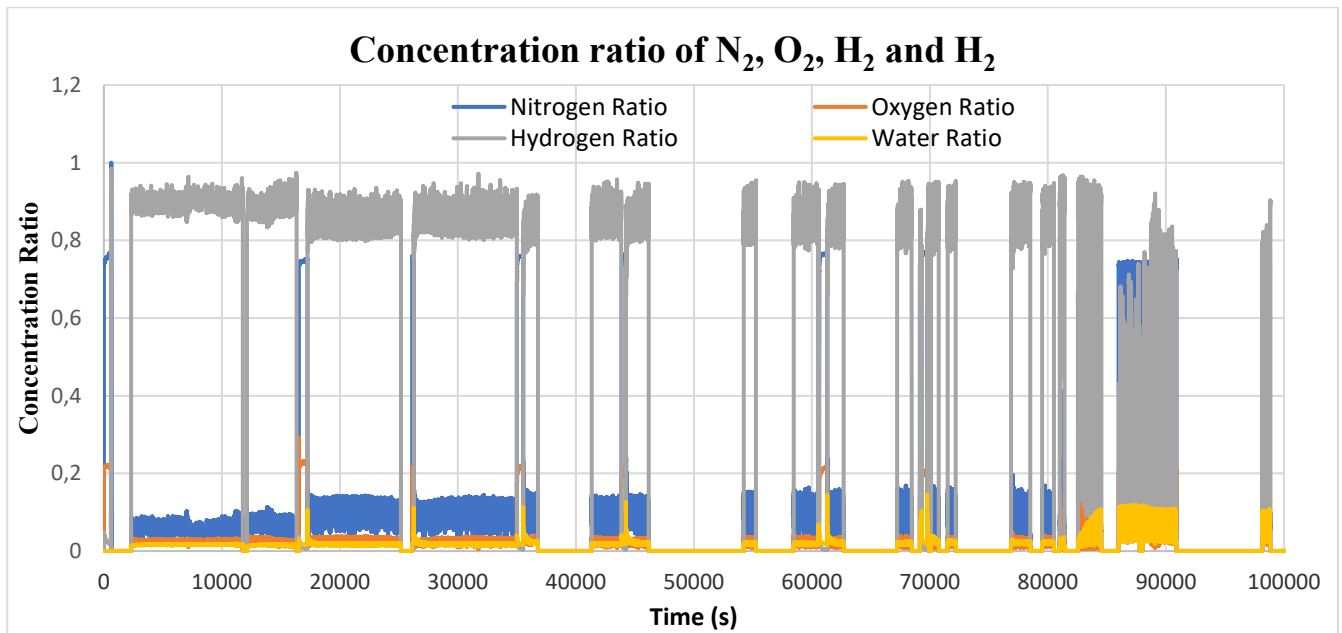


Figure 2. 21 Concentration ratio of N₂, O₂, H₂ and H₂

As we can see from figure 2.21 and 2.22 the hydrogen concentration is higher than the other specimens. Is between 80 % and 93 %. This means that the mass spectrometer is working properly, and the hydrogen is being produced.

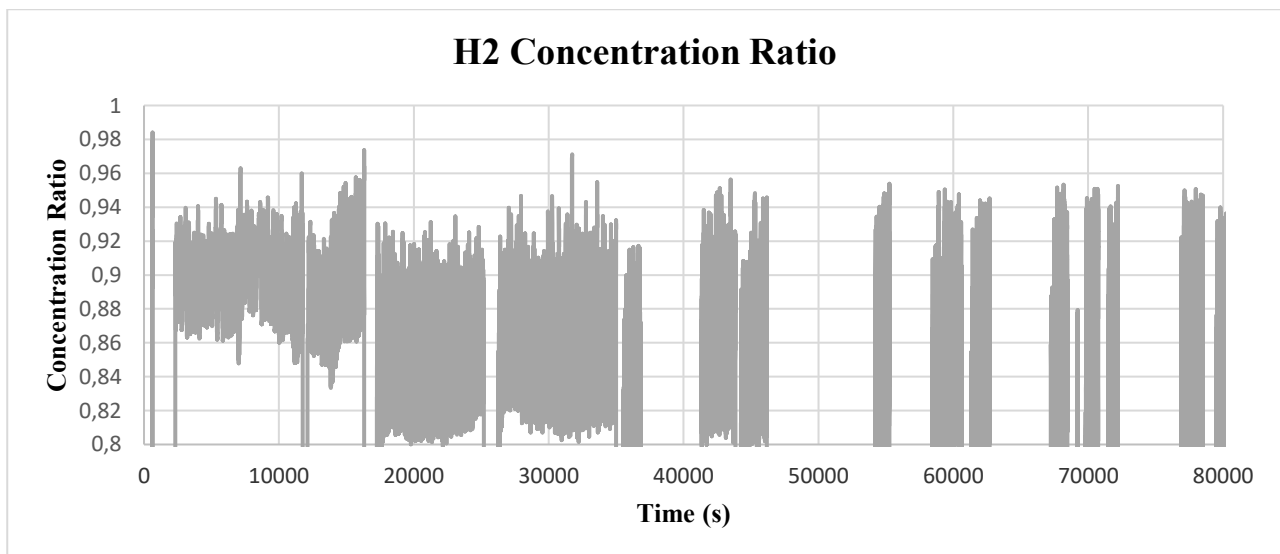


Figure 2. 22 Hydrogen percentage

Experiments

The first analysis of the data of the degradation test is by the comparison of the voltage and the hydrogen percentage during a period when both parameters are steady.

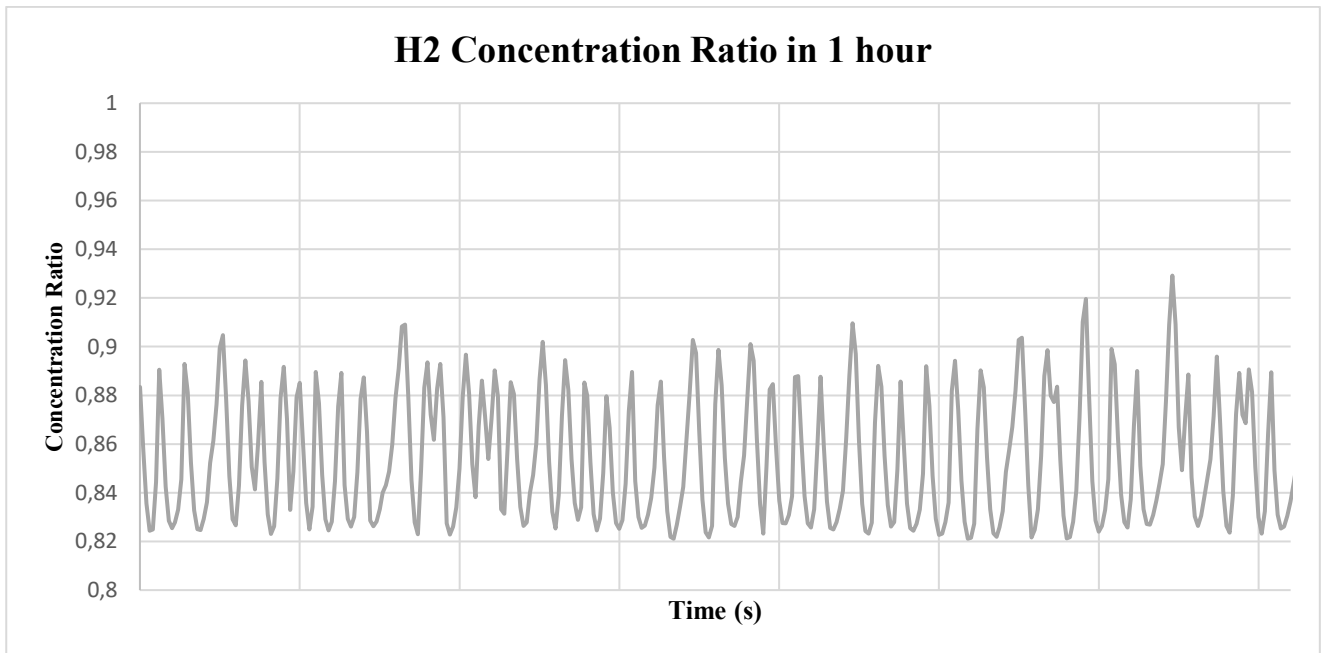


Figure 2. 23 Hydrogen percentage in one hour of steady functioning

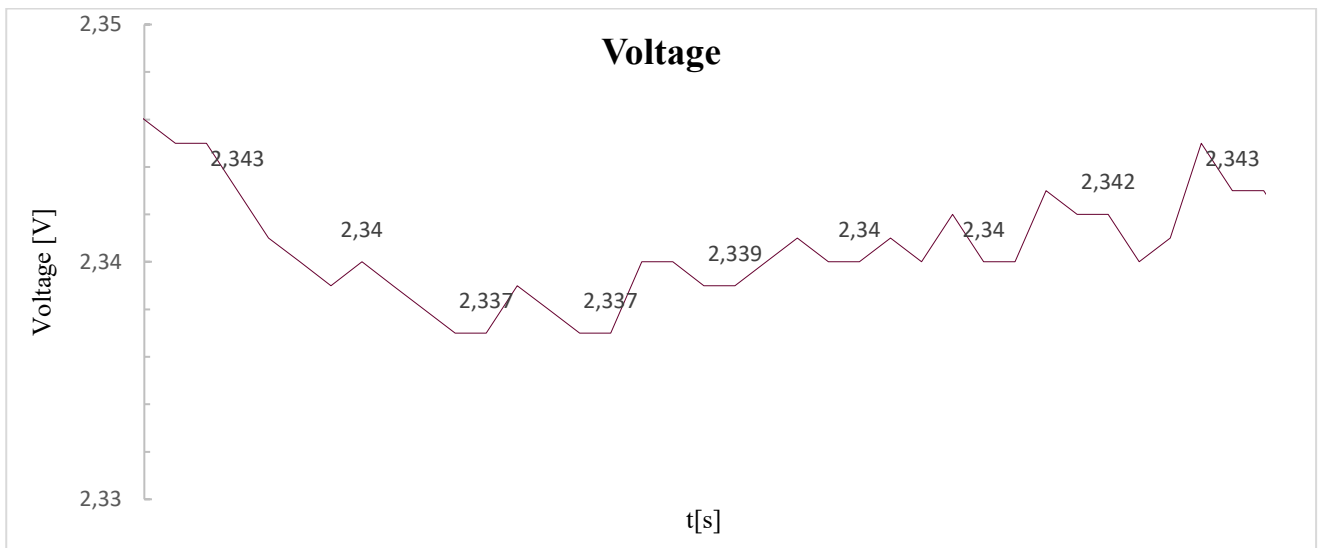


Figure 2. 24 Voltage values in one hour of steady functioning

As can be seen from the figures above (2.23 and 2.24), there are not anomalies or changes during a one-hour production between the voltage trend, which remains constant, between 2,337 V and 2,343 V, and the Hydrogen percentage.

Experiments

During the spectrometer analysis a possible problem that must be avoided is that the tube connecting the separation tank and the mass spectrometer is already saturated with hydrogen.

The production of hydrogen must have the same trend of the pressure at cathode side, since when the valve of pressure at cathode side is open (pressure higher than 0.5 bar) a release of cathodic water is present in the separation tank, with a rise of oxygen. If the hydrogen production rise even when there is not a release of pressure, it means that the tube is saturated, and the connection should be checked again.

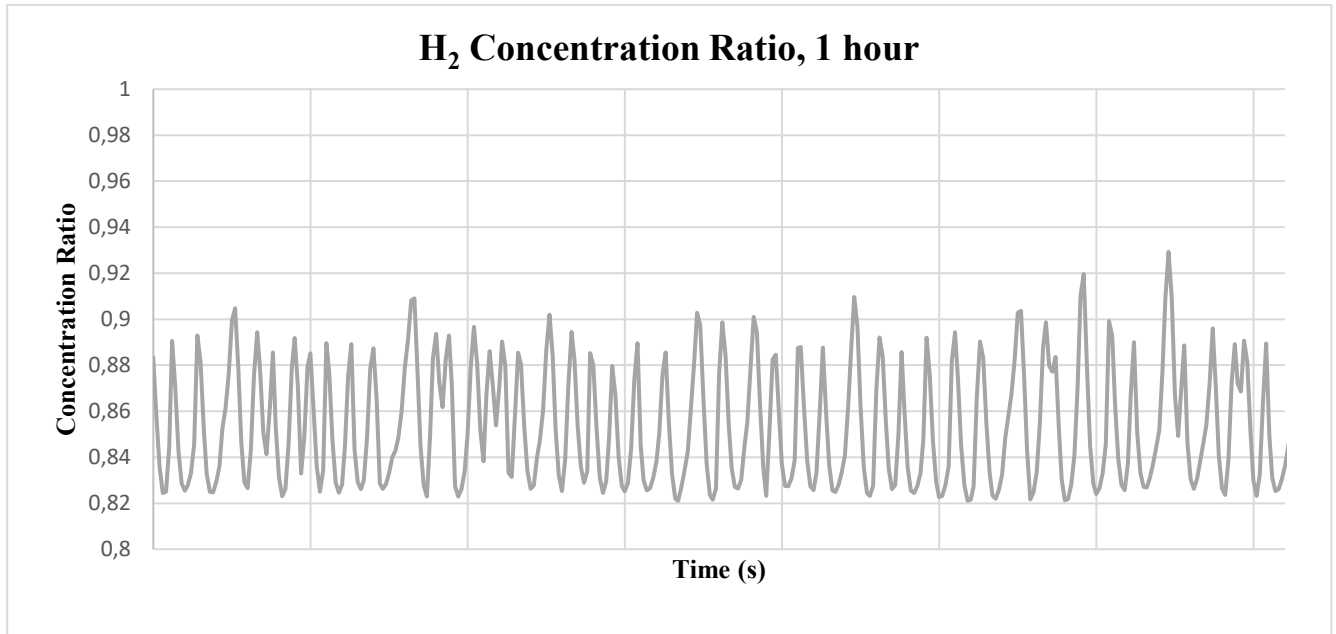


Figure 2. 25 Hydrogen percentage in one hour of steady functioning

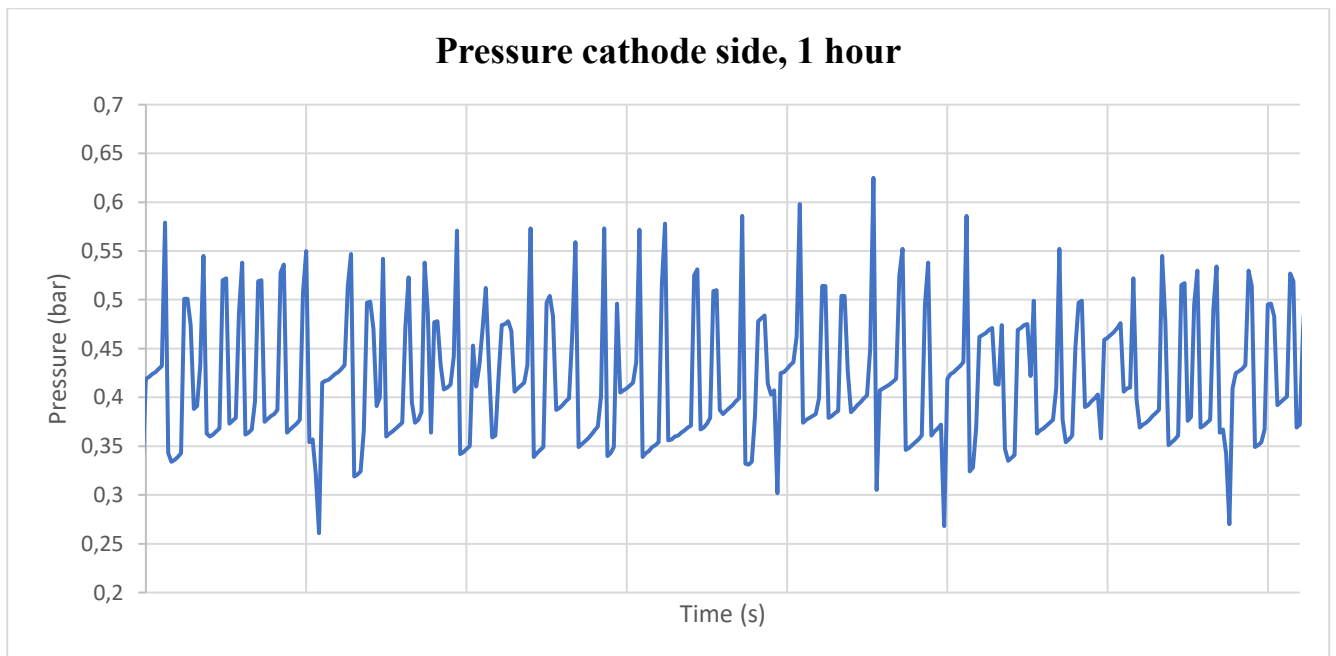


Figure 2. 26 Pressure at cathode side, one hour

Experiments

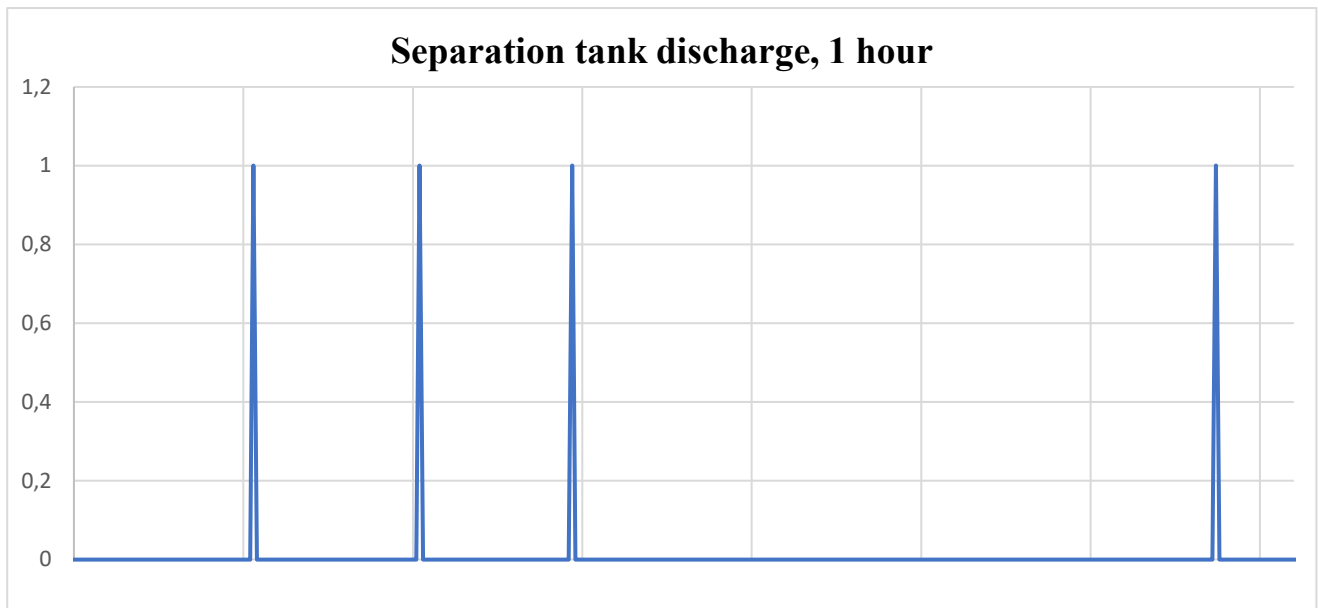


Figure 2. 27 Separation tank charge/discharge in 1 hour. When the valve is at 1, the water is discharged

From figure 2.25 and 2.26, the percentage of hydrogen and the pressure at cathode side have the same trend: the tube was not saturated, and the experiment is valid.

Another important proof that validated the experiment can be evaluated from the comparison of pictures 2.25 and 2.26 with 2.27, that is the discharge of water of the separation tank.

When water is discharged, it should correspond to a pressure drop on the cathode side, since we have a release of pressure in the system, and hydrogen concentration ratio that still goes up, related to the discharge of the separation tank. If this is proved, it means the connection was done properly and the experiment is valid.

From the comparison of the plot above, it can be seen that for every discharge of water the pressure at cathode sides drops and the hydrogen concentration ratio still rise. The experiment is acceptable.

2.3.3 Water consumption

Water consumption was constantly monitored in order to make a comparison with the hydrogen produced, to have an idea of the efficiency of the electrolyzer.

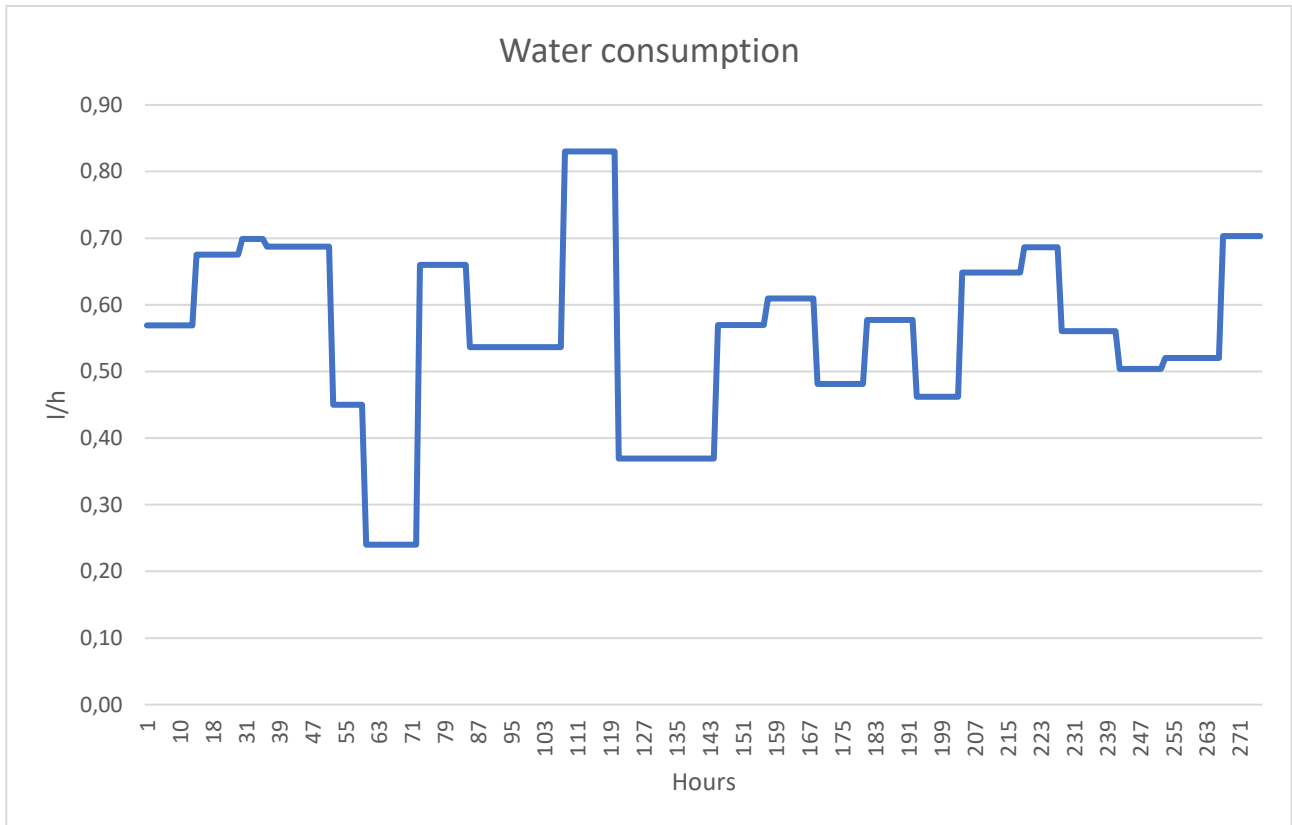


Figure 2. 28 Water consumption during degradation test

Chapter 3

Modelling

This chapter is devoted to a detailed examination of the modelling possibilities of PEM electrolysis. The model has been focused directly on the electrolytic cell used in the tests and on the test bench through boundary conditions.

The model was built for both 2D and 3D geometry in the Comsol Multiphysics 5.6, a Multiphysics simulation and finite element analysis program.

General assumptions, mathematical formulation, computational domain, geometry and mesh, boundary conditions, numerical implementation, and calculation technique are all components of the model, later in this chapter are deeply analysed into detail.

3.1 Geometry

First of all, the 2D Model geometry is introduced.



Figure 3. 1 2D Geometry

The 2D geometry consist in rectangular blocks, that represent respectively, from left to right:

- Anodic Bipolar plates in Titanium.
- Anode Electrode.
- Proton Exchange Membrane Electrolyte.
- Cathode Electrode
- Cathodic Bipolar plates in Graphite.

Modelling

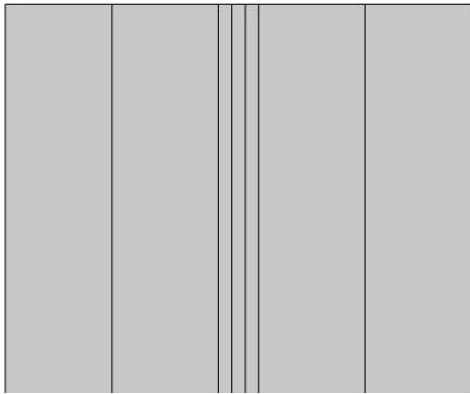


Figure 3. 2 Closeup of the 2D Geometry

The 3D Geometry used in the Comsol model, on the other hand, represent with fidelity the original model. In the reproduction trough Comsol editor the real measurements have been used.

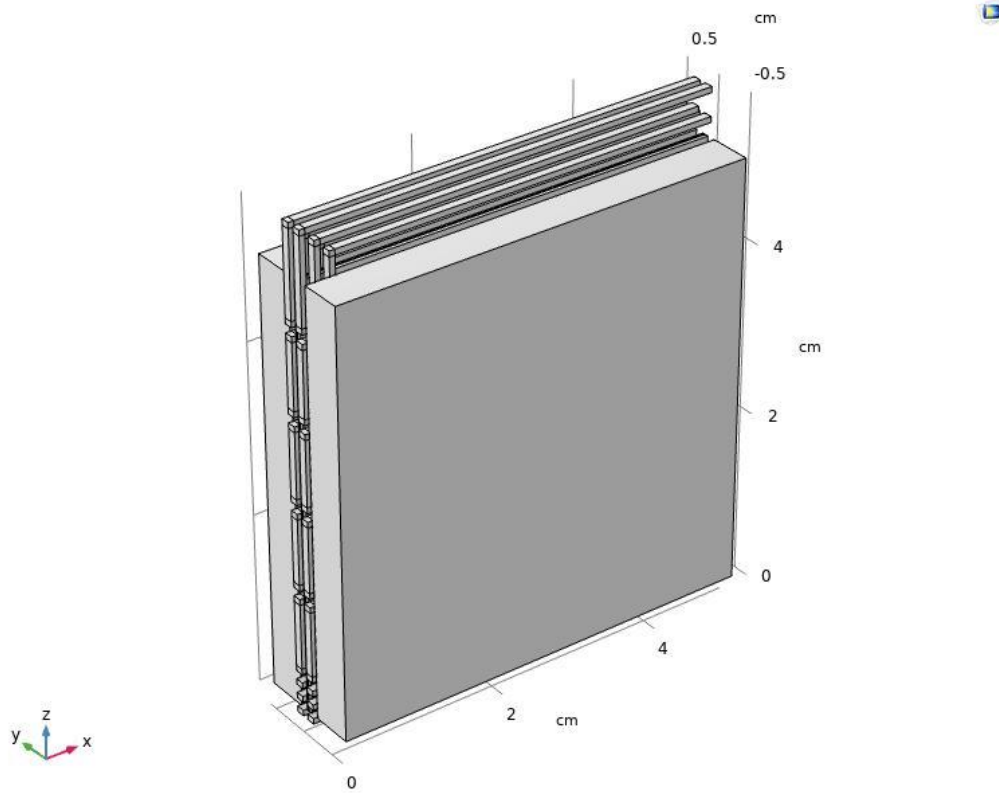


Figure 3. 3 Geometry of the 3D Model

Modelling

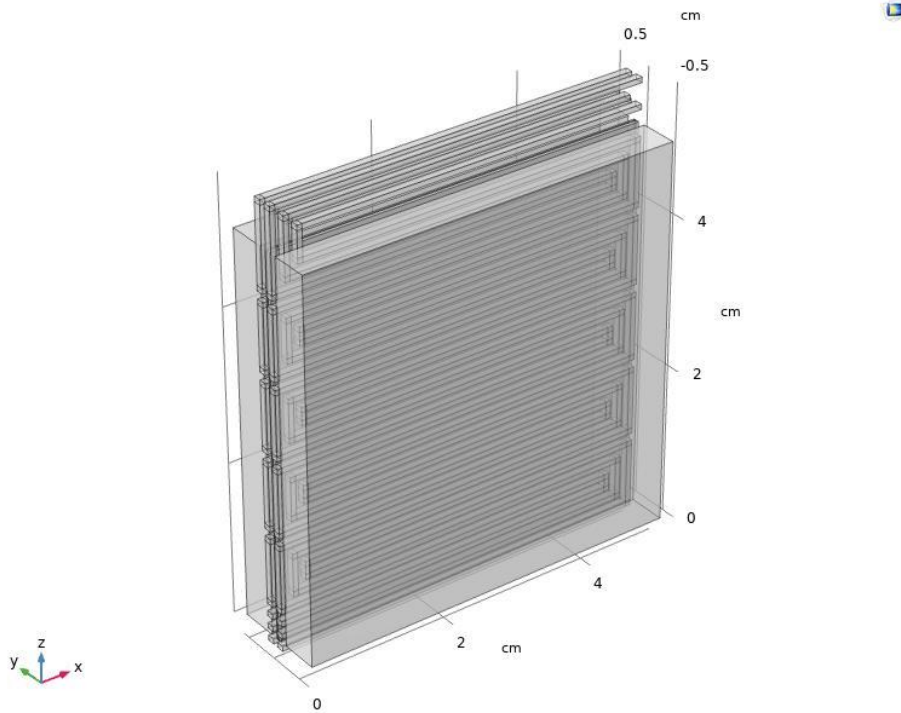


Figure 3. 4 Geometry of the 3D Model with transparency

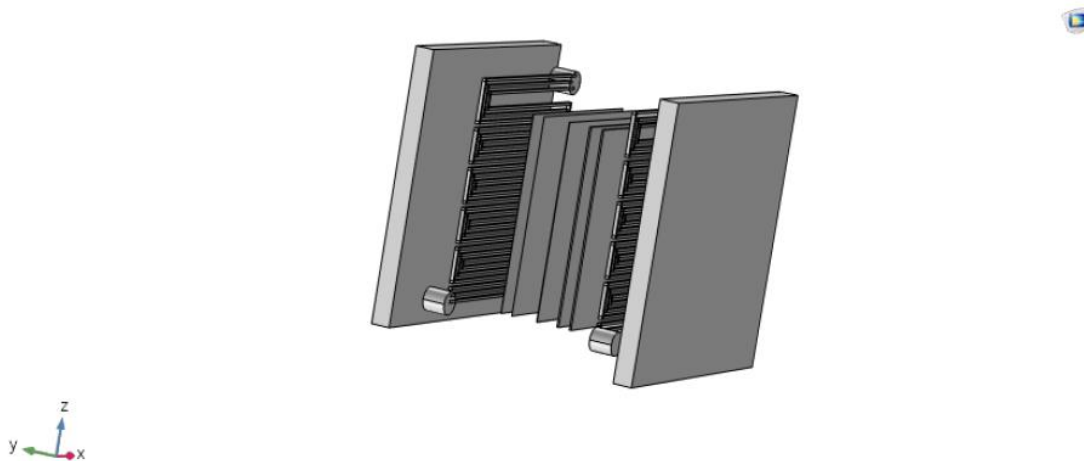


Figure 3. 5 Overview of the 3D geometry

In figure 3.4 we can see the 3D model with transparency in order to have a clearer view of the inside.

The main parts, as for the 2D model are:

- Anodic Bipolar plates in Titanium and Cathodic Bipolar plates in Graphite, that are the rectangular blocks respectively at right and left in figure 3.5
- Anode Electrode, composed by anode inlet, outlet, anode catalyst layer and the anodic serpentine shaped channels:

Modelling

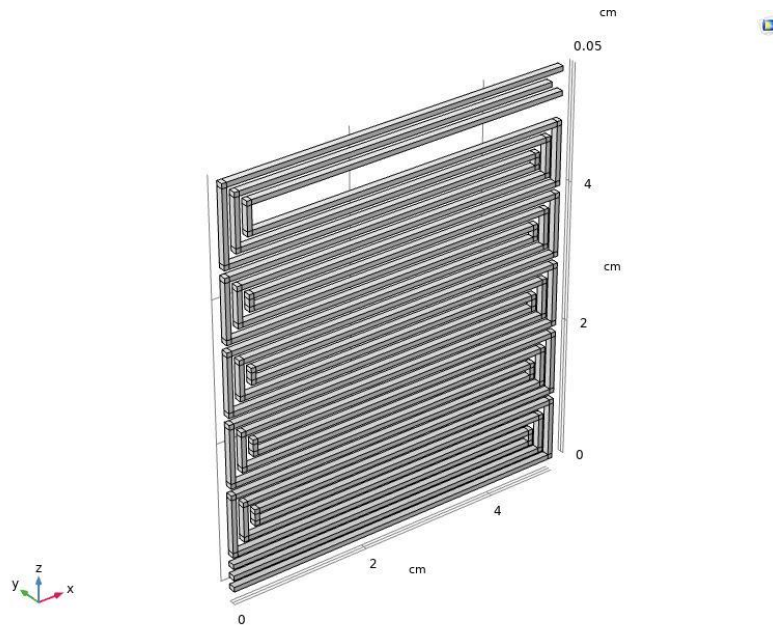


Figure 3. 6 Anodic channels detail

- Proton Exchange Membrane Electrolyte, rectangular shaped membrane made in Nafion 115

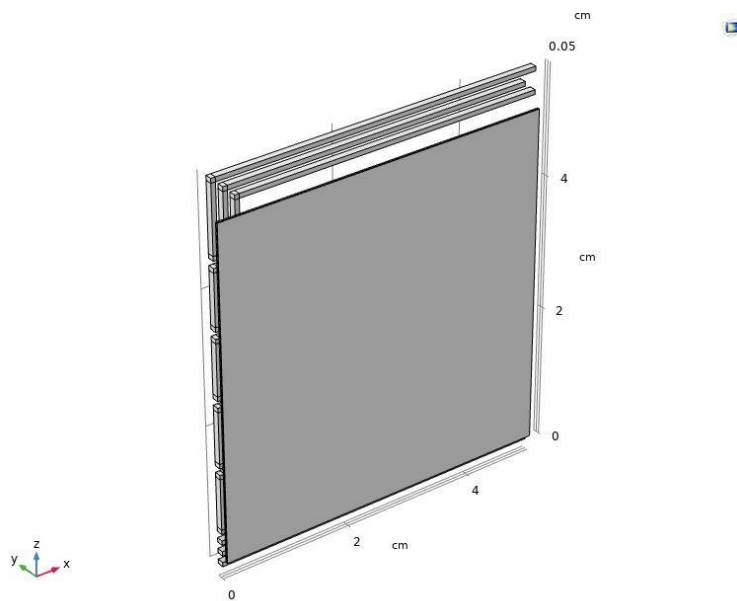


Figure 3. 7 Electrolyte membrane with anodic channels

- Cathode Electrode, composed by anode inlet, outlet, cathode catalyst layer and the cathodic serpentine shaped channels (same shape as anode one).

3.2 Mesh

The mesh used for the 2D model is a user-controlled mesh, a cartesian grid block-structured mesh was chosen.

The mesh density increases from both sides as it gets closer to the electrode/electrolyte interfaces. Because electrochemical processes take place in these areas, a finer mesh is required to accurately reflect the events. The element size and growth factor were designed to balance accuracy and computing time.



Figure 3. 8 2D Mesh

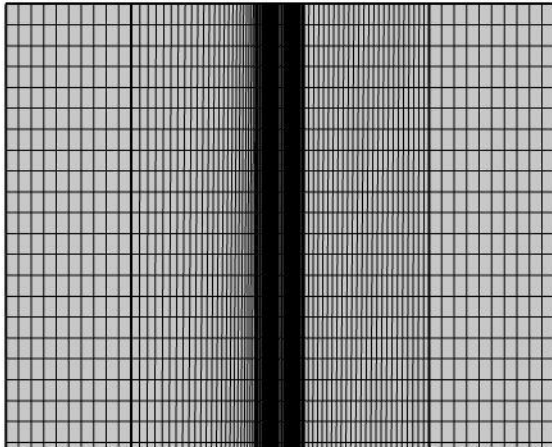


Figure 3.9 2D Mesh, close up

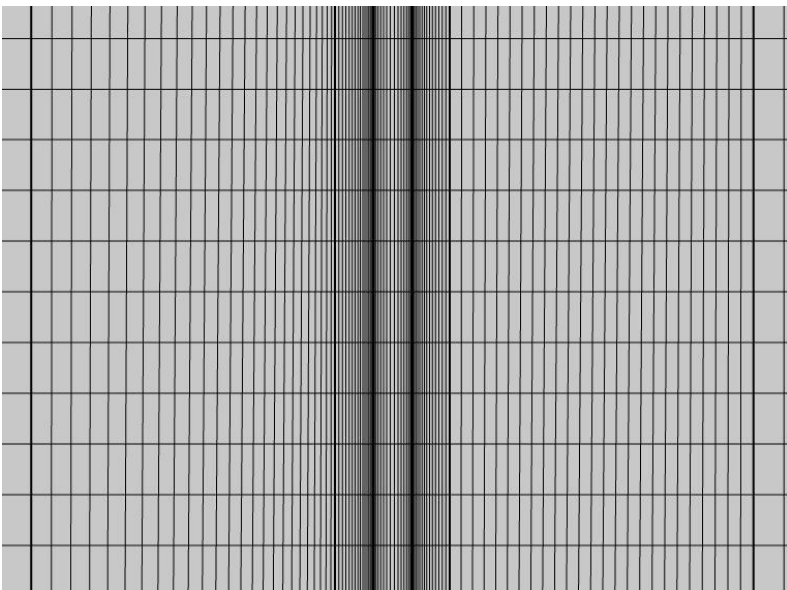


Figure 3.10 2D Mesh, close up of the inner part

In figure 3.10 the finer mesh of the inner part can be seen more clearly.

For what regards the 3D mesh, a Physics-controlled mesh was used. An element size for the mesh from Extremely coarse to Extremely fine from the Element size list can be chosen, in this model a normal type mesh was chosen (default value) in order to avoid very long computational times.

This kind of mesh control recommendations include all mentioned physics interfaces and moving mesh capabilities, later in this chapter all the physics will be analysed.

Modelling

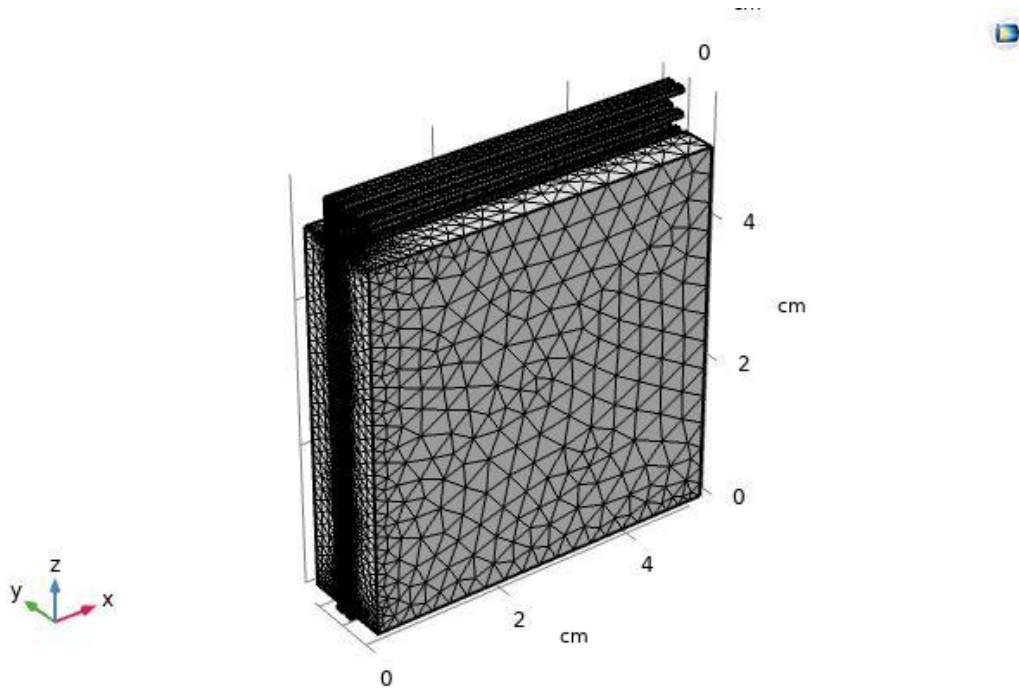


Figure 3. 11 3D Mesh

In this instance as well, the number of components that make up the mesh increases as you go closer to the centre of the cell, particularly in the MEA area and at the corners of the triple serpentine flow field.

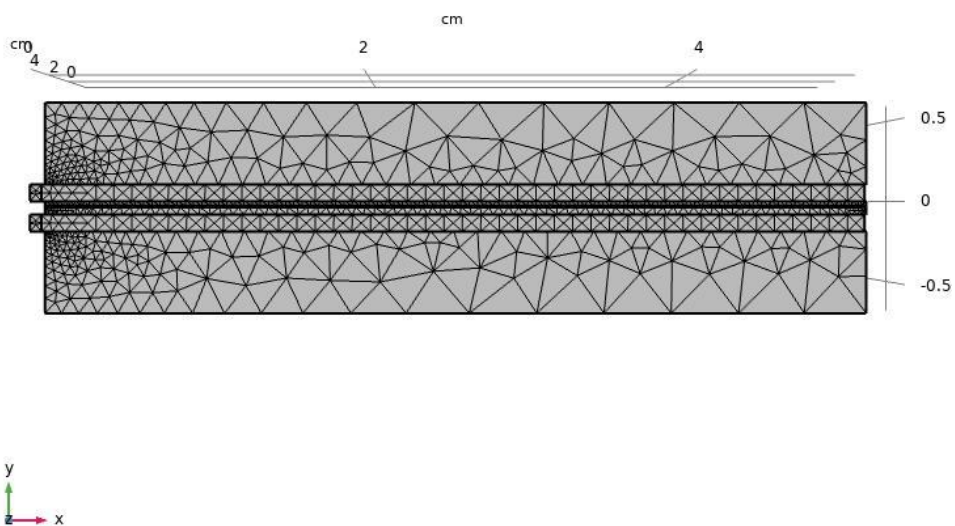


Figure 3. 12 3D Mesh, XY view

Modelling

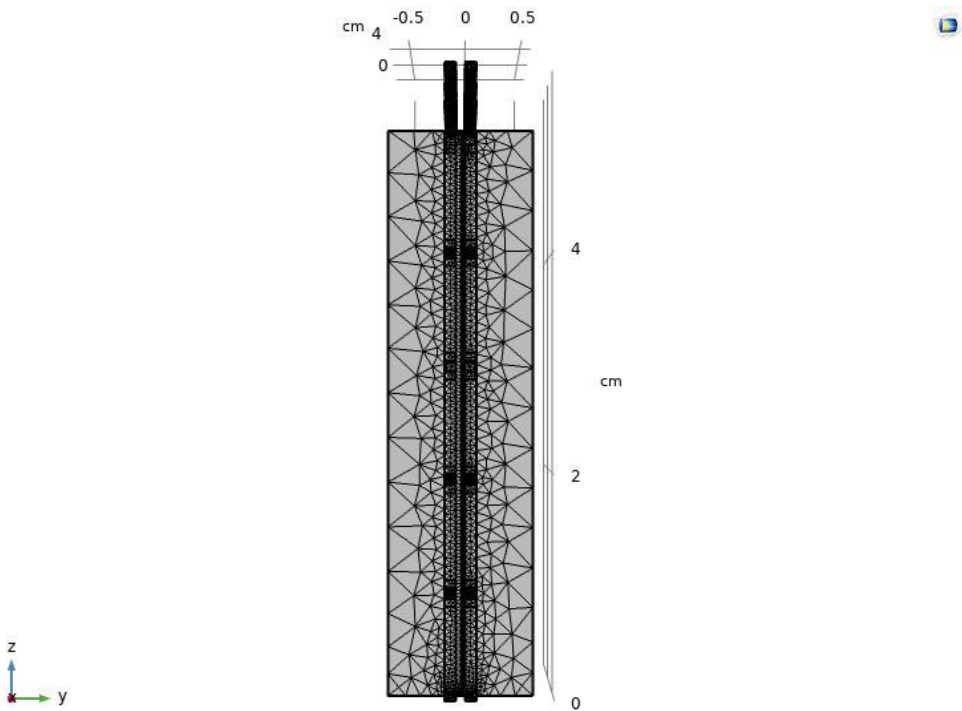


Figure 3. 13 3D Mesh, YZ view

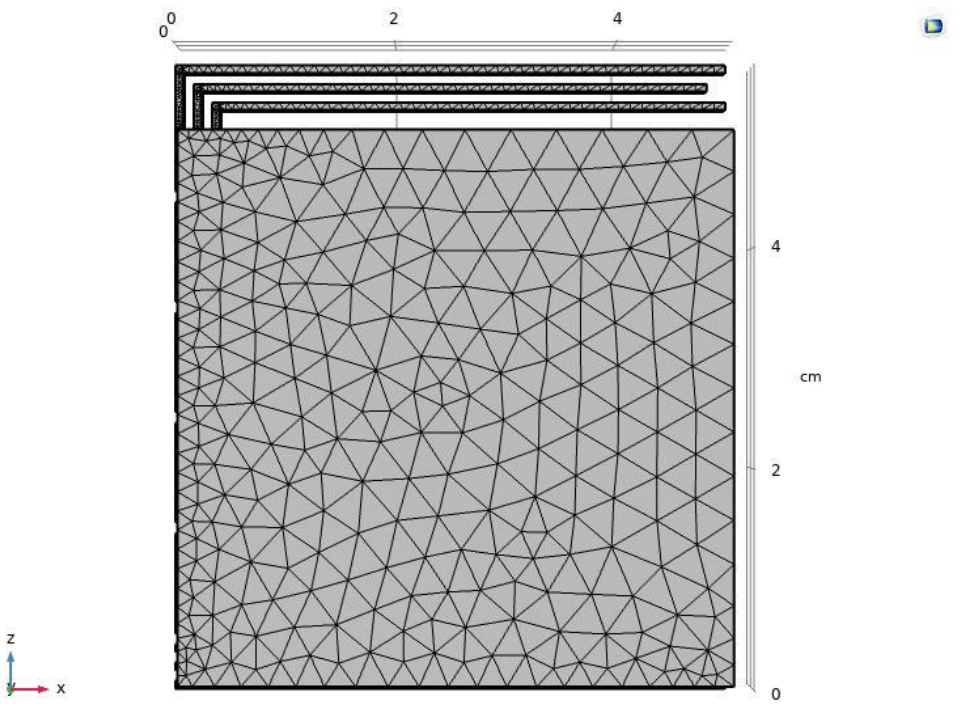


Figure 3. 14 3D mesh, XY view

3.3 Physics

Once the geometry of the cell is built, both in 2D and 3D, physics interfaces are applied in COMSOL in order to apply a predetermined set of equations to run the finite elements simulations to the mesh chosen.

In this paragraph all the modelling equations, boundary conditions and hypothesis made to build the COMSOL models are reported.

3.3.1 Water Electrolyzer

The first physics applied to the model is the Water Electrolyzer one. The electrode and electrolyte phase potentials of the different electron and ion-conducting layers of various kinds of water electrolyzer cells, are solved using this physics interface.

The first modelling assumptions is that the initial value of the electric potential Φ_l on all the cell domain is equal to 0: the electric potential is the dependent variable of the electrolyte phase, that affects all the cell domains.

The following equations are evaluated in the Electrolyte Domain, that interests all the cell [51] [52] [53] [54] [55]:

- Current density i_l :

$$i_l = -\sigma_{l,eff} \nabla \Phi_l$$

(3.1)

$\sigma_{l,eff}$ is the effective electrolyte conductivity. It is evaluated using the following formula [56]:

$$\sigma_l = \frac{F^2 C_{H^+} + D_{H^+}}{RT}$$

(3.2)

Where:

- F is the Faraday constant, equal to 96485.3329 C/mol
- R is the ideal gas constant, equal to $8.314 \frac{J}{mol K}$
- C_{H^+} is the concentration of H^+ ions in the membrane
- D_{H^+} is the concentration of H^+ ions due to diffusivity
- T is the operating temperature in K
- Values for C_{H^+} e D_{H^+} are both taken from Ferrero et al [56].

The effective electrolyte conductivity is then corrected using the Bruggeman correlation [57]:

$$\sigma_{l,eff} = \varepsilon_1 \cdot 1,5 \cdot \sigma_l$$

(3. 3)

With ε_1 the Electrolyte volume fraction equal to 0,3.

- Charge balance equation, defined as:

$$\nabla i_l = i_{v,tot}$$

(3. 4)

$i_{v,tot}$ is measured in A/m^3 and is the total of the electrode reactions' volumetric current density contributions in the Gas Diffusion Electrode domains.

In the Membrane and Gas Diffusion Layers domains the sequent charge balance equation is applied:

$$\nabla i_l = 0$$

(3. 5)

The boundary condition in this phase is the insulation, is applied to the walls of the cell or boundaries that do not face a conductor:

$$i_k \cdot n = 0$$

(3. 6)

Where:

- i_k is the current density vector
- $k = 1, s$ is the index for electrolyte and electrode, respectively.

In the Electronic Conducting phase all the electrode domains (anode and cathode) are interested. This time the dependent variable is Φ_s , the electric potential, that is set equal to the Voltage of the cell.

The equations in this phase are referred to [51] [52] [53] [54] [55]:

- Current density i_s :

$$i_s = -\sigma_{s,eff} \nabla \Phi_s$$

(3. 7)

$\sigma_{s,eff}$ is the effective electric conductivity. It is evaluated thanks to the work of Marangio et al [19] solving the equivalent circuit of the cell, as seen in figure 1.3.

- Charge balance equation, defined as:

$$\nabla i_s = i_{v,tot}$$

(3. 8)

Modelling

In the Membrane and Gas Diffusion Layers domains, again, the sequent charge balance equation is applied:

$$\nabla i_s = 0$$

(3. 9)

The boundary conditions of the Electronic Conducting Phase are:

- Insulation, as seen above it applies to every boundary that does not face a conductor.
- Electric ground, used to ground the voltage at the hydrogen side of the cell's current collector, as a reference. The electric potential is set to 0 in this boundary:

$$\Phi_s = 0$$

(3. 10)

- Electric Potential, it sets the electric potential at the cell voltage current collector of the oxygen side of the cell equal to the cell voltage:

$$\Phi_{s,boundary} = V_{cell}$$

(3. 11)

The Electronic Conducting phase has two principal domains:

- Anode domain: In this section is present:
 - Gas phase, where the modelling equations regards the gas phase transport:

$$p_i = x_i p_a$$

(3. 12)

Equation 3.12 states that the pressure of the i element is equal to the molar fraction times the absolute pressure.

$$M_n = \sum_i x_i M_i$$

(3. 13)

Equations 3.13 states that the molecular weight of the mixture is equal to the molecular weight of the i element times the molar fraction.

Gas, in this section and in all the domains are treated as ideal. Therefore, the density of the mixture is evaluated as:

$$\rho = \frac{p_a M_n}{RT}$$

(3. 14)

Equation 3.14 is the ideal gas law.

- Gas Diffusion Electrode. In this section, the $i_{v,tot}$ present in equation 3.8 is evaluated for the anode side. Is equal to:

$$i_{v,tot} = \sum_m i_{v,m} + i_{v,dl}$$

(3. 15)

$i_{v,m}$, the volumetric current in the surface of the electrode, is equal to:

$$i_{v,m} = a_v \cdot i_{loc}$$

(3. 16)

a_v is the Active Specific Surface Area, a geometrical parameter that in the cell used is 10^6 1/m.

i_{loc} is the local current, and it is calculated through the Electrode Kinetics, using the Butler-Volmer equations seen in the Literature Review, equations 1.12 and 1.13.

Below are the Butler-Volmer equations used in the modelling:

$$i_{loc,expr,an} = i_0 \left(\exp\left(\frac{\alpha_{an} F \eta}{RT}\right) - \exp\left(\frac{-\alpha_{cat} F \eta}{RT}\right) \right)$$

(3. 17)

Where:

- i_0 is the exchange current density
- α_{an} is the anode exchange coefficient, as seen in L.R. equal to 2
- F is the Faraday constant
- η is the activation overpotential, it denotes the amount of voltage used to speed up an electrochemical process by activating it, measured in V.
- R is the ideal gas constant
- T is the operating temperature
- α_{cat} is the cathode exchange coefficient, equal to 0,5

In order to have i_{loc} , $i_{loc,expr}$ is corrected by a factor, for both anode and cathode, the limited current density.

The electrolyte content and solution velocity affect the limiting current density of a liquid solution. Concentration polarization occurs in the boundary layer of an ion exchange membrane's substrate surface.

Limiting current density is affected by the solution flow in a desalting cell, the path of ionic transportation in the boundary layer, the distribution of solution flow in desalting cells:

$$i_{lim} = \frac{2FD_w \rho_{an} tr_l}{M_{O_2}}$$

(3. 18)

Where:

- D_w is the diffusion coefficient, taken from the work of Ferrero et al
- ρ_{an} is the anode density
- tr_l in the transport length

Modelling

- M_{O_2} is the molar weight of oxygen

i_{loc} can then be corrected:

$$i_{loc} = \frac{i_{loc,expr}}{1 + \left\| \frac{i_{loc,expr}}{i_{lim}} \right\|}$$

(3. 19)

In Equation 3.17 the activation overvoltage is used. It is equal to:

$$\eta = E_{ct} - E_{eq}$$

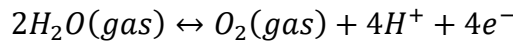
(3. 20)

- E_{ct} is the difference between the Electronic Potential and the Ionic Potential:

$$E_{ct} = \Phi_s - \Phi_l$$

(3. 21)

- E_{eq} is the Equilibrium Potential. It is calculated applying the Nernst equation seen in L.R. (equation 1.4) to the semi reaction (OER), in this case at anode side:



(3. 22)

The Equilibrium Potential of the reaction is:

$$E_{eq,an} = \frac{\Delta g_0(T, p_0)}{z_r F} + \frac{RT}{z_r F} \ln \left(\frac{p_{O_2}^{0,5}}{p_{H_2O}} \right)$$

(3. 23)

Where:

- $\Delta g_0(T, p_0)$ is the Gibbs Free Energy variation at Standard Condition, equal to the difference of Gibbs Free Energy at S.C. of products and reactants:

$$\Delta g_{0,OER} = \Delta g_{0products} - \Delta g_{0reactants}$$

(3. 24)

- p_i are the partial pressures of products (numerator) and reactants (denominator) elevated to their number of moles.
- z_r is the number of electrons exchanged
- F is the Faraday Constant
- R the ideal gas constant
- T is the operating temperature, in K

- Cathode domain. As for the anode one, in this section is present:

Modelling

- Gas phase
- Gas Diffusion Electrode. $i_{v,tot}$ and i_{loc} are this time evaluated for the cathode side. The Butler-Volmer equation changes:

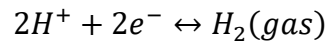
$$i_{loc,expr,cat} = i_0 \left(\exp\left(\frac{\alpha_{cat}F\eta}{RT}\right) - \exp\left(\frac{-\alpha_{an}F\eta}{RT}\right) \right)$$

(3. 25)

Where:

- i_0 is the exchange current density
- α_{an} is the anode exchange coefficient, as seen in L.R. equal to 2
- F is the Faraday constant
- η is the activation overpotential, it denotes the amount of voltage used to speed up an electrochemical process by activating it, measured in V.
- R is the ideal gas constant
- T is the operating temperature
- α_{cat} is the cathode exchange coefficient, equal to 0,5

The Equilibrium Potential this time is calculated applying the Nernst equation to the semi reaction (HER), in this case at cathode side:



(3. 26)

The Equilibrium Potential of the reaction is:

$$E_{eq,an} = \frac{\Delta g_0(T, p_0)}{z_r F} + \frac{RT}{z_r F} \ln(H_2)$$

(3. 27)

3.3.2 Free and Porous Media Flow

In this Physics, Navier-Stokes equations are used in to describe flow in open areas, while the Brinkman equations are used to describe flow in porous regions at the Free and Porous Media Flow Interface.

In both the free flow and porous domains, the identical fields, u , velocity field, and p , pressure field are solved for. This indicates that along the interface between a free flow domain and a porous domain, the pressure in the free fluid and the pressure in the pores are both constant. It also implies that the fluid velocity in free flow and the Darcy velocity in the porous domain must be consistent.

The stress discontinuity at the boundary between a free-flow domain and a porous domain is implied by the continuity in u and p . The difference is the stress absorbed by the stiff porous matrix, which is a result inherent in the Navier-Stokes and Brinkman equations' formulations.

The domain interested are anodic and cathodic ones (both electrode and catalyst layer).

Equations are taken from Le Bars et al [58].

Navier stokes Equation for flow in open areas:

$$\rho(u \cdot \nabla u) = \nabla \cdot [-pI + \mu(\nabla u + (\nabla u)^T)]$$

(3. 28)

Where:

- u is the velocity field vector
- ρ is the density
- p is the reference pressure
- μ is the viscosity
- T the reference temperature

Brinkman equation for flow in porous region:

$$\frac{\rho}{\varepsilon} \left[(u \cdot \nabla) \frac{u}{\varepsilon} \right] = \nabla \cdot \left\{ -pI + \frac{\mu}{\varepsilon} [\nabla u + (\nabla u)^T] - \frac{2\mu}{3\varepsilon} (\nabla u)I \right\} - \left(\frac{\mu}{k} + \frac{Q}{\varepsilon^2} \right) u$$

(3. 29)

Where:

- ε is the porosity
- k is the thermal conductivity
- Q is the mass volumetric source

The equations are solved together using the continuity equation:

$$\rho \nabla \cdot \mathbf{u} = Q$$

(3. 30)

Q is set equal to 0.

Boundary conditions applied in this physic are:

- Wall conditions, in the boundary between anode (cathode) bipolar plates and the electrode. No slip condition is applied: the fluid velocity relative to the wall velocity is zero on a no slip wall. This indicates that $\mathbf{u} = 0$ for a stationary wall.
- Inlet, in the inlet boundary at anode (cathode). The condition applied is the velocity at inlet, equal to:

$$u_{H_2O,anode} = \frac{G_{H_2O,anode}}{\rho_{H_2O}(T)}$$

(3. 31)

Where:

- $G_{H_2O, anode}$ is the flow of water at anode side
- $\rho_{H_2O}(T)$ is the density of water, function of temperature, added in the Material node of the COMSOL model.

At cathode inlet, the equation is the same with the flow of water relative to the cathode side, which is set to 0 in the closed cathode configuration.

- Outlet, in the inlet boundary at anode (cathode). This condition is applied to domain borders if there is a net outflow. The boundary conditions applied is for pressure (from the Navier Stokes equation):

$$(-p_{out} + K)n = -p_o$$

With p_o equal to the anode (cathode) operating pressure. Backflow is not considered in this boundary.

- Electrode-Electrolyte Interface Coupling, in the boundary between anode (cathode) and the electrolyte membrane. Is used in order construct a combined wall and inflow/outflow boundary condition in an Electrochemistry interface depending on current densities of one or more Electrode Reaction nodes. According to Faraday's rule, the flow is proportional to the reacting species' molar mass (kg/mol), current densities, and stoichiometric coefficients as determined by summation over the Reaction Coefficient subnodes:

$$-n \cdot \mathbf{j}u = \sum_{m,i} R_{i,m} M_i$$

(3. 32)

Where:

Modelling

- n is the number of electrons of the coupled reaction, that is the Butler-Volmer equation for the local current density, for anode equation 3.19, for cathode 3.25 (with the limiting current correction).
 - j is the current density
 - R are the reaction coefficients of the coupled reaction. (3.19 anode, 3.25 cathode)
 - M are the molar masses of the elements of the coupled reaction. For the anode/membrane boundary, they are molar mass of oxygen and water, for the cathode/membrane boundary, is the molar mass of hydrogen.
- To evaluate the Reaction coefficient from the coupled reaction, the following formula is used:

$$R_i = \frac{\nu_i i_{loc}}{nF}$$

(3.33)

Where:

- ν_i are the stoichiometric coefficients
- i_{loc} is the local current density
- F is the Faraday constant

3.3.3 Transported of Diluted Species

Transport of Diluted Species interface is used to compute the concentration field of a dilute solute in a solvent. This interface manages the transport and interactions of species dissolved in a gas, liquid, or solid. Diffusion, as defined by Fick's law, convection when related to a flow field, and migration when coupled to an electric field are all driving factors for transport.

The molar concentration, c , is the dependent variable. Multiple species transport is modelled using the physics interface, which solves for each species' molar concentration, c_i . Three distinct domains are considered: anode, cathode and membrane.

Fick's Law:

$$\nabla \cdot J_i + u \cdot \nabla c_i = R_i$$

(3.34)

Where:

- J_i is Diffusive Flux vector, measured in $\left[\frac{\text{mol}}{\text{m}^2\text{s}}\right]$. It is evaluated as:

$$J_i = -D_i \nabla c_i$$

(3.35)

With:

- D_i is the Diffusion Coefficient of the i specie. It is calculated as a binary diffusion coefficient for mixtures:

$$D_i = \frac{a}{p} \left(\frac{T}{\sqrt{T_{c,a} \cdot T_{c,b}}} \right)^b \cdot (p_{c,a} \cdot p_{c,b})^{\frac{1}{3}} \cdot (T_{c,a} \cdot T_{c,b})^{\frac{5}{12}} \cdot \left(\frac{1}{M_a} + \frac{1}{M_b} \right)^{\frac{1}{2}}$$

(3.36)

In which:

- a and b are empirical coefficient for the species under consideration
- p is the reference pressure
- T is the reference temperature
- $p_{c,i}$ is the critical pressure
- $T_{c,i}$ is the critical temperature
- M is the molar weight of the species

The mixtures considered are O_2 in H_2O for the anode side and H_2 in H_2O for the cathode one.

- ∇c_i is the Molar concentration gradient of the i specie. Concentration is measured in $\left[\frac{\text{mol}}{\text{m}^3}\right]$ and the species considered are in the anode domain oxygen and water, in the membrane domain only water and in the cathode domain hydrogen and water
- u is the velocity of i specie

Modelling

- R_i is the Reaction rate of the i specie.

The boundary conditions for this physics are different for the anode/cathode domain and for the membrane one.

In the anode (cathode) domain they are:

- No Flux condition, applied in the boundary between electrode and bipolar plate. The condition applied is that there is no mass flux, since is a solid wall with no surface interactions. The condition that each species is subjected to corresponds to:

$$-n \cdot (J_i + uc_i) = 0$$

(3. 37)

Where:

- n is the outward pointing normal of the boundary
- J_i is Diffusive Flux vector of the i specie
- u is the velocity of i specie
- c_i is the Molar concentration of the i specie
- Electrode-Electrolyte Interface Coupling, in the boundary between anode (cathode) and the electrolyte membrane, as for the Free and Porous Media Flow physic boundary condition:

$$-n \cdot J_i u = \sum_{m,i} R_{i,m} M_i$$

(3. 38)

Instead of the current density of equation 3.32, the Diffusive Vector is present. Reaction Coefficients are taken from the same equation from anode and cathode.

- Inflow, at the inlet of anode (cathode). The inlet concentration, in mol/m³, is specified of oxygen and anodic water for anode and of hydrogen and cathodic water for the cathode.
- Outflow, at the outlet boundaries, to transfer organisms out of the model domain through fluid motion or an electric field (in the case of ions). The dominant transport processes across the boundary are convection and migration (in an electric field), and hence diffusive transport may be neglected, that is:

$$n \cdot D_i \nabla c_i = 0$$

(3. 39)

In the membrane, the boundary conditions are:

- No Flux condition, applied in the upper and lower layer of the membrane (the boundaries not in contact with the electrodes), same equations as for 3.37.
- Concentration condition, which adds a boundary condition for the species concentrations. In the Electrolyte-Anode boundary, the concentration specified is the anodic water, in the Electrolyte-Cathode boundary, is the cathodic one.

References for the modelling equations and boundary conditions in this physic: [60], [61], [62], [63],[64], [65], [66].

3.3.4 Darcy's Law

Because the pore walls obstruct momentum transmission to the fluid beyond the individual pores, the global transport of momentum by shear stresses in the fluid in a porous media is frequently insignificant. In most cases, a precise description down to the resolution of each pore is impractical. A typical alternate strategy is to combine the porous and fluid media into a single medium. Darcy's law, in combination with the pore fluid (or gas) continuity equation and equation of state, provides a comprehensive mathematical model suited for a broad range of applications involving porous medium flows in which the pressure gradient is the primary driving factor.

Darcy's law defines fluid flow across porous media's interstices. Flow velocities in porous media are extremely low because the fluid loses a lot of energy due to frictional resistance inside the pores. The Darcy's Law interface is used to solve small-scale chemical engineering problems as well as large-scale geophysical or hydrological problems like water flowing in an aquifer or stream bank, oil migrating to a well, and even magma rising through the ground to a volcano's chamber

Darcy's law explains flow in porous material that is caused by pressure gradients in the hydraulic potential field. For many applications, equivalent fluid or head heights are used to describe the complete hydraulic potential, pressure, and gravity components. Because units of length make it easy to compare to a variety of physical facts, dividing potential by fluid weight helps simplify modelling. The physics interface also allows the specification of boundary conditions as well as the assessment of results using hydraulic and pressure heads.

Pressure is always the dependant variable in the physics interaction.

The domain where this physics is applied is the membrane domain.

According to Darcy's law, the velocity field is governed by the pressure gradient, fluid viscosity, and porous media structure:

$$u = -\frac{k}{\mu} \nabla p$$

(3. 40)

Where:

- u is the Darcy's velocity or Specific Discharge Vector [m/s]
- k is the permeability of the porous medium [m^2]
- μ is the dynamic viscosity of the fluid [$Pa \cdot s$]
- p is the pore pressure [Pa]

The Darcy's Law physic combine equation 3.40 with the continuity equation, to obtain:

$$\frac{\partial}{\partial t}(\rho \varepsilon_p) + \nabla \cdot (\rho u) = Q_m$$

(3. 41)

Where:

- ρ is the density of the fluid [kg/m^3]

Modelling

- ε_p is the porosity [dimensionless]. The percentage of the control volume filled by pores is known as porosity. As a result, porosity may range from zero for pure solid areas to unity for free-flowing domains.
- Q_m is the mass source term [kg/m^3s]

Boundary conditions for this interface are:

- No flow conditions, applied to the upper boundary of the electrolyte. It states that there is no flow over impermeable limits. This is the mathematical formula:

$$n \cdot \rho \frac{k}{\mu} (\nabla p + \rho g \nabla D) = 0$$

(3. 42)

Where:

- n is the outward pointing normal of the boundary
 - D is the elevation head [m], equal to 0 in this electrochemical application
-
- Pressure conditions, where the pressure values for the boundaries with anode and cathode is specified.

References for this physic are found in: [67] [68] [69] [70] [71] [72].

3.3.5 Heat Transfer in Porous Media

The Heat Transfer in Porous Medium physic is used to simulate heat transfer in porous media via conduction, convection, and radiation. On all domains, the Porous Medium model is enabled by default. Other domain types, such as a solid domain, can also be included using the same capability.

In porous media domains, the temperature equation relates to the convection-diffusion equation, with thermodynamic properties averaging models to account for both solid matrix and fluid characteristics. When the temperatures inside the porous matrix and the fluid are in balance, this equation holds true.

The mixture rule on energies found in solid and fluid heat transfer equations is used to create the heat transfer equation for porous media. Equation 3.43 simplifies for undeformed immobile solids to:

$$\rho_s C_{p,s} \frac{\partial T_s}{\partial t} + \nabla \cdot q_s = Q_s$$

(3.43)

Where:

- ρ_s is the density of the solid [kg/m^3]
- $C_{p,s}$ is the heat capacity at constant pressure of the solid [$J/kg \cdot K$].
- T_s is the temperature of the solid [K]
- q_s is the conductive heat flux [W/m^2]
- Q_s is the heat source [W/m^3]

For a fluid domain where pressure work and viscous dissipation are neglected, it becomes:

$$\rho_f C_{p,f} \frac{\partial T_f}{\partial t} + \rho_f C_{p,f} u_f \cdot \nabla T_f + \nabla \cdot q_f = Q_f$$

Where:

- u_f is the velocity of the fluid.

(3.44)

The mixture rule is applied by multiplying the first equation by the solid volume fraction, s , and the second equation by the porosity, p , and then adding the two equations together.

In both the fluid and solid phases, the local thermal equilibrium theory presupposes temperature equality:

$$T_f = T_s = T$$

(3.45)

In a porous matrix, possibly consisting of several solids, and filled with a mobile fluid, and one or more immobile fluids, which is the case of anode and cathode, the equation becomes:

Modelling

$$\rho_p C_p u_f \cdot \nabla T_p + \nabla \cdot q_p = Q_p$$

(3. 46)

The q_p is the conductive heat flux for porous media, and is obtained:

$$q = -d_z k_{eff} \nabla T$$

(3. 47)

k_{eff} is the effective thermal conductivity [$\frac{W}{m} \cdot k$] defined by an averaging model to take into account both solid matrix and fluid properties:

$$k_{eff} = \theta_p k_p + (1 - \theta_p)k + k_{disp}$$

(3. 48)

Where:

- θ_p is the volume fraction of the solid material
- k_p is the thermal conductivity of the porous medium
- k is the thermal conductivity of the fluid referred to the fluid volume fraction, equal to $1-\theta_p$
- k_{disp} is the thermal conductivity of the dispersed fluid

The heat source Q_p in the model are generated by three contributors:

1. Heat of activation, generated by the activation overvoltage:

$$Q_{act,an} = \eta_{act,an} \cdot i_{loc,an}$$

(3. 49)

For the anode side

$$Q_{act,cat} = \eta_{act,cat} \cdot i_{loc,cat}$$

(3. 50)

For the cathode side

Where:

- η_{act} is the activation overvoltage
- i_{loc} is the local current density

2. Heat of irreversibility during the redox reactions:

Modelling

$$Q_{irr,an} = \frac{T\Delta S_{an}}{2F} \cdot i_{loc,an}$$

(3. 51)

For the anode side

$$Q_{irr,cat} = \frac{T\Delta S_{cat}}{2F} \cdot i_{loc,cat}$$

(3. 52)

Where:

- ΔS is the entropy variation in the redox reaction
- T is the reference temperature
- F is the Faraday constant

1. Heat due to Joule effect:

$$Q_{joule} = -(i_s \nabla \cdot \Phi_s + i_l \nabla \cdot \Phi_l)$$

(3. 53)

Where:

- i_s is the ionic current density
- Φ_s is the electronic potential
- i_l is the electric current density
- Φ_l is the electronic potential

Boundary conditions:

- Boundary heat source, which prescribes that the temperature field is continuous across the boundary. The boundary selection is the membrane interface with anode (cathode):

$$-n \cdot q = dzQ$$

(3. 54)

Where:

- n is the outward pointing normal of the boundary
- q is the conductive heat flux
- Q is the heat source.

References for this physics are in [73] [74] [75] [76].

3.3.6 Bubbly Flow, $k - \omega$

Modelling

The Bubbly Flow k - ω interface it is used to describe the flow of liquids with distributed bubbles at high Reynolds numbers, it is used instead of the Free and Porous Media physic, and it take into account the effects of the formation of bubbles in the anodic compartments.

The bubbles are expected to take up a modest volume proportion and to always move at their terminal velocity. It is thus possible to solve only one set of Navier-Stokes equations for the liquid phase and use a slip model to direct the bubble velocity. A mixture-averaged continuity equation is used to compute the pressure distribution.

By calculating a transport equation for the effective gas density, the volume fraction of bubbles is monitored. The Wilcox revised two-equation k - ω model with realizability limitations and bubble-induced turbulence generation is used to model turbulence effects. The k - ω model is a low-Reynolds number model, meaning it can resolve the flow all the way to the wall [77].

The domain interested in this physics is the anode one, since the formation of bubbles is related to the concentration of oxygen.

The Turbulent Bubbly Flow k - ω equations, are:

$$\rho_l(u_l \cdot \nabla)u_l = \nabla \cdot [-pI + K] + \Phi_l \rho_l g + F \quad (3.55)$$

$$\rho_l \nabla \cdot u_l = 0 \quad (3.56)$$

$$K = (\mu_1 + \mu_t)(\nabla u + (\nabla u)^T) \quad (3.57)$$

$$\nabla \cdot N \rho_g \Phi_g = -m_{gl} \quad (3.58)$$

$$N \rho_g \Phi_g = \rho_g \Phi_g u_g \quad (3.59)$$

$$u_g = u + u_{slip} - \frac{D_{gc}}{\Phi_g} \nabla \Phi_g \quad (3.60)$$

$$D_{gc} = \frac{\mu_t}{\rho_l \sigma_t} \quad (3.61)$$

$$\rho(u \cdot \nabla)k = \nabla \cdot [(\mu_l + \mu_t \sigma_k) \nabla k] + P_k - \beta_0 \rho_l \omega k \quad (3.62)$$

$$\rho(u \cdot \nabla)\omega = \nabla \cdot [(\mu_l + \mu_t \sigma_\omega) \nabla \omega] + \alpha \frac{\omega}{k} P_k - \beta_0 \rho_l \omega^2 + \alpha_k S_k \frac{\omega}{k} \quad (3.63)$$

Modelling

$$\mu_t = \rho_l \frac{k}{\omega}$$

(3. 64)

$$s_k = -c_k \Phi_g \nabla p u_{slip}$$

(3. 65)

$$P_k = \mu_t [\nabla u (\nabla u + (\nabla u)^T)]$$

(3. 66)

Where:

- ρ_l is the liquid-phase density
- u_l is the liquid-phase velocity
- p is the pressure
- Φ_l is the volume fraction of the liquid phase
- g is the gravity acceleration
- k is the turbulent kinetic energy
- μ_t is the eddy viscosity
- ρ_g is the gas-phase density
- Φ_g is the gas phase volume fraction
- u_g is the gas-phase velocity
- u_{slip} is the slip velocity. For the evaluation, is assumed that the pressure forces on a bubble are balanced by the drag force.
- The Turbulence model parameters for the RANS model are:
 - $\alpha = \frac{13}{25}$
 - $\sigma_k = \frac{1}{2}$
 - $\sigma_\omega = \frac{1}{2}$
 - $\beta_0 = \frac{9}{125}$
 - $k_v = 0.41$
 - $B = 5.2$
 - $\sigma_t = 1$
 - $C_k = 0.505$
 - $\alpha_\omega = 0.46$

The formation of bubbles attached to the electrode is the reason of an additional overvoltage, modelled in the following equation by Amin Nouri-Khourasani et al [78]:

$$\eta_{bubbly} = \frac{-RT_{an} \log(1 - \Phi_g)}{\alpha_{an} F}$$

(3. 67)

Modelling

Where:

- R is the ideal gas constant
- T_{an} is the operative temperature at anode side
- Φ_g is the electrolyte bubble fraction
- α_{an} is the anodic transfer coefficient
- F is the Faraday constant

Boundary conditions:

- Wall, with no slip for the liquid phase and no gas flux for the gas phase, in the interface between anode and anodic back plate.
- Wall in the anode/electrolyte interface, where the gas flux is set equal to:

$$N_{\rho_g \Phi_g} = \frac{i_{loc,anode} M_{O_2} F}{4}$$

(3. 68)

With:

- $i_{loc,anode}$ the local current, from the ButlereVolmere equations
- M_{O_2} the molar weight of oxygen
- F the Faraday constant

The gas mass flux us measured in $[\frac{kg}{m^2 \cdot s}]$

Chapter 4

Results

In this chapter the results obtained with the Comsol models described in chapter 3 are obtained.

4.1 Validation of models

To proceed with the submission of the results, first the veracity of the models must be proven.

As announced in the experimental part, the experimental polarization curves and the curves obtained with the models will be compared in order to find a match.

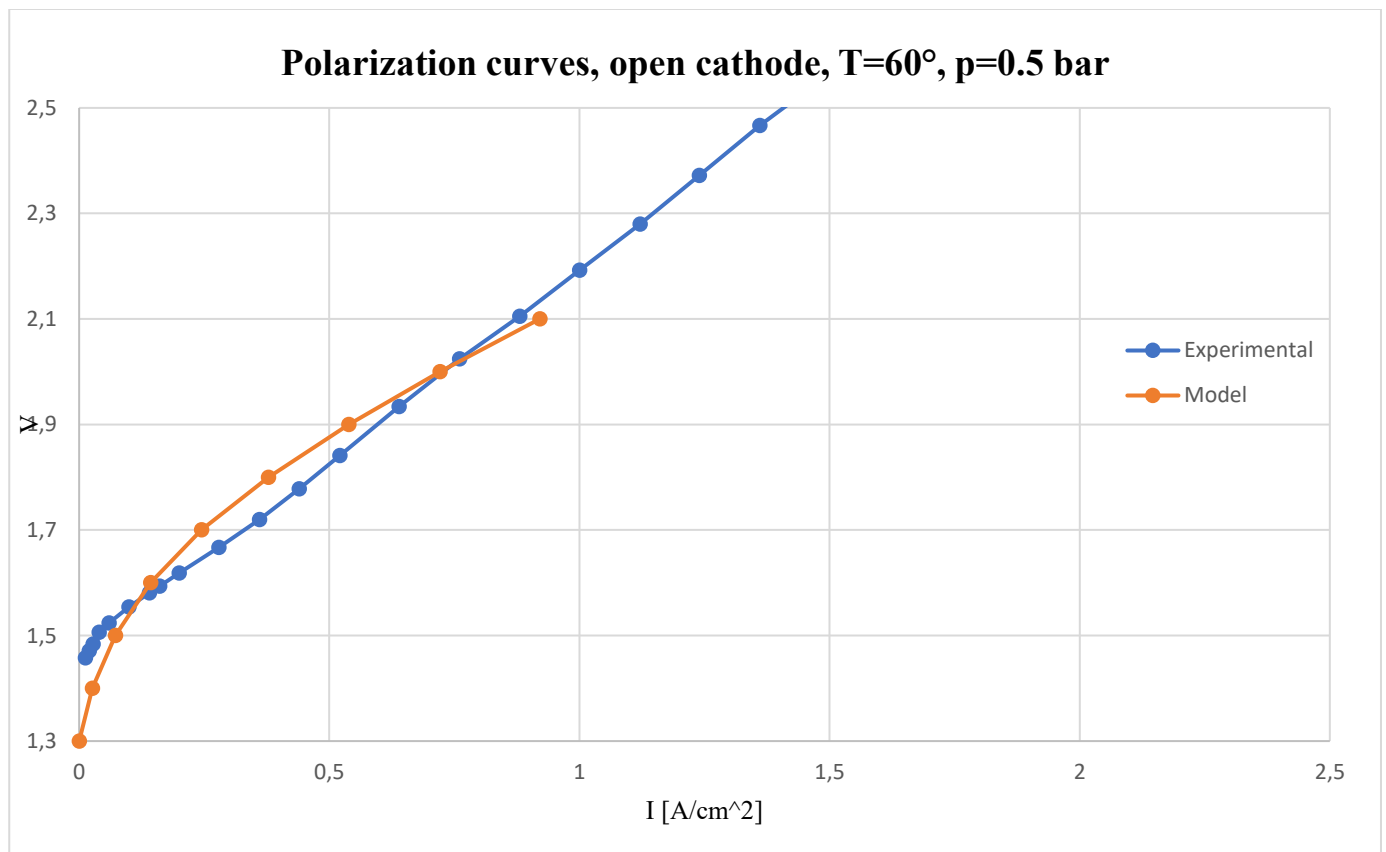


Figure 4. 1 Polarization curves, open cathode, $T=60^\circ$, $p=0.5$ bar

Results

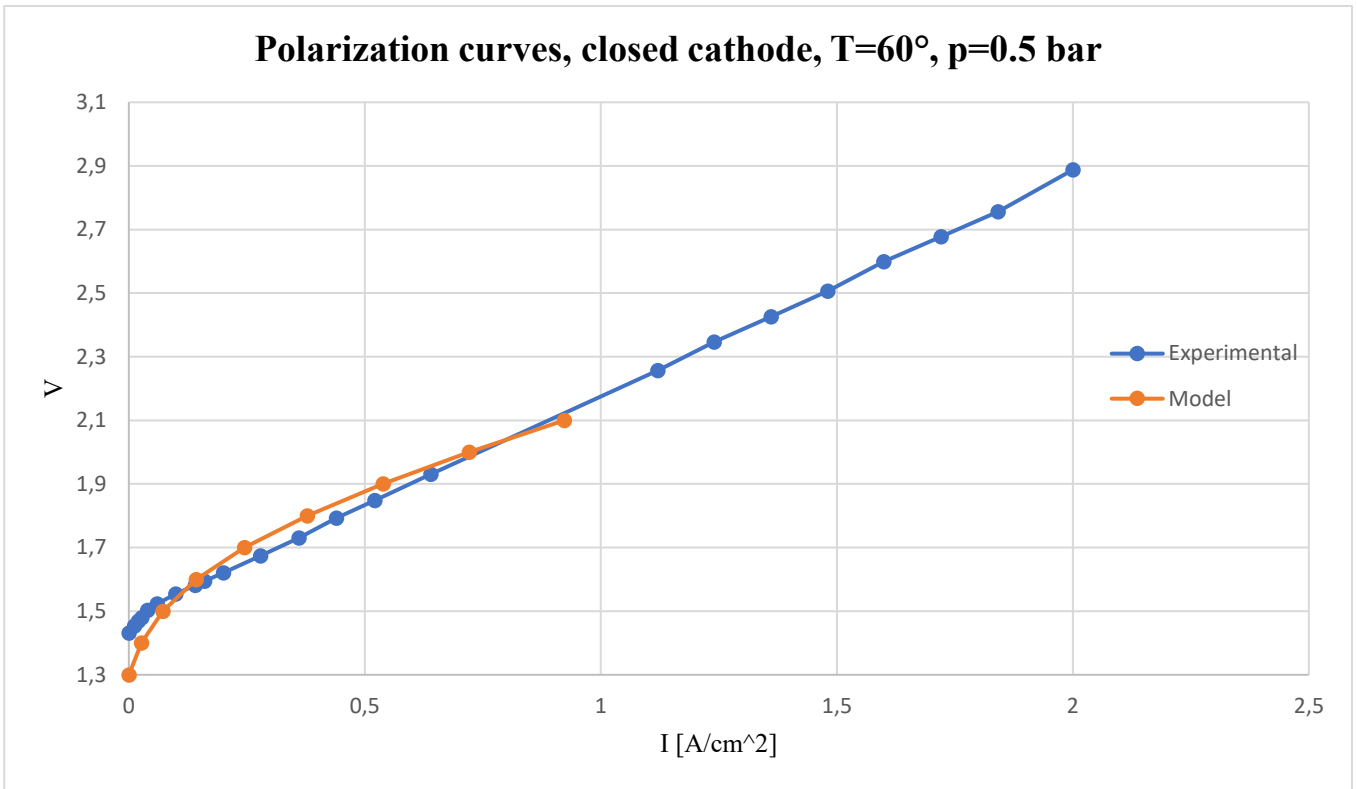


Figure 4. 2 Polarization curves, closed cathode, T=60°, p=0.5 bar

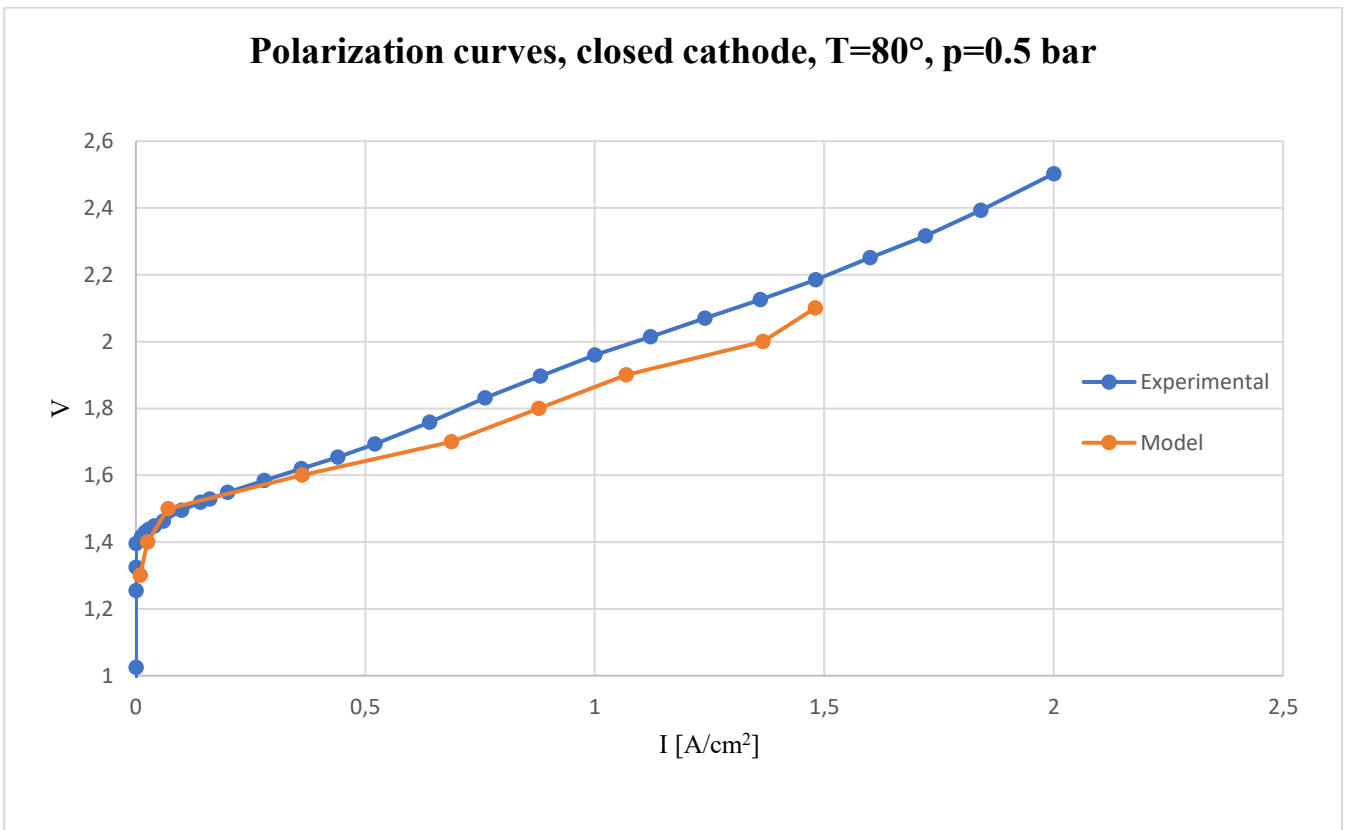


Figure 4. 3 Polarization curves, closed cathode, T=80°, p=0.5 bar

Results

From figure 4.1, 4.2, 4.3 it can be seen that the parameters and model equations illustrated in the previous chapter accurately reflect the experimental reality, as a consequence results can be shown. The validation of the models is related to the 2D models in open and closed cathode.

Simulations performed are for:

- 2D Single-phase Laminar flow Model
- 2D Multi-phase Turbulent Flow Model
- 3D Single Phase Laminar Flow Model
- 3D Single Phase Turbulent Flow Model
- 3D Single Phase Laminar Flow Model Close Cathode configuration

The operating conditions chosen for the simulations were the same as for the validation of models, so:

- $T = 60^\circ \text{C}$
- $p = 0.5 \text{ bar}$ (relative pressure)
- Voltage sweep: increase from OCV to 2.1 V

4.2 2D Single-phase Laminar flow model

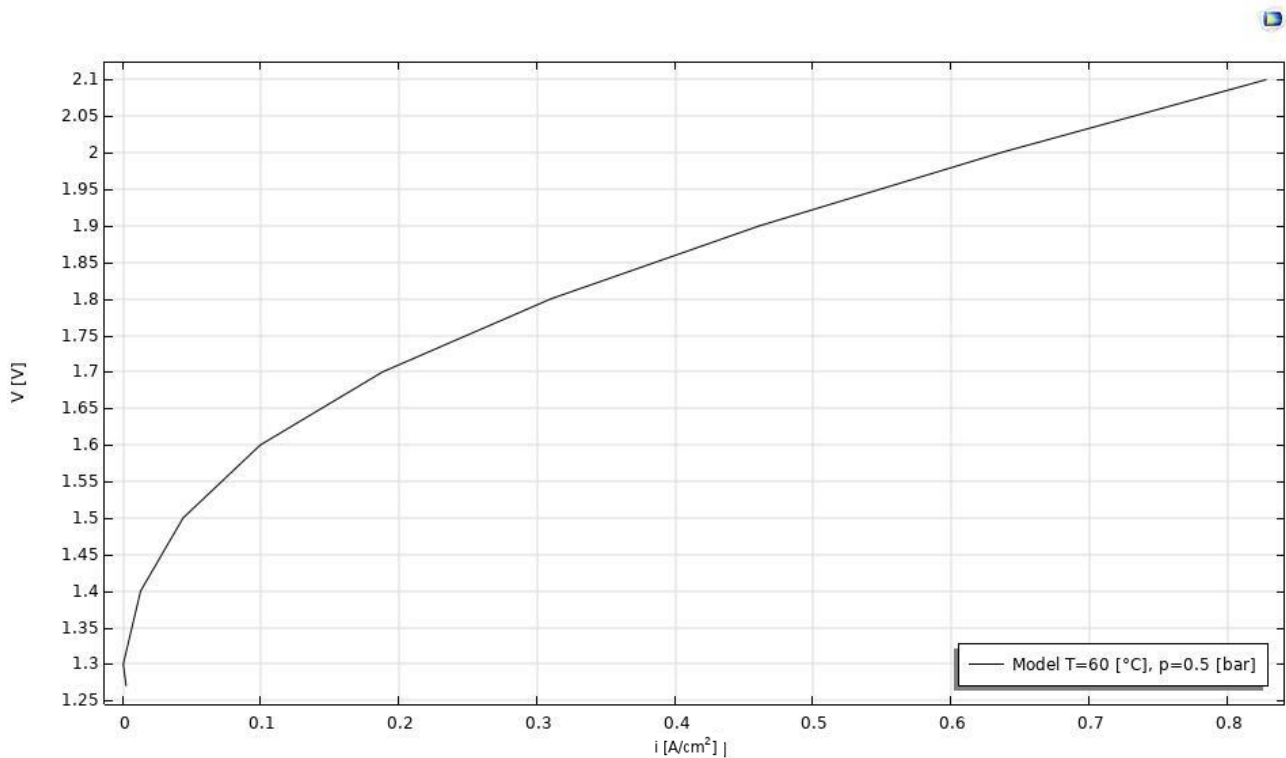


Figure 4. 4 Polarization curve, 2D Laminar Flow

Results

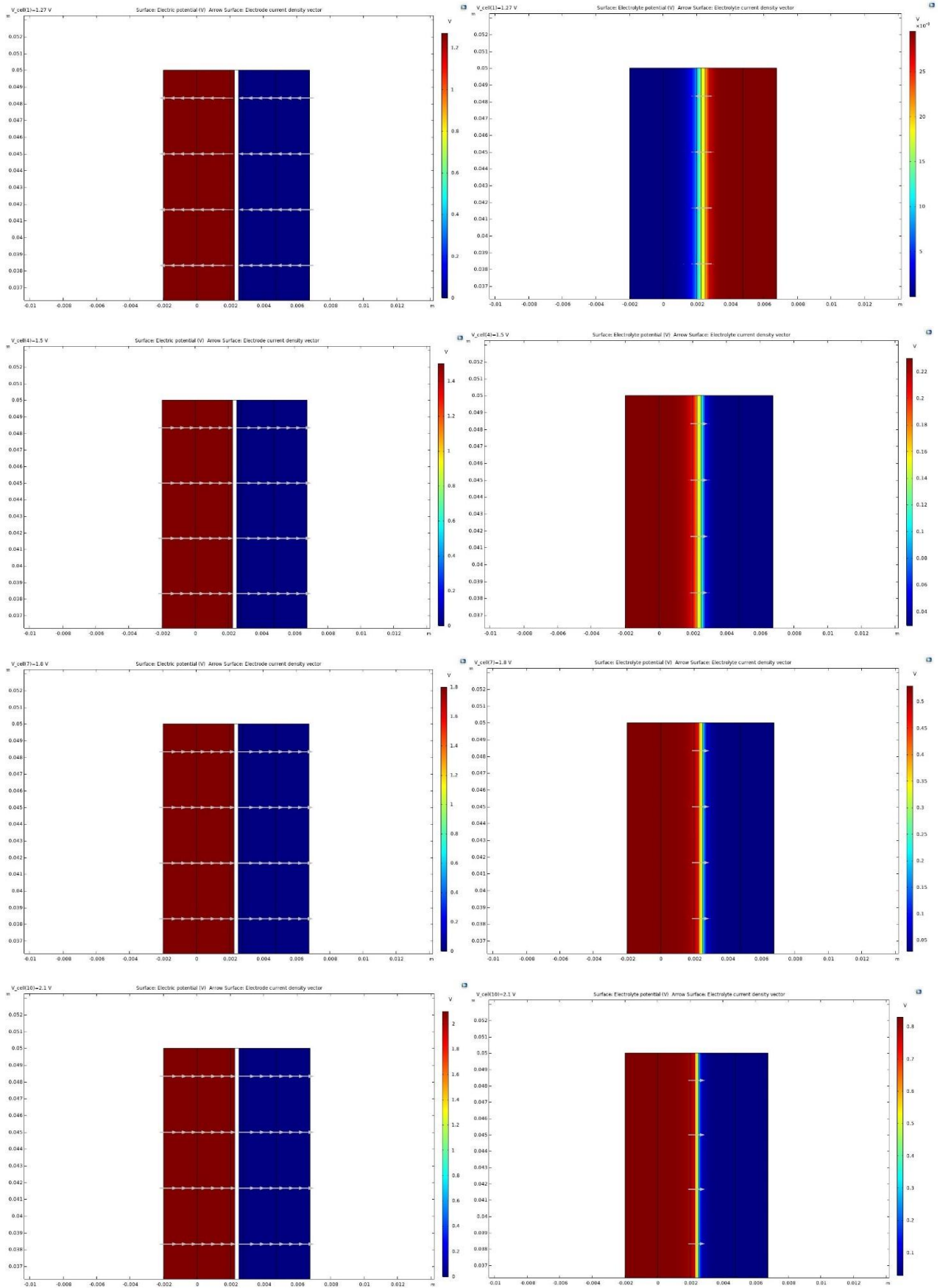


Figure 4. 5 Electric Potential at anode and cathode (left) and Electrolyte Potential (right) for different voltage values, from top to bottom respectively: 1,27-1,5-1,8-2,1 V

Results

From Figure 4.5 it can be seen that the electrode voltage remains constant in both x and y directions throughout the electrodes; however, the electrolyte voltage distributions vary along the x-axis. The fact that it is reversed at open circuit voltage owing to Nernstian physics is one of the most significant findings.

The electric field Vector at the Electrolyte changes direction and aligns with the electric field induced by the external bias when the applied voltage across the terminals of the cell rises in relation to the OCV value, it is shown better in figure 4.6 below where a close-up of the electrolyte at maximum voltage, 2.1, is presented.

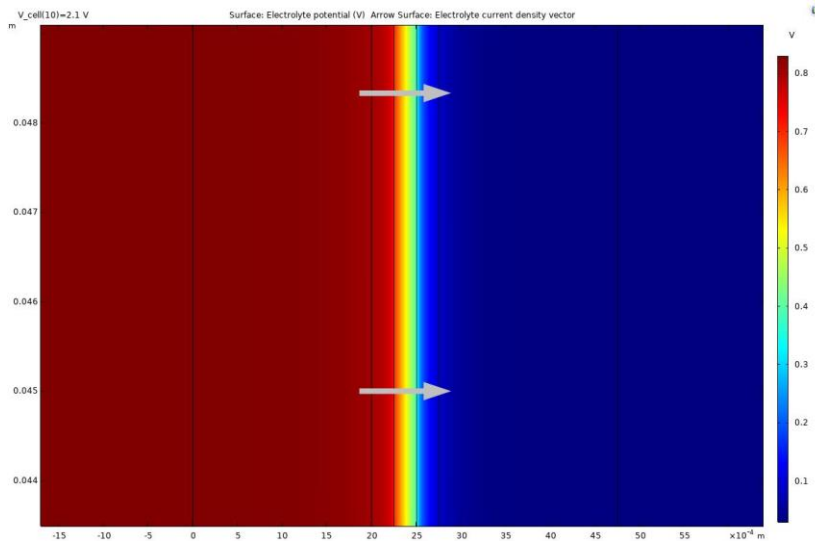


Figure 4.6 Electrolyte field vector, with arrow that indicates the external bias

In Figure 4.7 is reported the relative humidity. The current–voltage behaviour was greatly influenced by the relative humidity of the input carrier gas, with decreased electrolysis current density attributable to dehydration of the PEM at lower humidity levels.

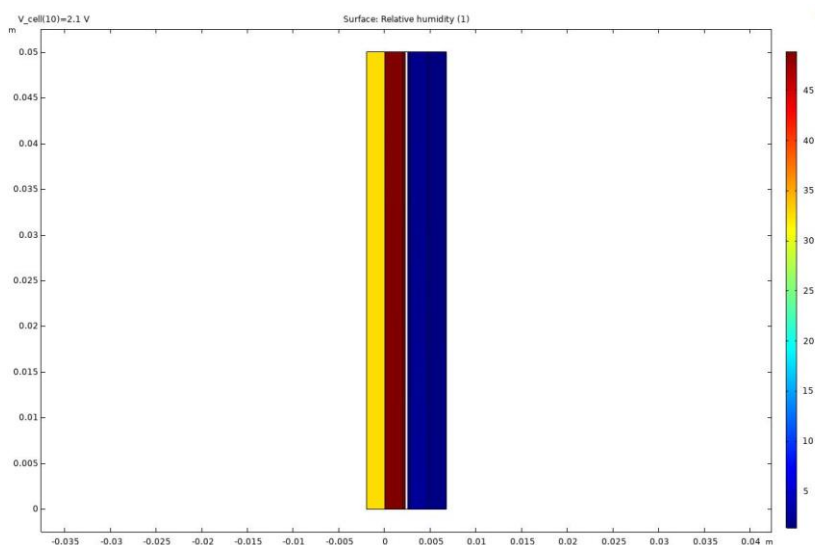


Figure 4.7 Relative Humidity

Same trend as for potential can be seen for current densities, at membrane and electrodes, as shown below in Figure 4.8.

Results

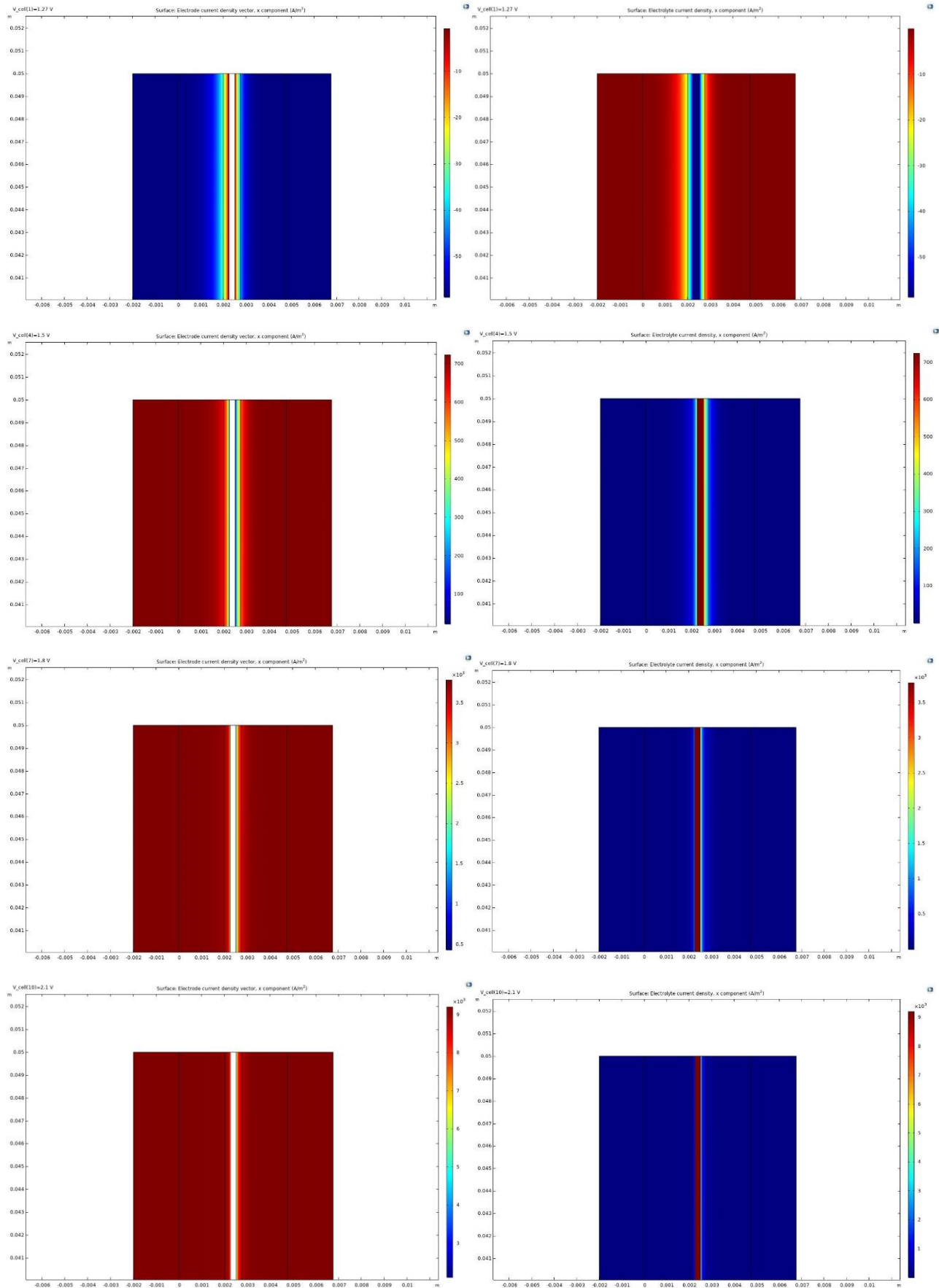


Figure 4.8 Electrode Current Density [A/cm^2] at anode and cathode (left) and Electrolyte Current Density at membrane (right) for different voltage values, from top to bottom respectively: 1,27-1,5-1,8-2,1 V

Results

Concentration of oxygen does not vary with the various voltages applied, apart at the outlet, because the pressure is kept constant. The higher concentration is present at the outlet of the anode, figure 4.10.

Is interesting however the linear concentration of oxygen and hydrogen along anode/electrolyte interface and the cathode/electrolyte interface to better understand the two distributions (figure 4.11).

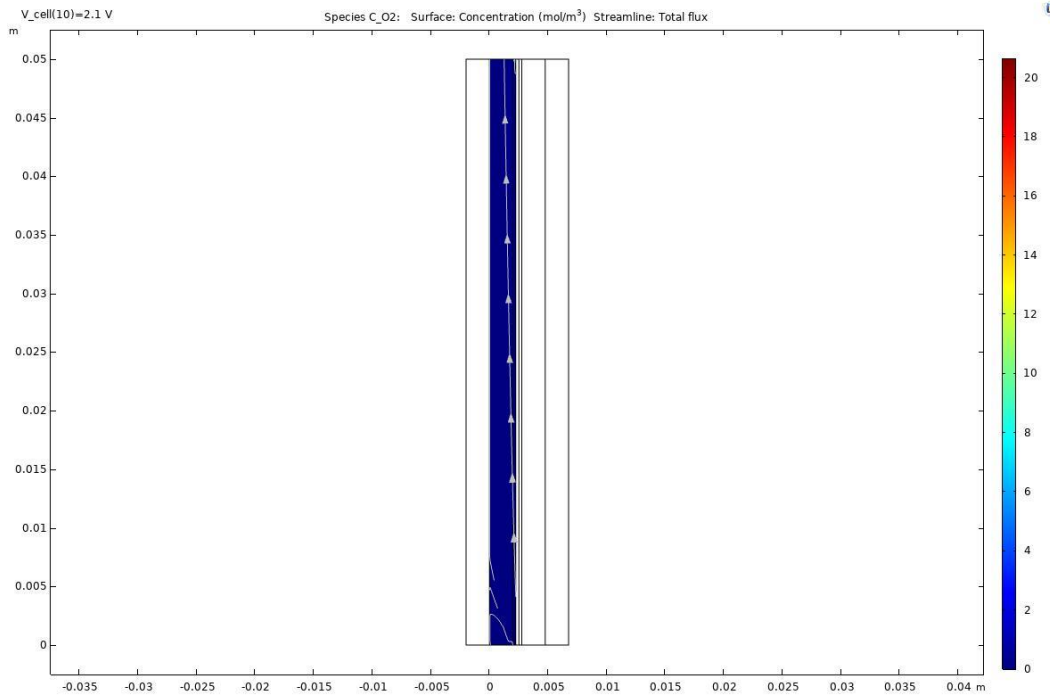


Figure 4.9 Oxygen concentration at anode, $V = 2,1$

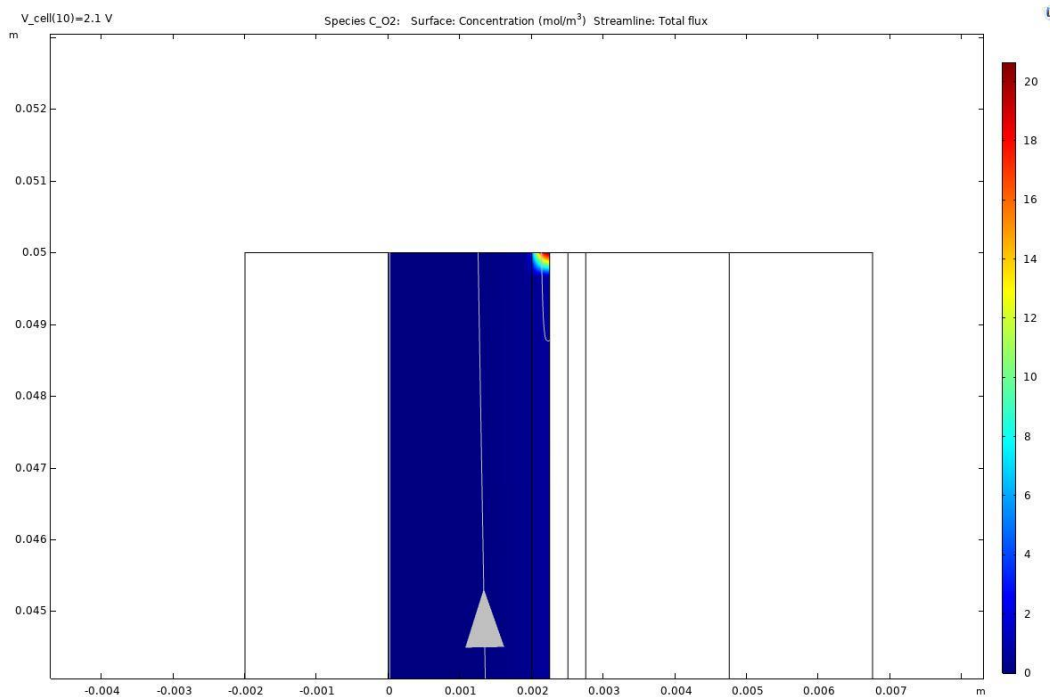


Figure 4.10 Oxygen concentration at anode, $V = 2,1$, outlet closeup

Results

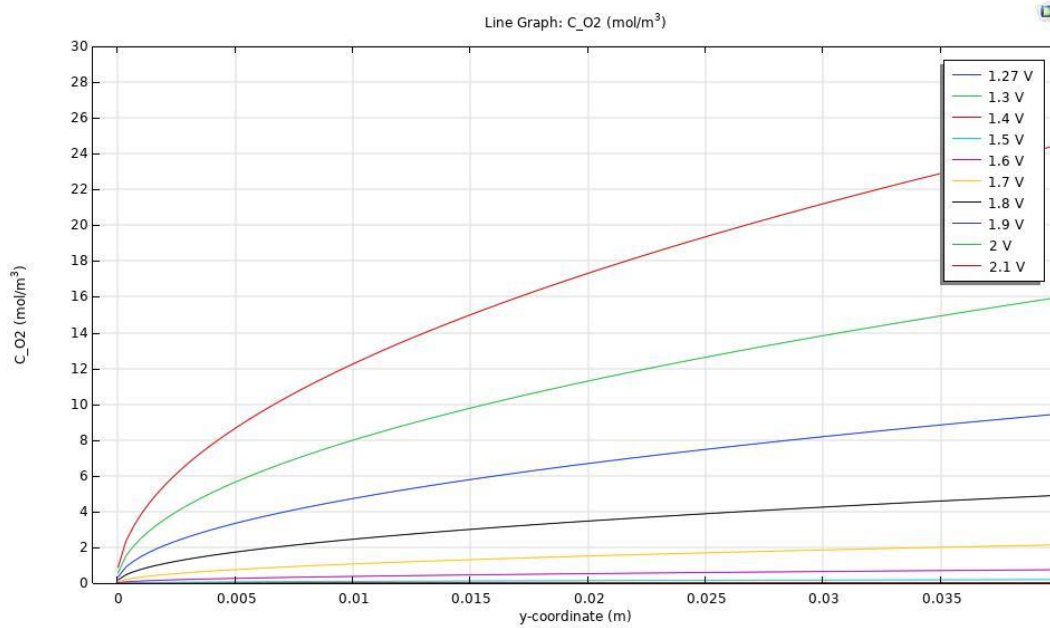


Figure 4.11 Oxygen Concentration at anode/membrane surface

The local current density in the porous anode, the stoichiometric coefficient, and the channel height all have a major influence on the oxygen content. As can be observed in figure 4.11, the molar concentration of O_2 increases as the channel height rises.

The more the applied voltage as well as the height, the greater the concentration rise.

The rise is attributable to an increase in the local current at the interface, and the same trend is shown for the hydrogen distribution.

Results

For what regards the hydrogen distribution, there is a much more homogenous concentration in the cathodic channels and is dependent on the voltage applied:

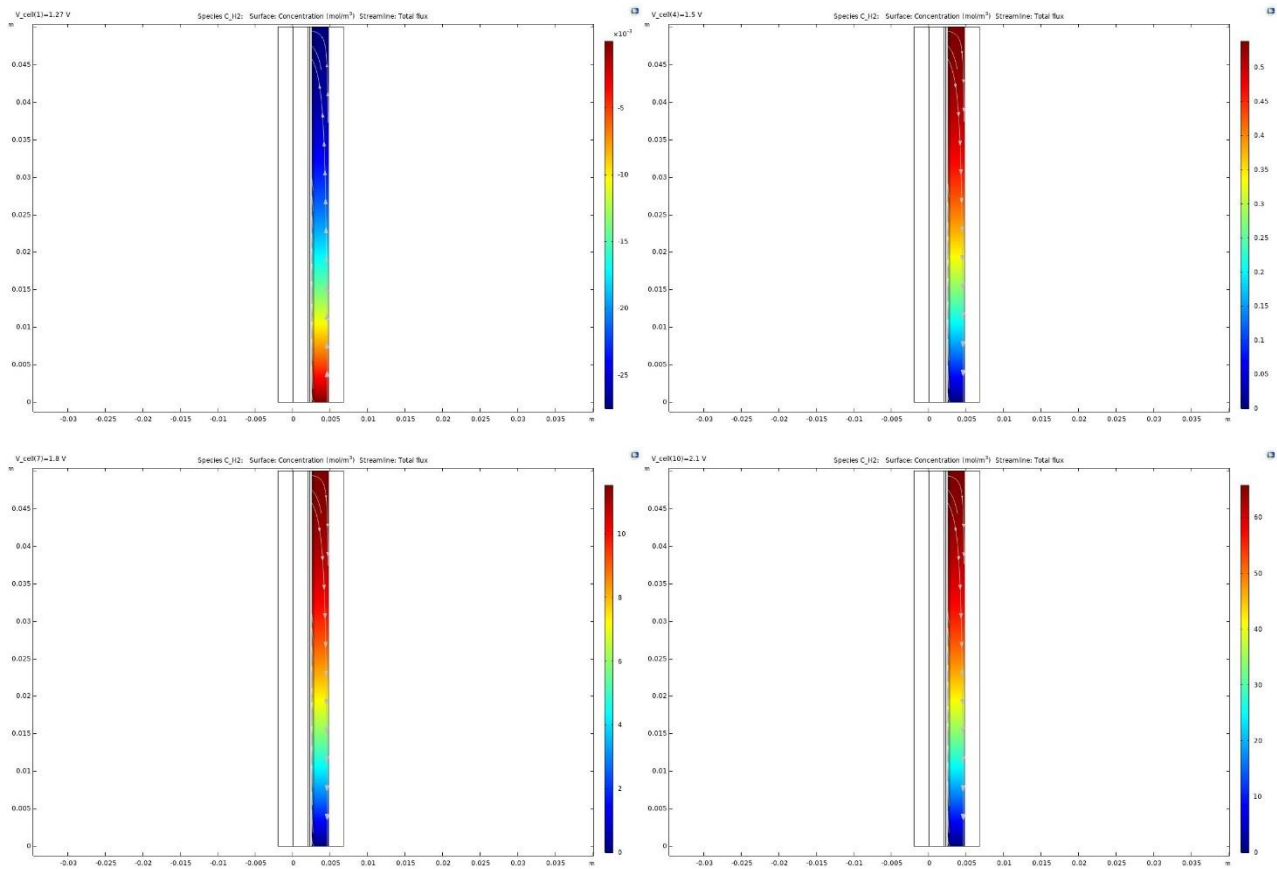


Figure 4.12 Hydrogen distribution with different input voltages [up left 1,27-up right 1,5-bottom left 1,8-bottom right 2,1]

As for the oxygen distribution, the hydrogen one is shown along the cathode/membrane interface:

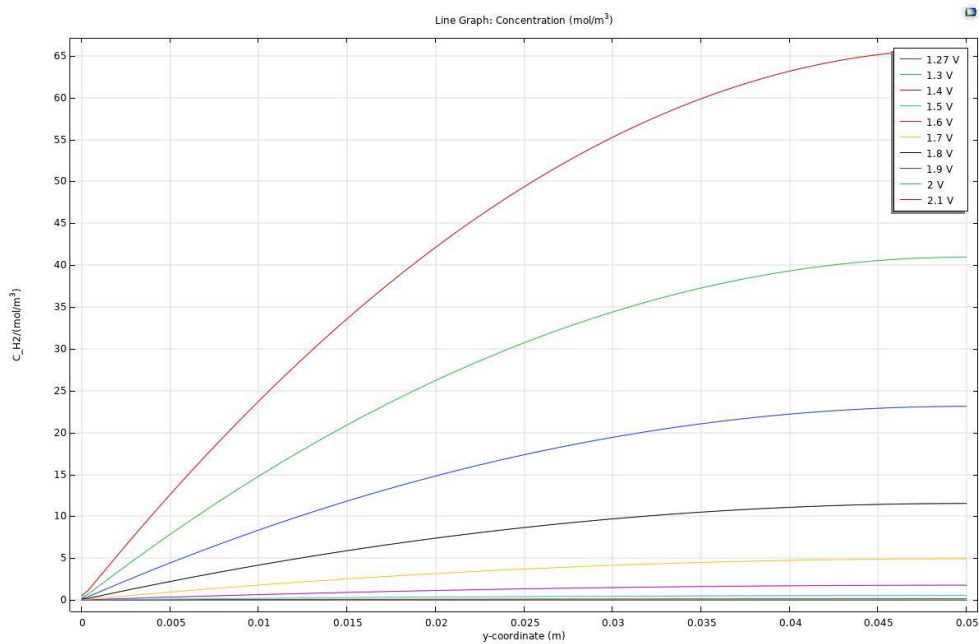


Figure 4.13 Hydrogen Concentration at the cathode/membrane interface

Results

Again, as for the anode/membrane interface, the hydrogen rises with height and voltage, as a direct consequence of the rising of the local current.

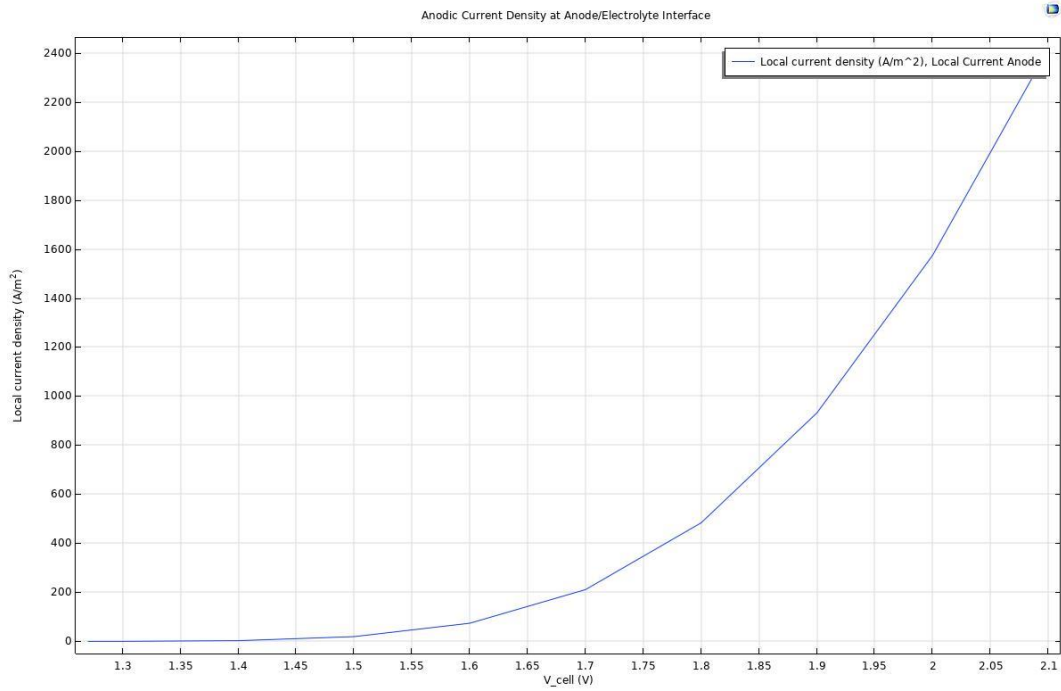


Figure 4.14 Local current density at Anode/Membrane interface

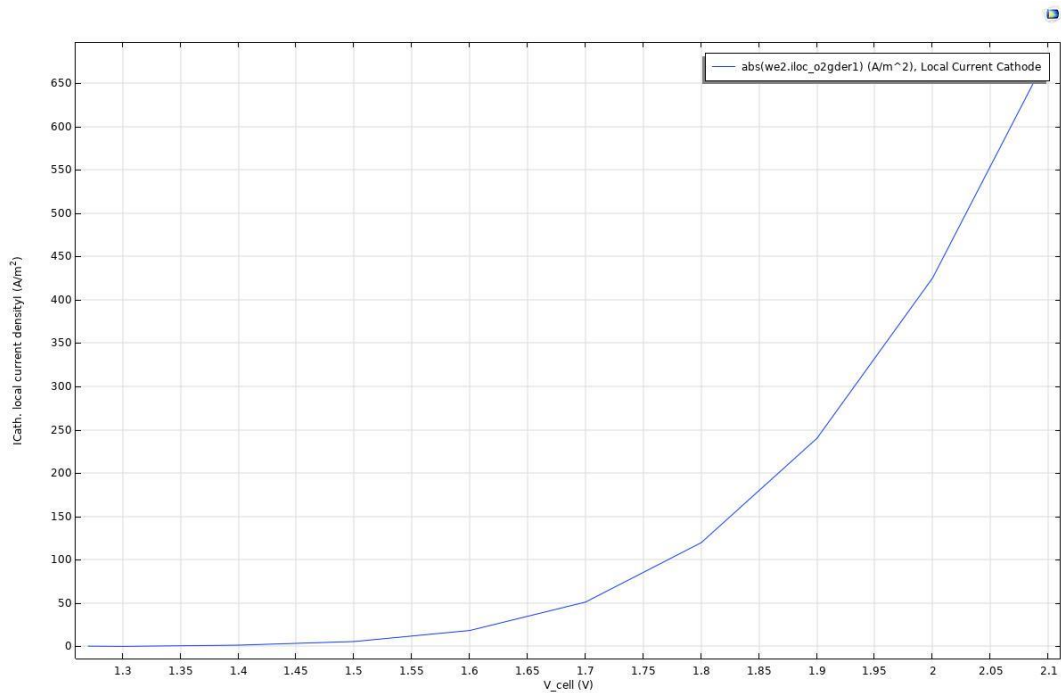


Figure 4.15 Local current density at Anode/Membrane interface

As expected, from the Butler-Volmer equations, the local current density rises with voltage rise.

Results

The water distribution is now presented. This is one of the most important parameters to analyze since the excessive consumption of water is the weak point of PEM electrolyzers.

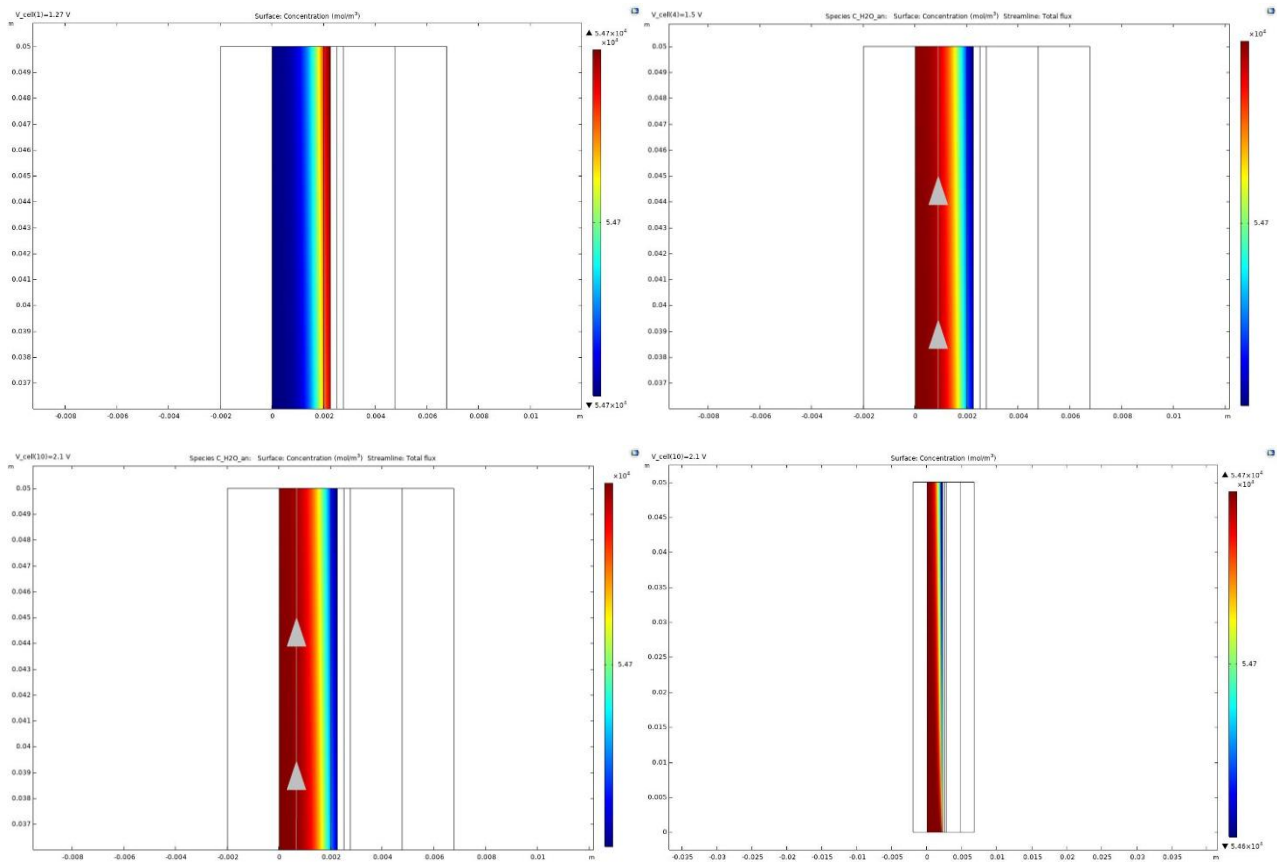


Figure 4.16 Distribution of water in the anodic compartment with different voltages. Top left 1,27 V-Top right 1,5 V-Bottom left 2,1 V- Bottom right 2,1 V overview

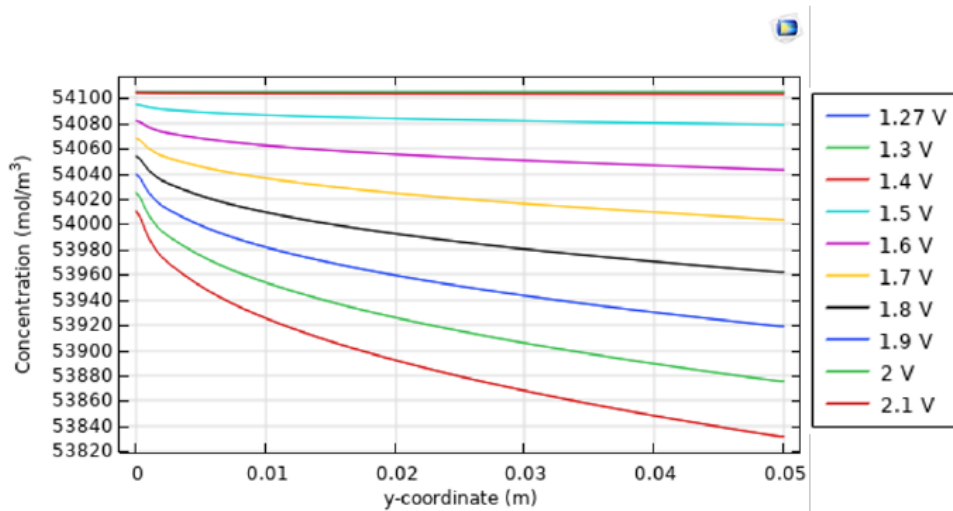


Figure 4.17 Anodic concentration of water at anode/membrane interface

The water Concentration Distribution in the Anodic Compartment is shown in figure 4.16.

Is interesting to see how the water at the beginning of the electrolysis, with low voltage, is maximum in the membrane and then shifts to the anode side. This is due to the fact that the voltage influences the water concentration field due to the impact of the local current density (figure 4.17).

Results

Since water and oxygen are reactants and products of the same half-reaction, the water concentration distribution field has the same trend of the oxygen one.

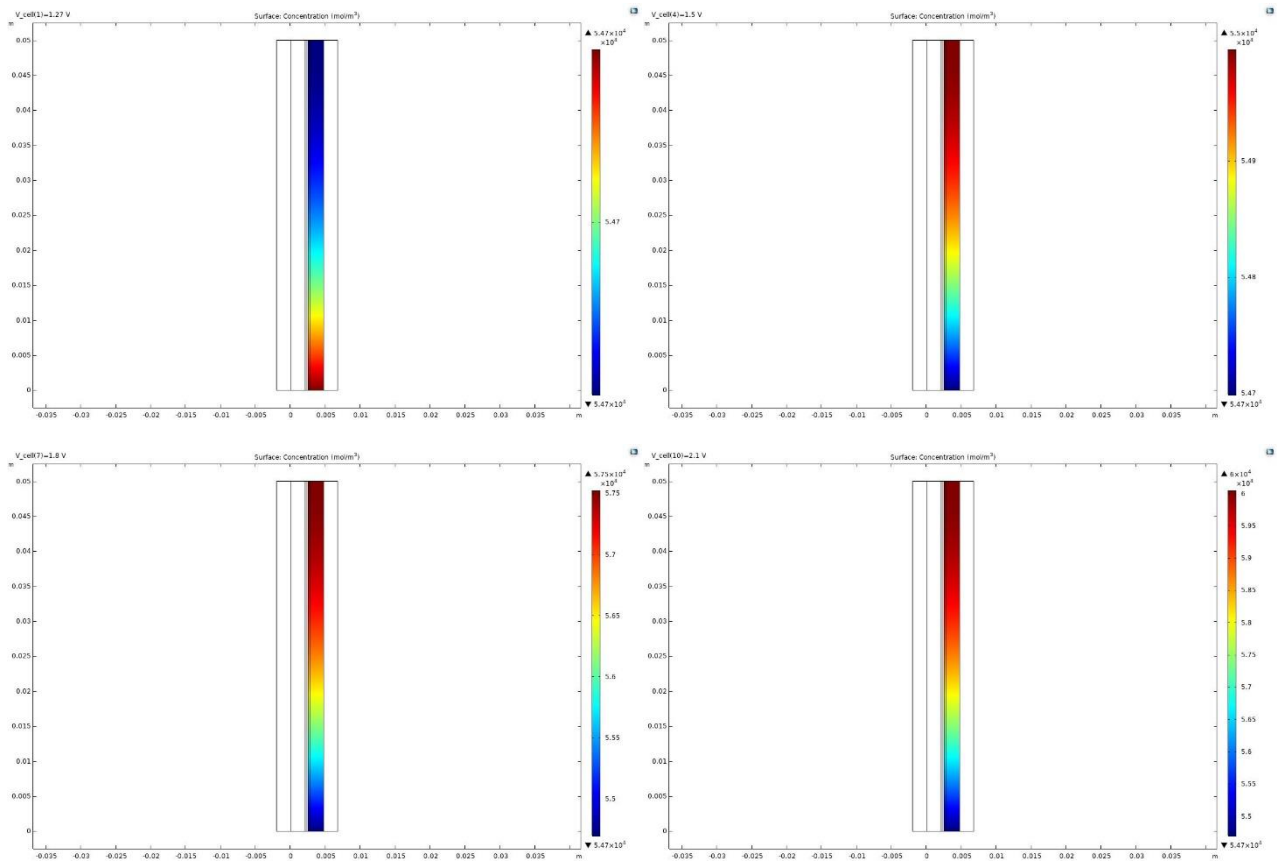


Figure 4.18 Distribution of water in the cathodic compartment with different voltages. Top left 1,27 V-Top right 1,5 V-Bottom left 1,8 V- Bottom right 2,1 V

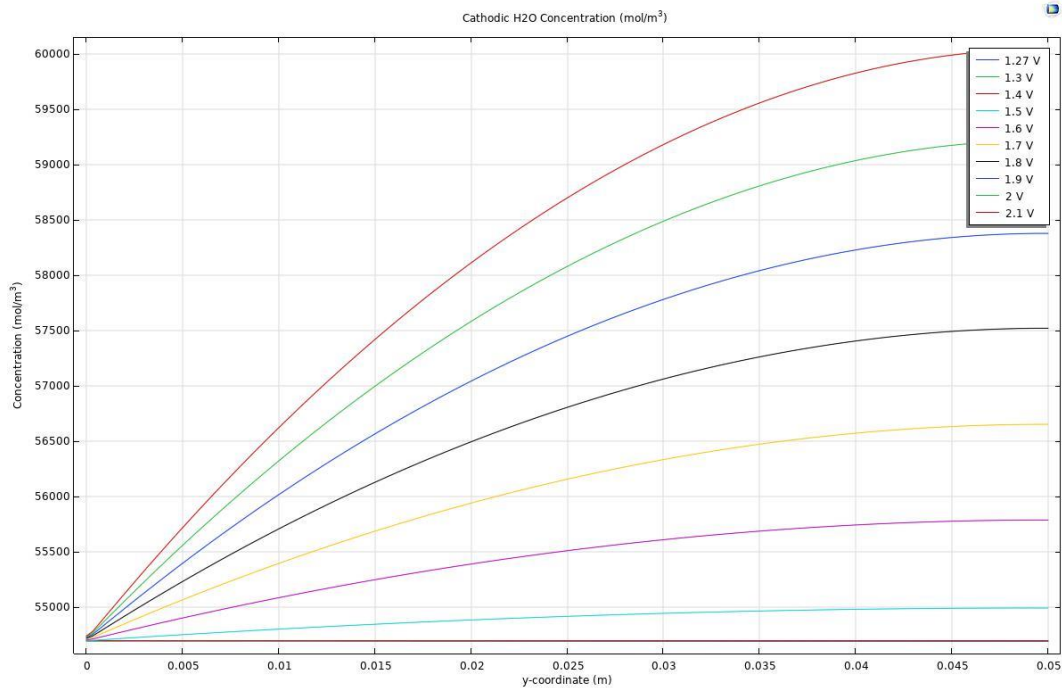


Figure 4.19 Cathodic concentration of water at cathode/membrane interface

Results

Figure 4.18 illustrates that the concentration of water at the cathode grows even when it is not participating in the process, since it is used only to keep the temperature under control. It rises with channel height and applied voltage, as shown in figure 4.19, owing to water transport over the membrane, where water moves from the anodic to the cathodic compartments, as well as electroosmotic drag, diffusion, and pressure phenomena.

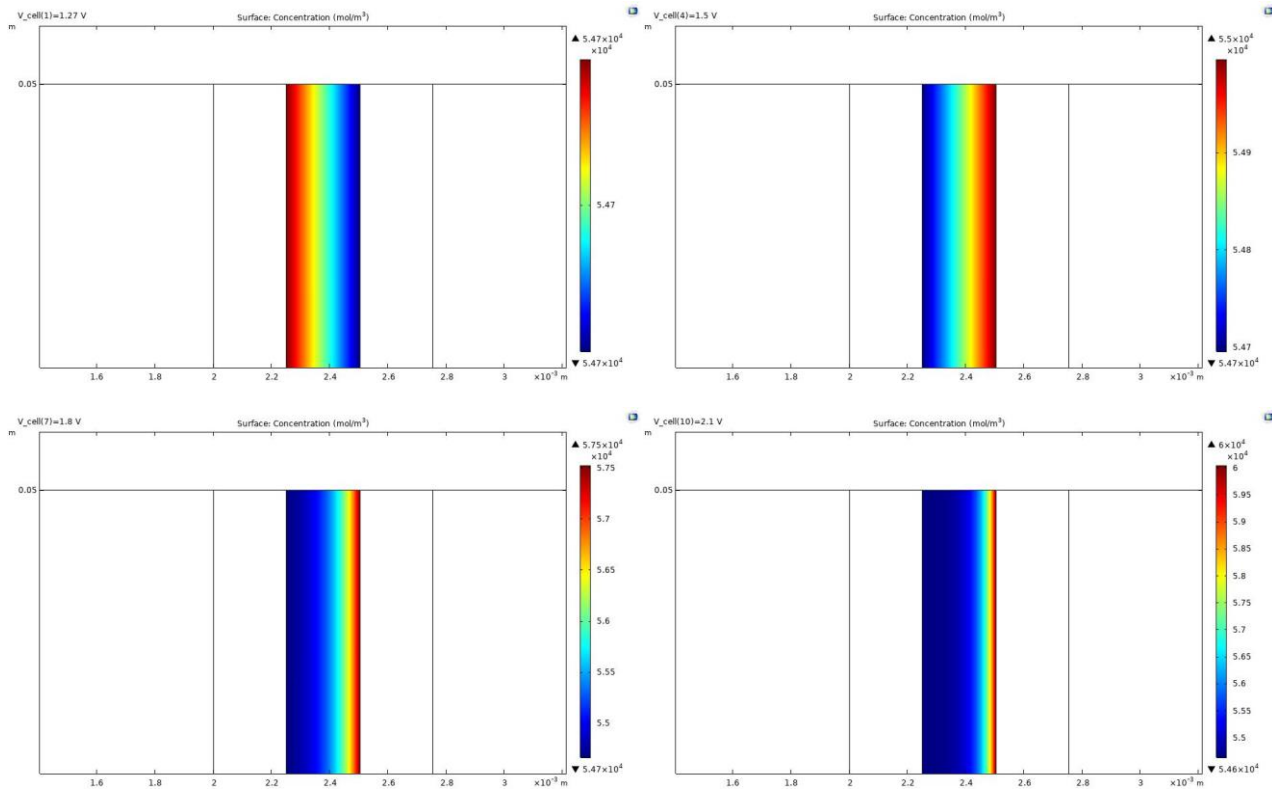


Figure 4.20 Distribution of water in the electrolyte with different voltages. Top left 1,27 V-Top right 1,5 V-Bottom left 1,8 V- Bottom right 2,1 V

The water distribution within the membrane shown in figure 4.20 depicts an intriguing water flow rate behaviour in the membrane. It is connected to the existence of certain waves, which seem to condense near the cathodic interface, causing the applied voltage to rise.

Due to its direct dependency on current, the electroosmotic (figure 4.21) contributes the most to the total flow through the membrane. It is, in fact, order of magnitudes more than Diffusion Membrane Flow (figure 4.22).

Results

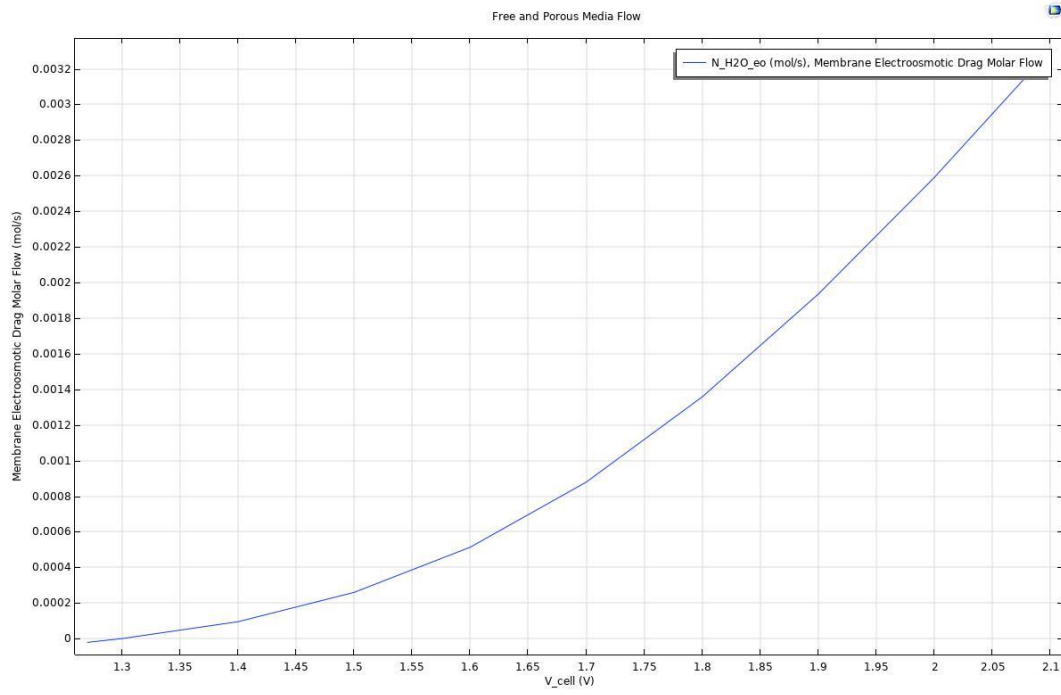


Figure 4.21 Membrane Electroosmotic Drag Molar Flow

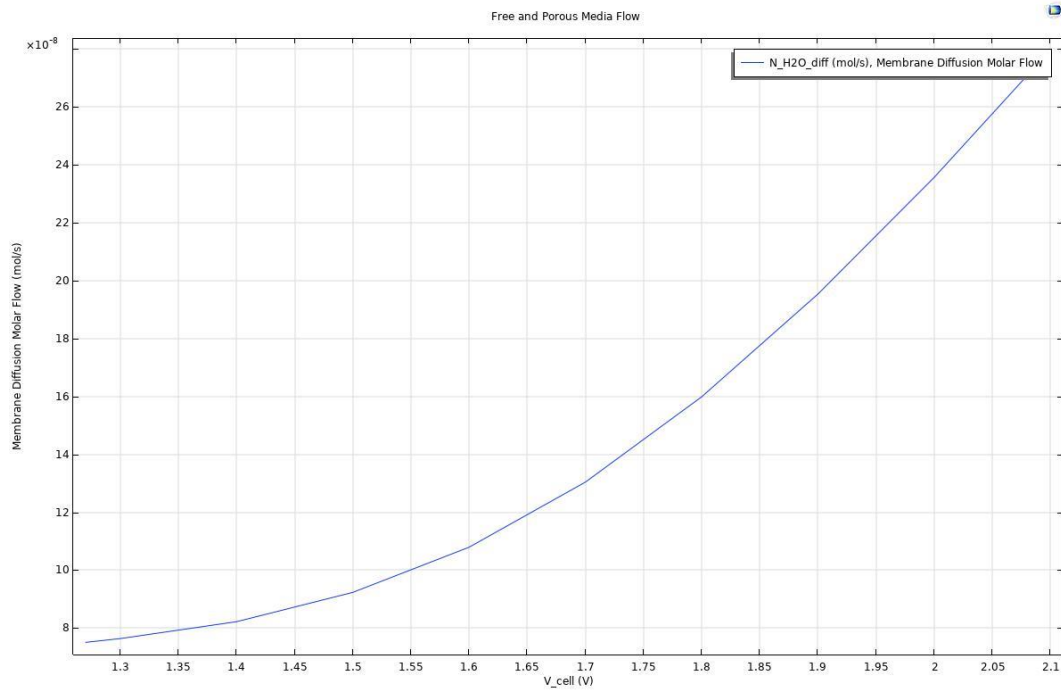


Figure 4.22 Membrane Diffusion Molar Flow

Results

Temperature is one of the most essential thermodynamic characteristics in the system; it is critical for the electrolyzer's proper functioning.

Figure depicts the temperature distribution for various applied voltage levels.

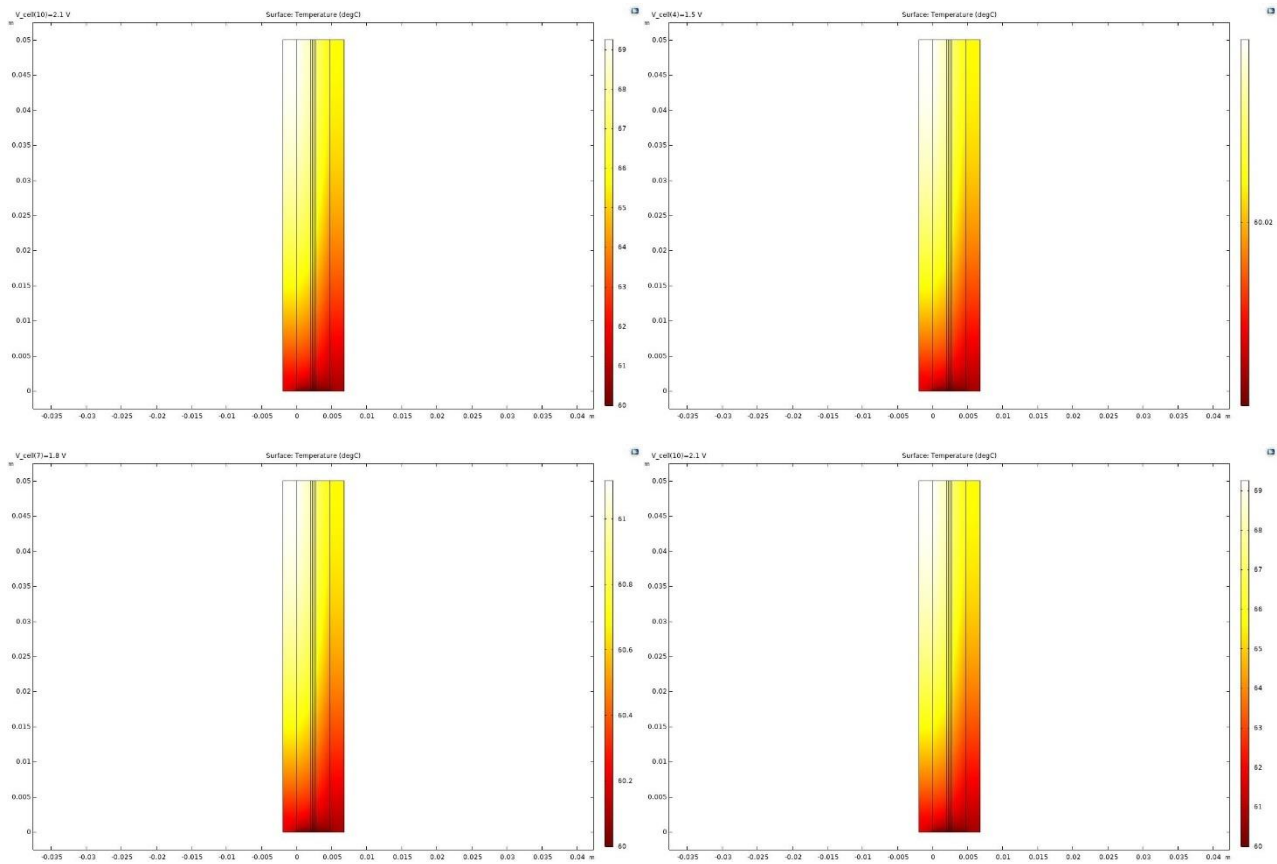


Figure 4.23 Temperature Distribution for different voltage values: Top left 1,27 V-Top right 1,5 V-Bottom left 1,8 V- Bottom right 2,1 V

Temperature profiles at the anode/electrolyte interface and the cathode/electrolyte Interface are shown in the graphs below.

Figure depicts the temperature profiles of the mixes at the interfaces, demonstrating the behaviour of temperature gradients and their reliance on the vertical coordinate.

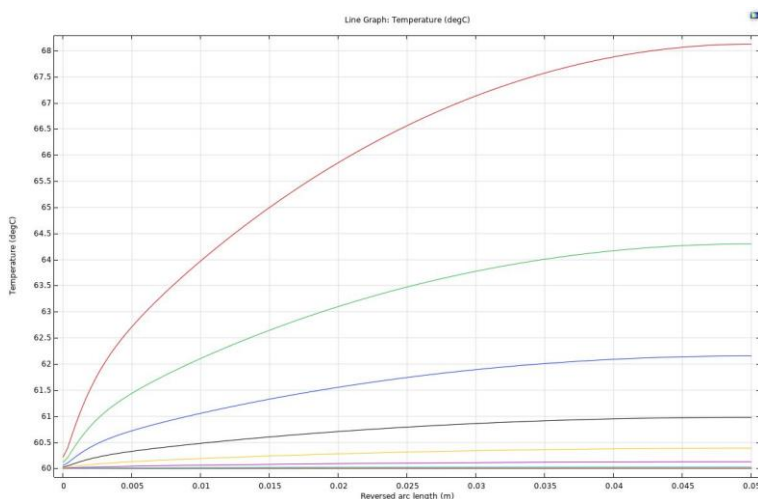


Figure 4.24 Temperature profile at Anode in function of arch length

Results

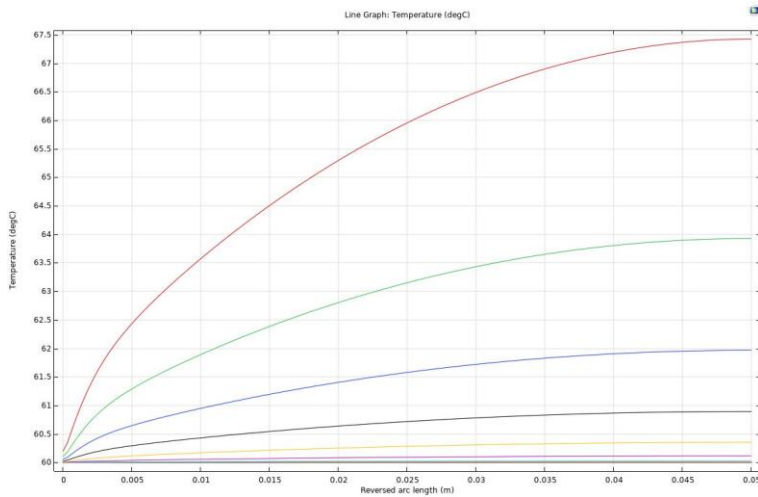


Figure 4.25 Temperature profile at Cathode in function of arch length

The temperature gradients are seen in figure 4.26. The cathodic compartment has a larger temperature gradient than the anodic compartment because the water flow velocity in the cathodic compartment is lower.

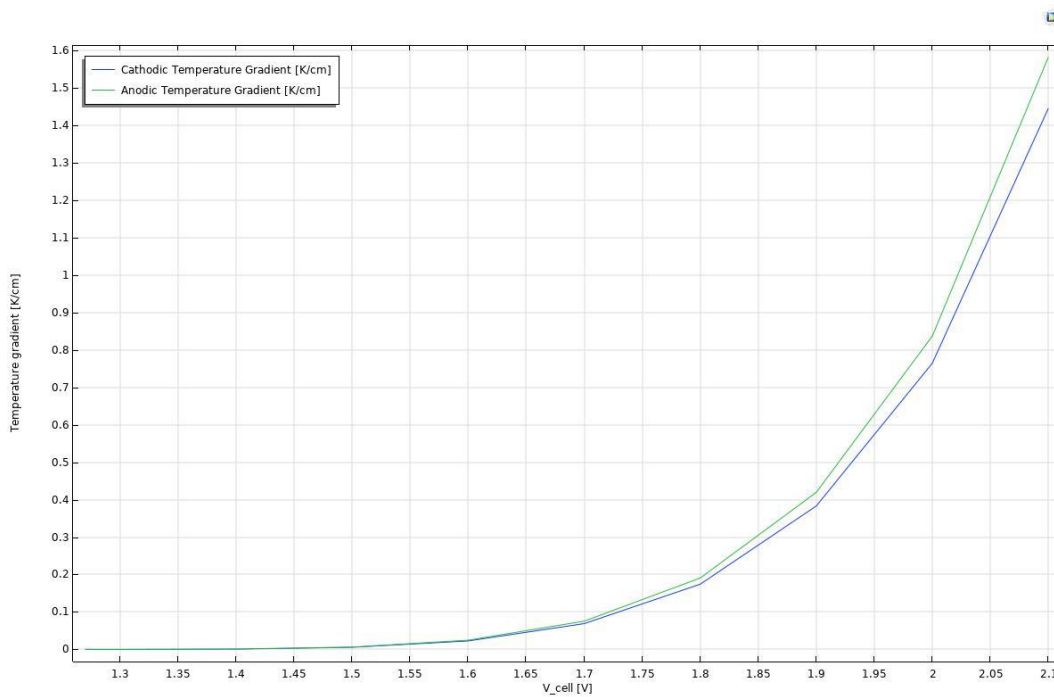


Figure 4.26 Temperature gradients

Results

4.3 3D Single-phase Laminar flow model

For the 3D Model simulation, the same operating conditions were used, $T = 60^\circ\text{C}$ and $p = 0.5$ bar, but with a different Voltage sweep: 1,27 – 1,3 – 1,35 – 1,4 – 1,5 – 1,6 – 1,7 – 1,8 – 1,9 – 2 – 2,1 – 2,2 – 2,3 – 2,4 V, to have a clearer view of the serpentine flow field architecture.

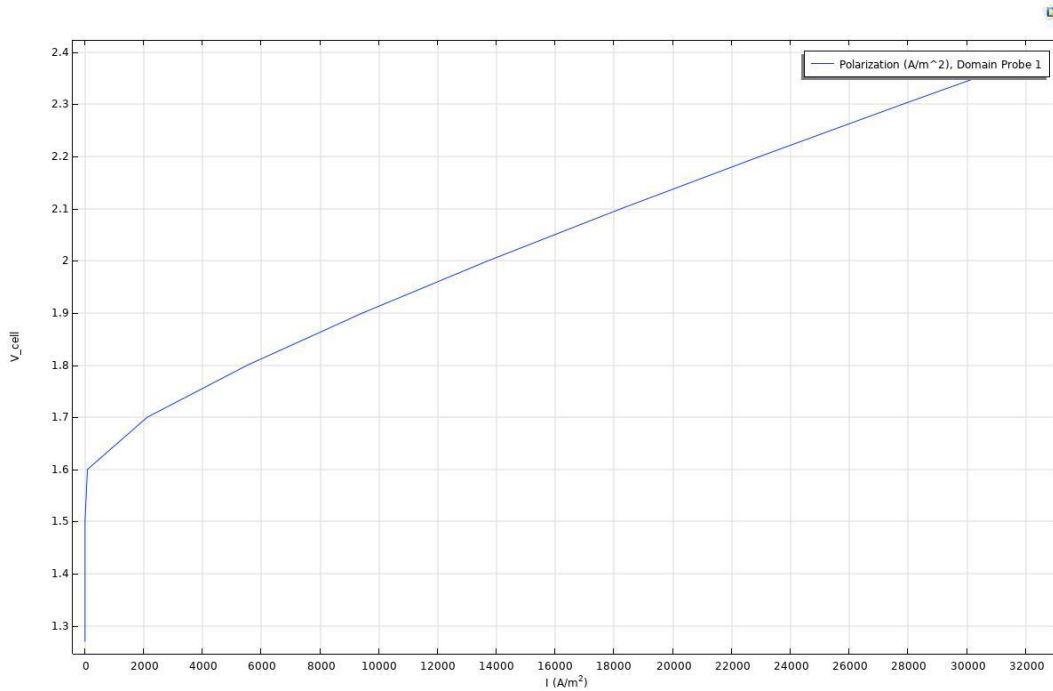
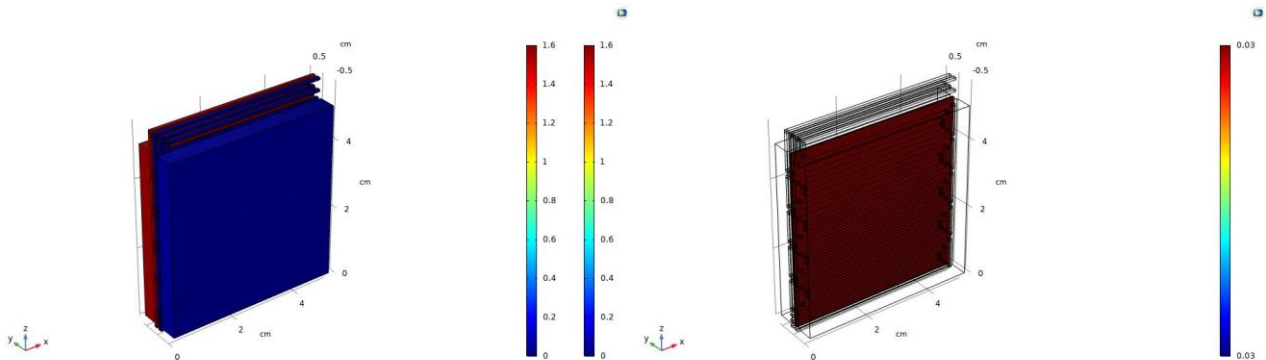


Figure 4.27 Polarization curve $T=60^\circ\text{C}$ $p=0.5$ bar



Results

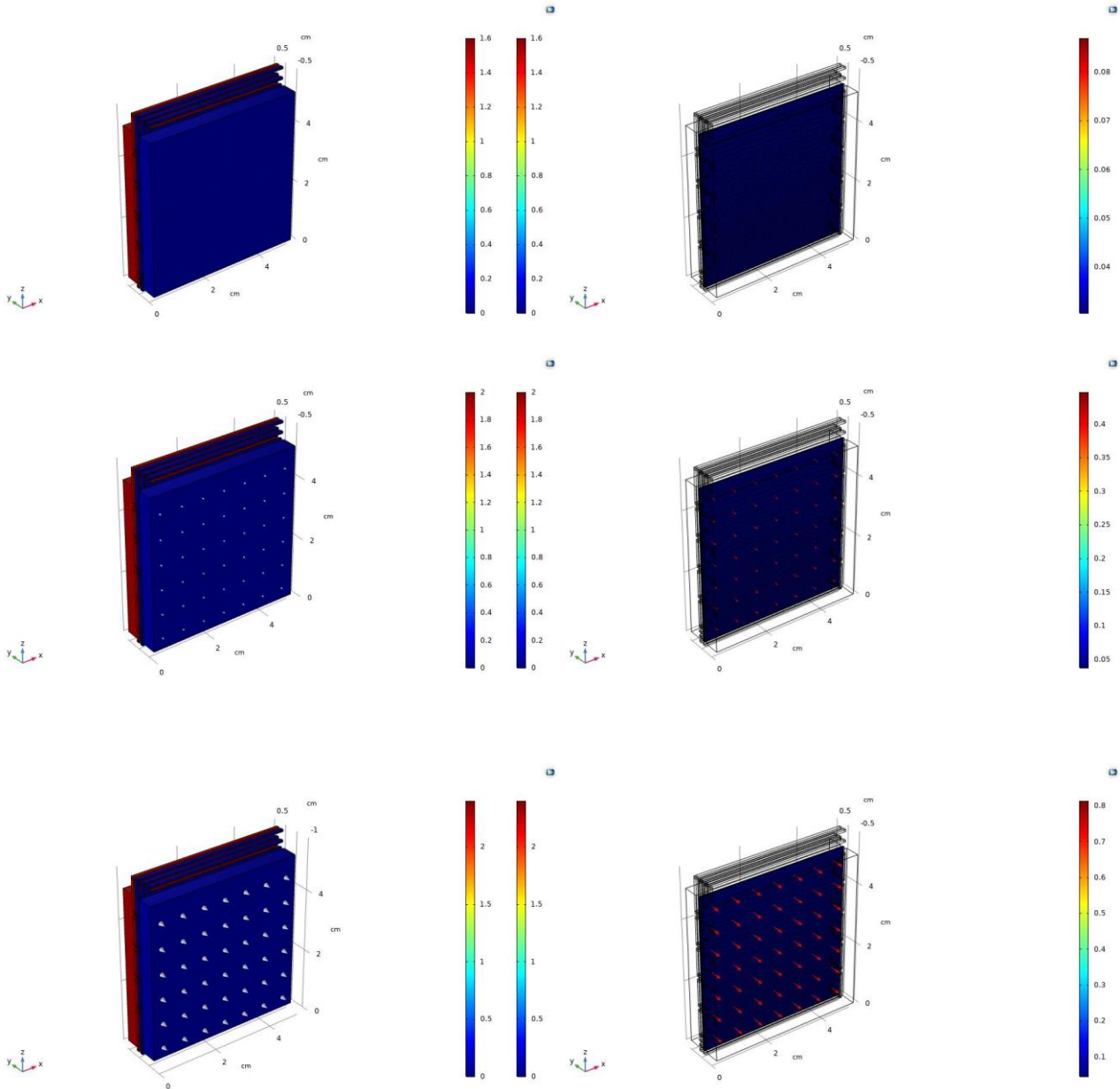


Figure 4.28 Electric Potential (left) and Electrolyte potential (right) for different value of voltages: from top to bottom, for each row, 1,27 – 1,6 – 2 – 2,4 V

In figure 4.28 Electrode and Electrolyte Potential respect to ground is reported. The arrows represent for the Electric Potential the Electrode Current Density Vector, and for the Electrolyte Potential the Electrolyte Current Density vector.

Interesting result is that the current vector field is visible only for voltage values higher then 1,6 V, which is a confirm of the Polarization curve trend, figure 4.27, where the curve first useful point is for a value of 1,7 V and corresponds to a current density of $0,2 \text{ A/cm}^2$.

Results

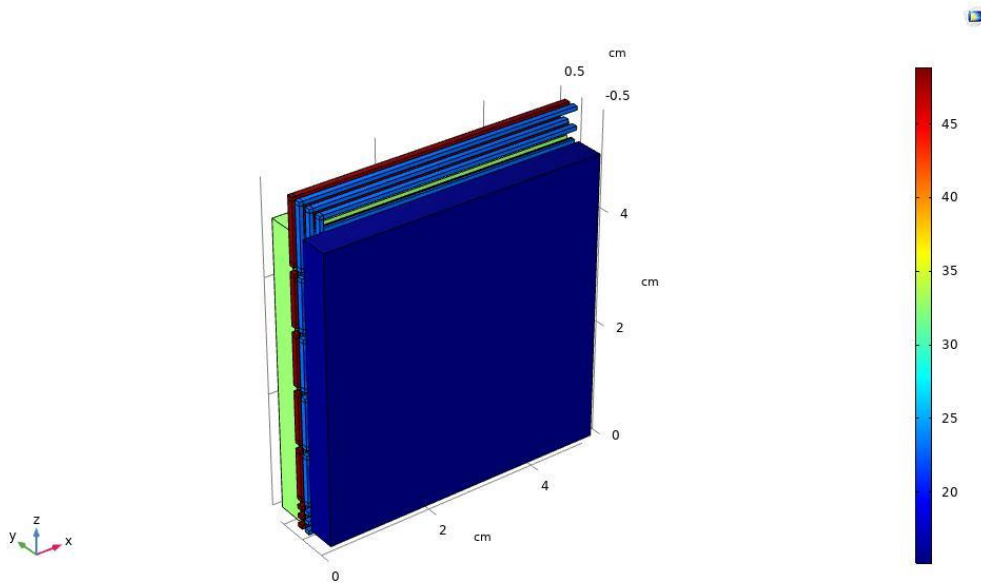


Figure 4.29 Relative Humidity

The Relative Humidity distribution is very similar to the 2D Model, since the same input carrier gas are used, as expected.

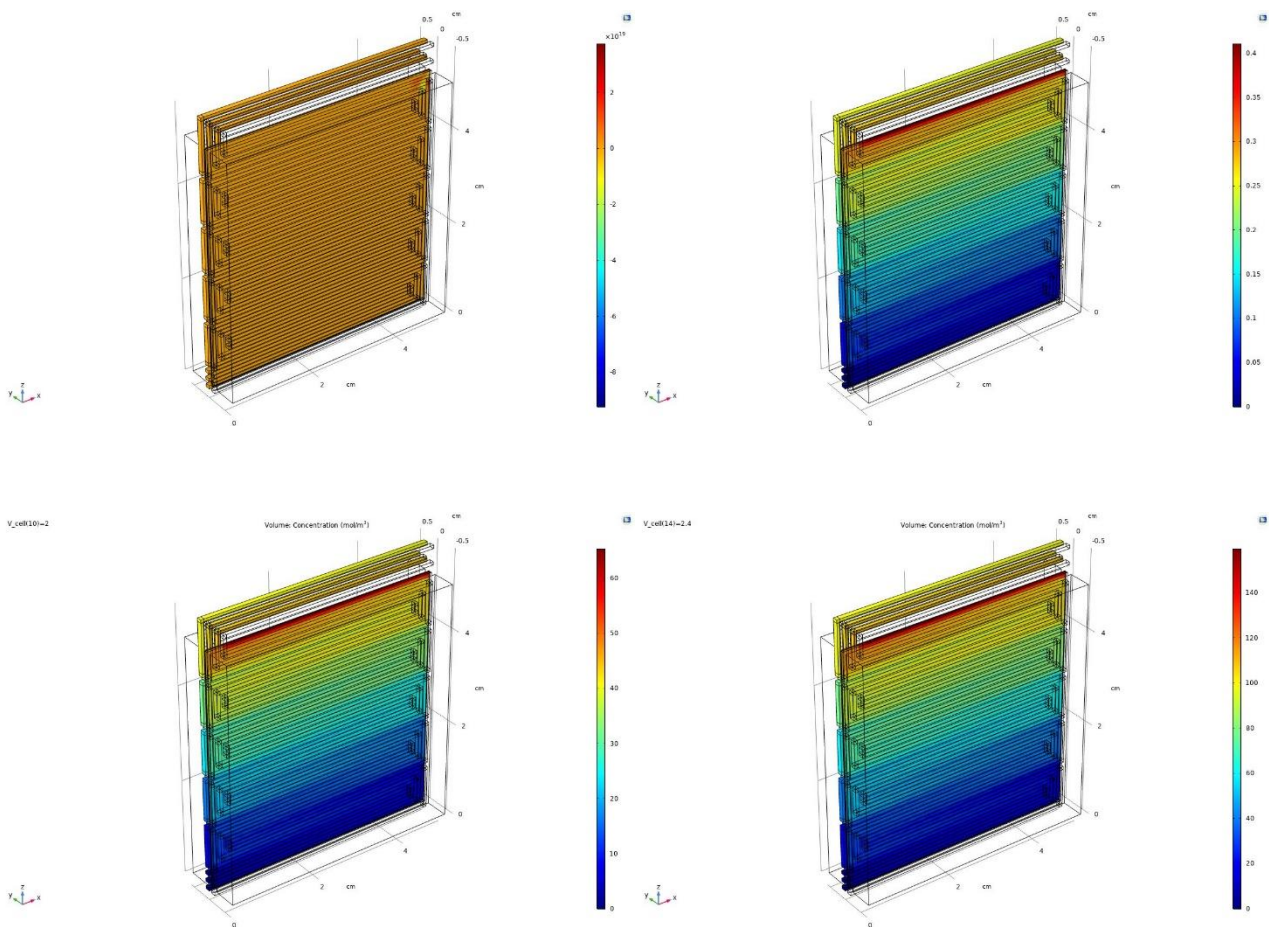


Figure 4.30 Oxygen Concentration in anodic channels for different voltage values: Top left 1,27-Top right 1,6-Bottom left 2-Bottom right 2,6 V

For the 3D Model, we can see that the oxygen concentration in the flow fields patterns vary significantly depending on the input voltages.

Results

For input voltages lower than 2 V the oxygen distribution is maximum 0.4 mol/m^3 , so values very close to 0.

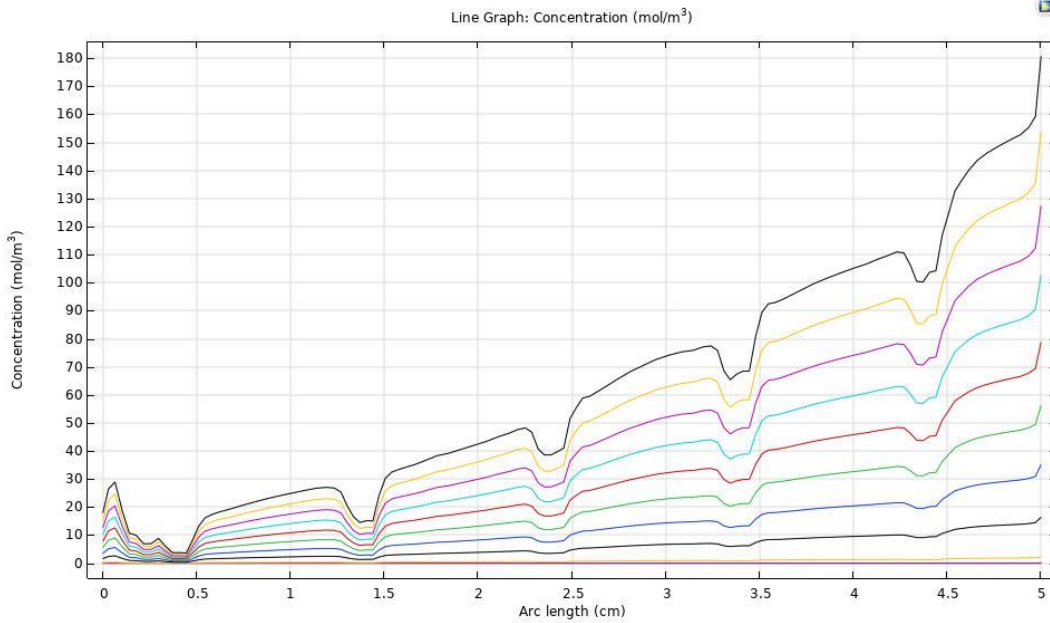
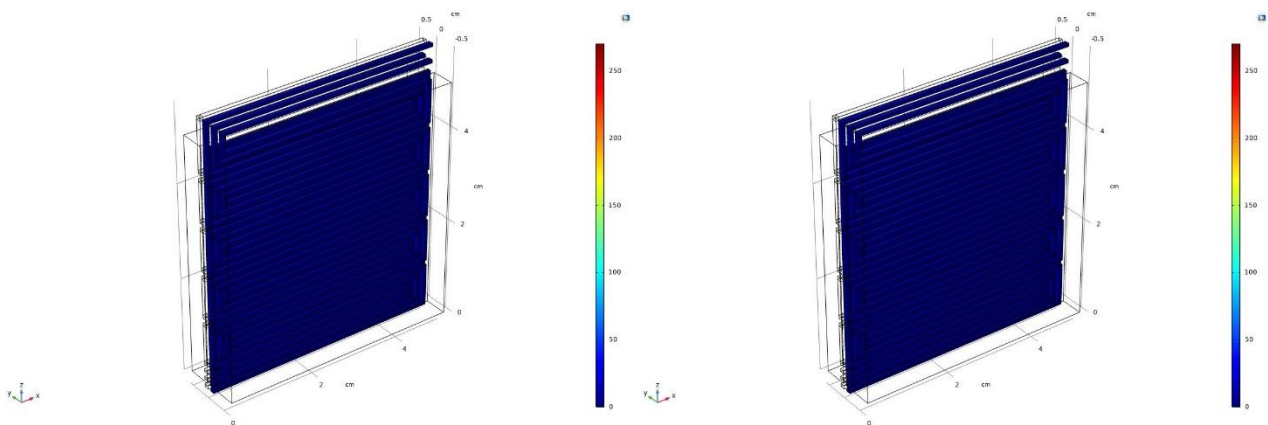


Figure 4.31 Oxygen Concentration at anode/membrane interface

As for the 2D model, the oxygen concentration at electrode/membrane interface rises with the arc length, since voltage and as a consequence local current density rises.



Results

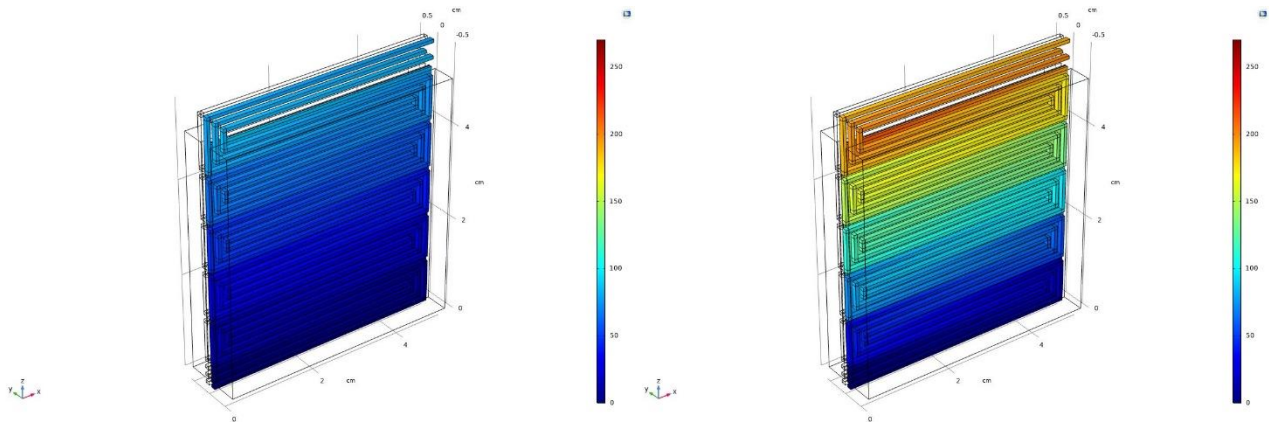


Figure 4.32 Hydrogen concentration in cathodic channels for different voltage values: Top left 1,27-Top right 1,6-Botto left 2-Bottom right 2,6 V

In terms of hydrogen distribution, figure 4.32 depicts the 3-D distribution of hydrogen in porous electrodes and channels.

As can be seen (figure 4.33), hydrogen production rises with increasing z-coordinate (height) but remains constant in the other two directions. They are thicker in the upper region of the porous electrode when considering the highest numerical values of hydrogen concentration. The last section of the channel also shows high hydrogen concentrations, indicating a rise in concentration along the triple serpentine.

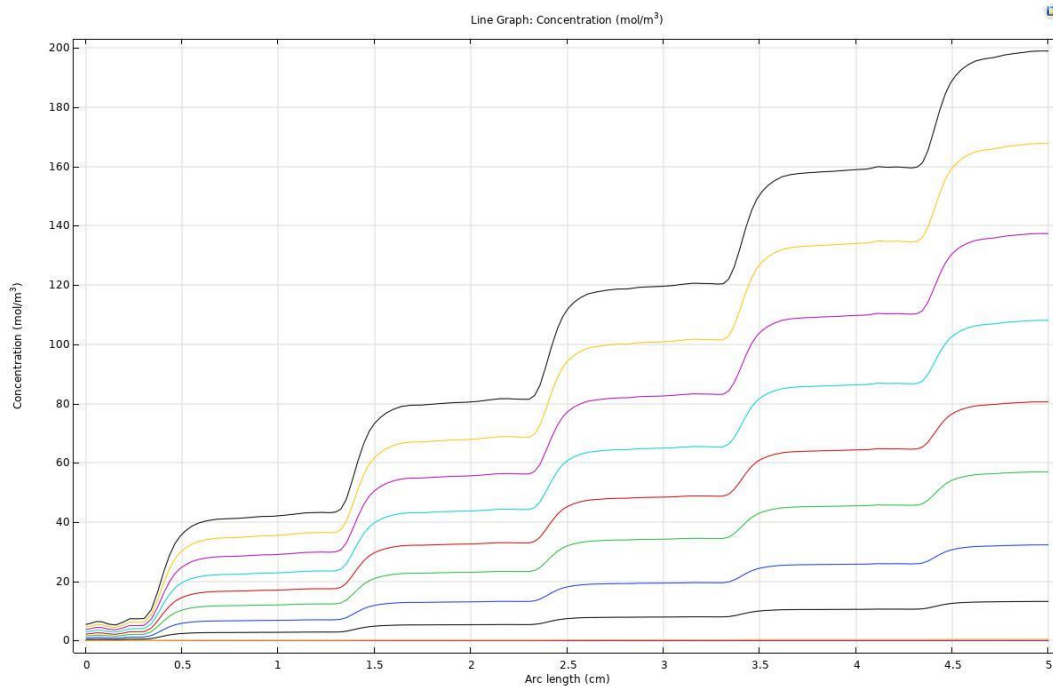


Figure 4. 33 Hydrogen Concentration at cathode/membrane interface

Results

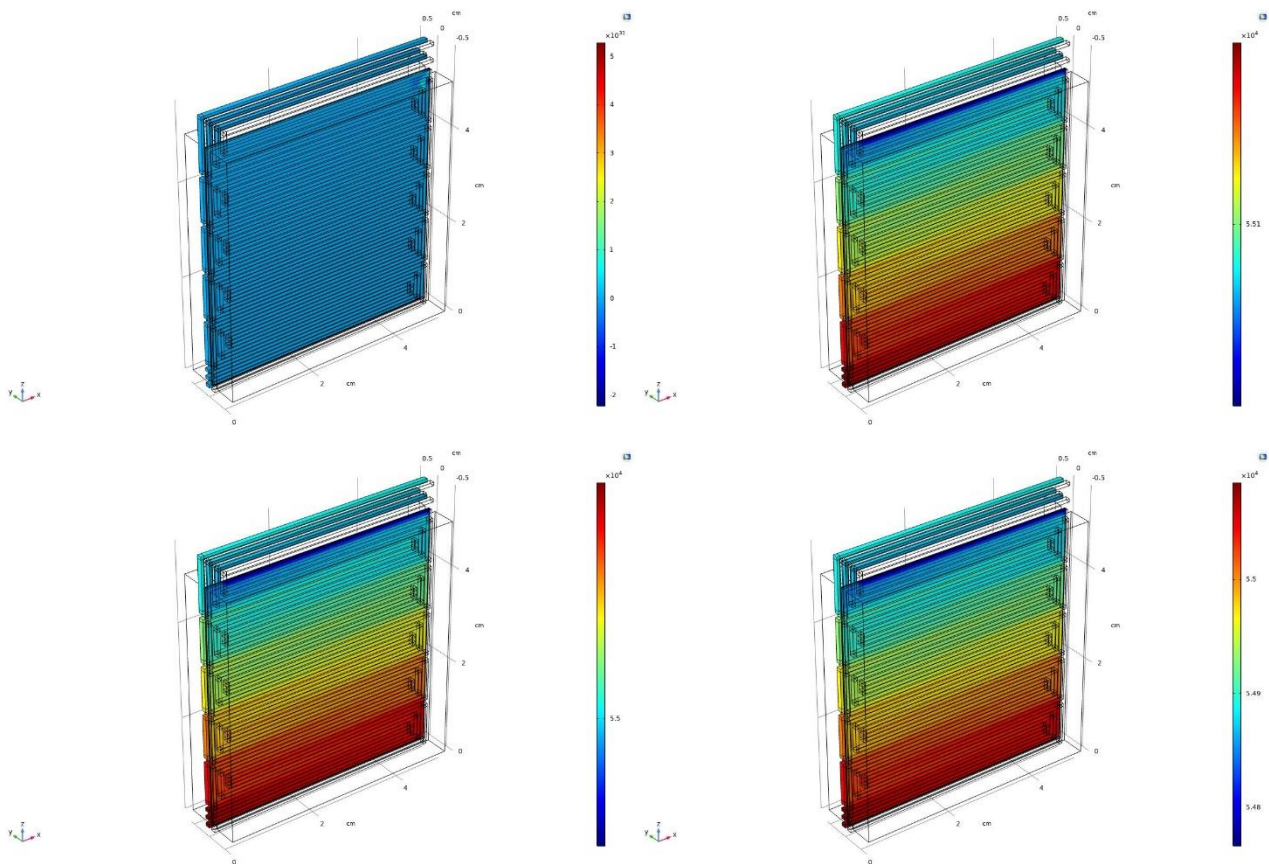


Figure 4.34 Water concentration in anodic channels

Water level in anodic compartments significantly rises with voltages higher than 1,27, then it becomes quite steady at around 55000 mol/m^3 , same seen in the 2D simulation.

Water level of course increases with hydrogen concentration along the z direction, since it is a part of the same semi reaction.

Results

4.4 2D Multi-phase Turbulent Flow Model

In this simulation the main turbulence variables are presented, with a focus on the overpotential caused by bubbles.

The turbulent interface used is the RANS $k-\omega$, used for value of Reynolds number between 2000 and 3000.

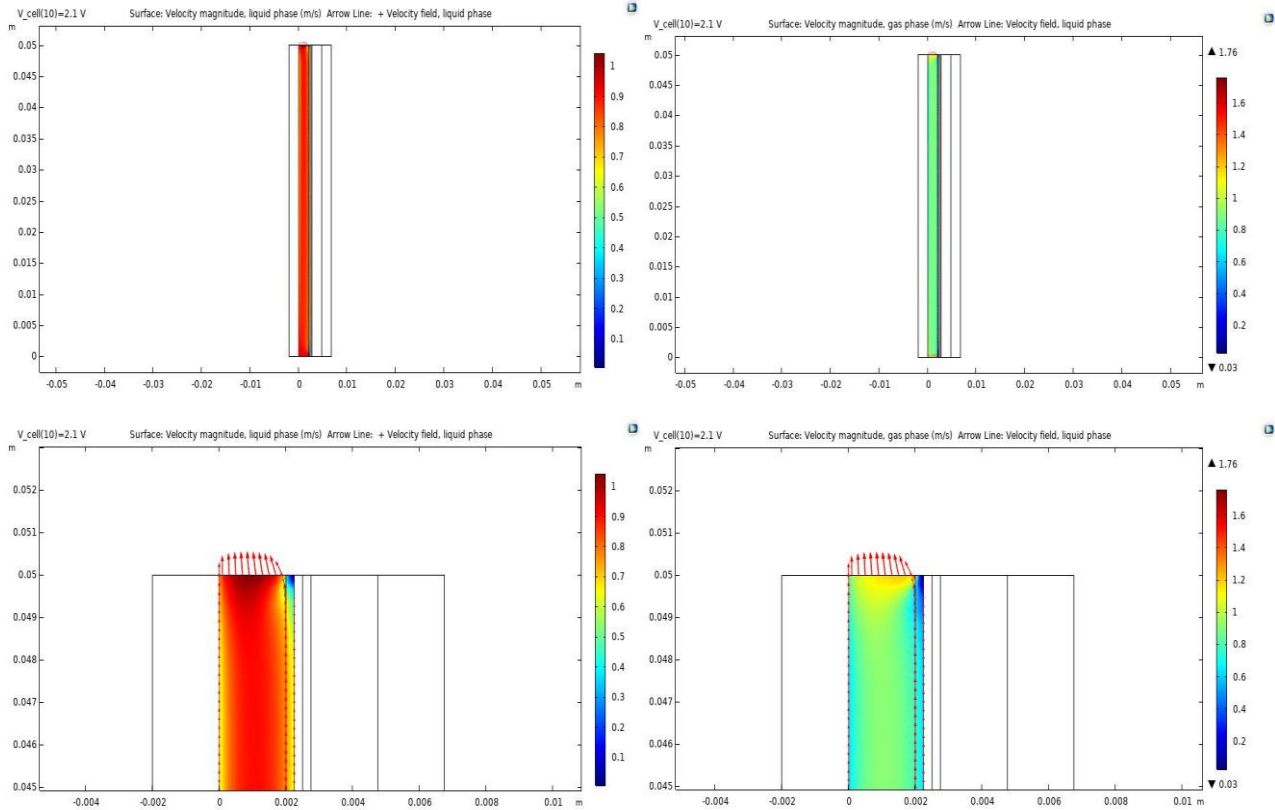


Figure 4. 35 Velocity distribution of liquid (left) and gas (right) phase.

In figure 4.35 is shown the speed of the two phases in the anodic domain, gas phase and liquid one.

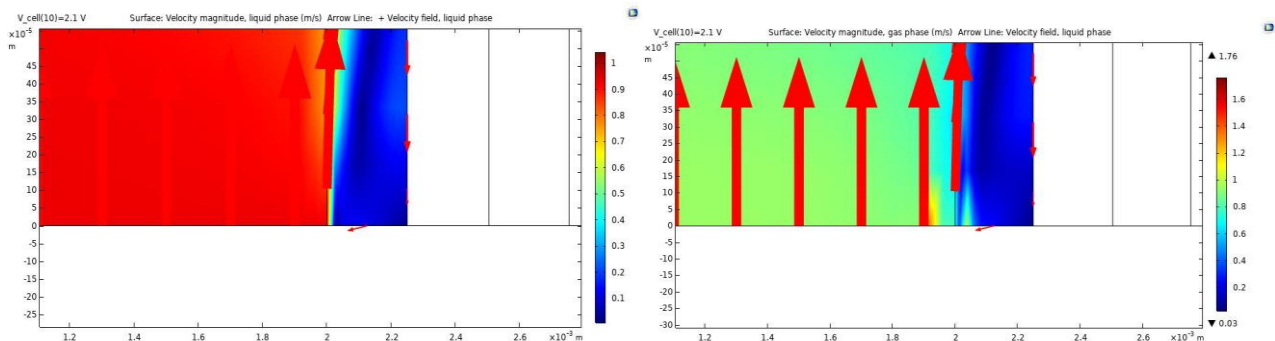


Figure 4. 36 Vortex formation

As presented in figure 4.36 there is a zone at the channel intake, near the electrolyte contact, where the velocity direction is reversed, suggesting the existence of a small vortex, which is due to the turbulences created by the bubbles on the fluid flow.

Results

An important result of the Multiphase model is the fraction of volume occupied by the bubbles, since is fundamental to understand the size of the bubbles and their impact on the electrodes.

The bubble electrode coverage is important in understanding the influence of bubbles on the lowering of the usable electro-active area required for the splitting process. The behaviour of bubble volume fraction at electrode for various applied voltages is shown:

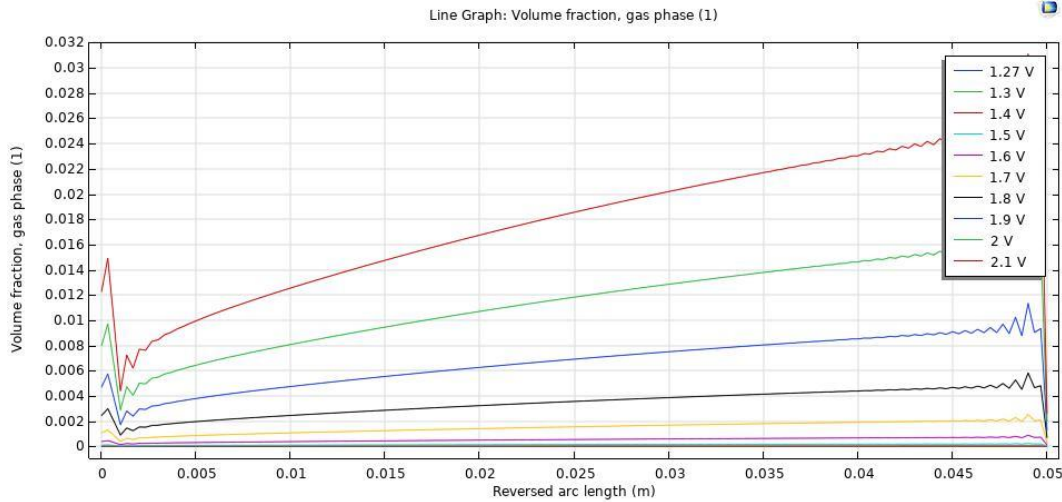


Figure 4. 37 Volume fraction in function of the height

The bubbles, clog the pores, resulting in an extra overpotential. Figure 4.38 shows a plot of the overpotential in function of the length of the anodic channel.

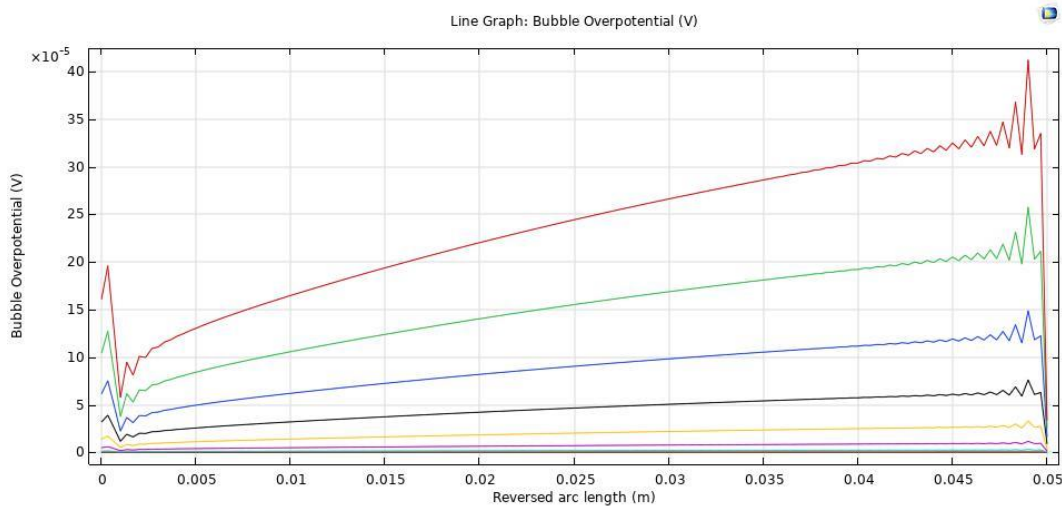


Figure 4. 38 Overpotential due to bubble formation

Results

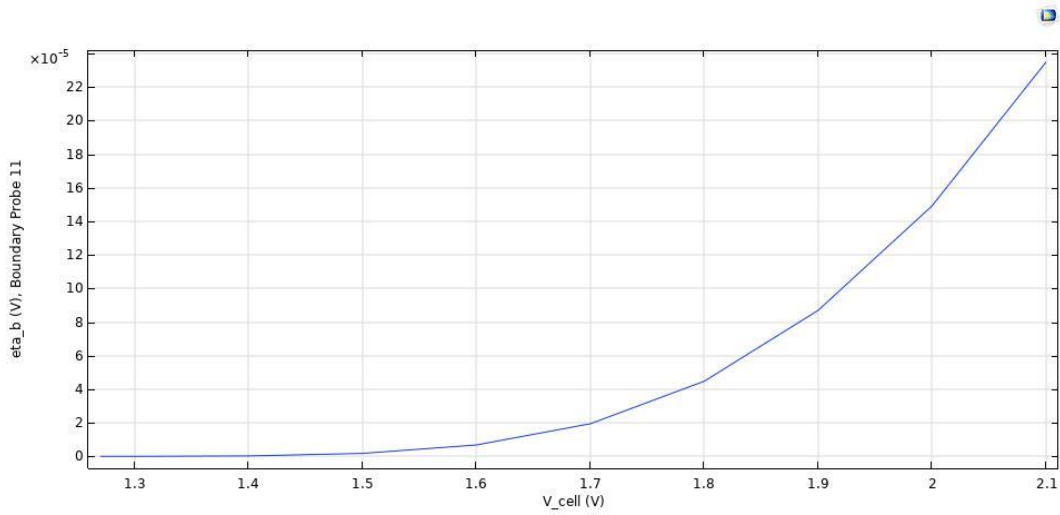


Figure 4. 39 Bubble overpotential in function of the applied voltage

The integral value of the Bubble Overpotential at the electrode/electrolyte contact vs the applied voltage is shown in Figure 4.39.

4.5 3D Single Phase Turbulent Flow Model

In this section, a comparison between 3D turbulent model and 3D laminar model seen above is reported. The turbulent model used in this section is again the RANS $k-\omega$.

First, a brief report on the turbulent variables is presented.

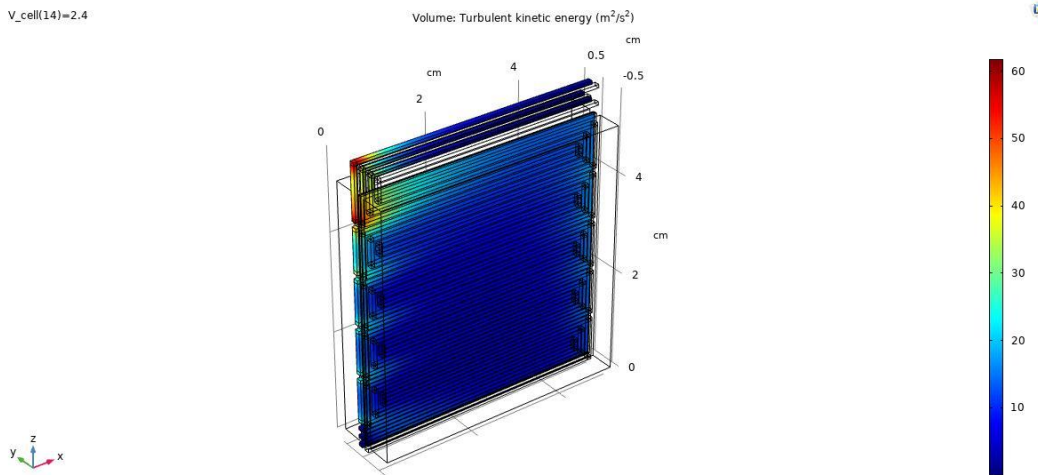


Figure 4. 40 Turbulent kinetic energy distribution

Turbulent kinetic energy is simply defined as a mean variation in kinetic energy per unit mass. The root mean square (RMS) fluctuation in the magnitude of the flow velocity is defined as this quantity. The total turbulent kinetic energy is just the sum of the variations in each velocity component since flow velocity is a vector.

If the flow was purely laminar along all three orthogonal directions, then the turbulent kinetic energy would be zero, meaning all kinetic energy would be accounted for in laminar flow.

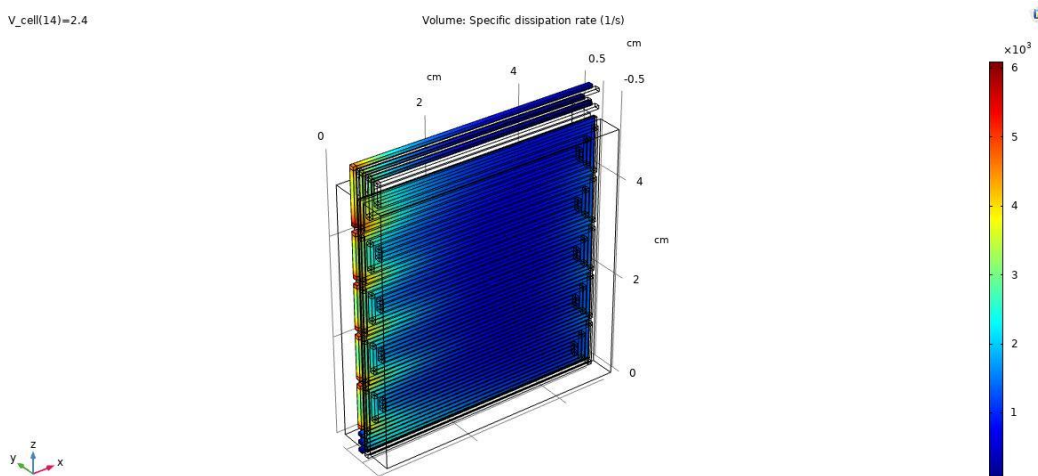


Figure 4. 41 Specific dissipation rate distribution

Results

Turbulent flow is made up of eddies of varying sizes, and the size range expands as the Reynolds number rises. Interactional forces between the eddies cause kinetic energy to cascade down from big to tiny eddies. The energy of the eddies dissipates into heat at a very tiny scale owing to viscous forces. The energy dissipation rate is a parameter that determines how much energy is wasted in a turbulent flow due to viscous forces.

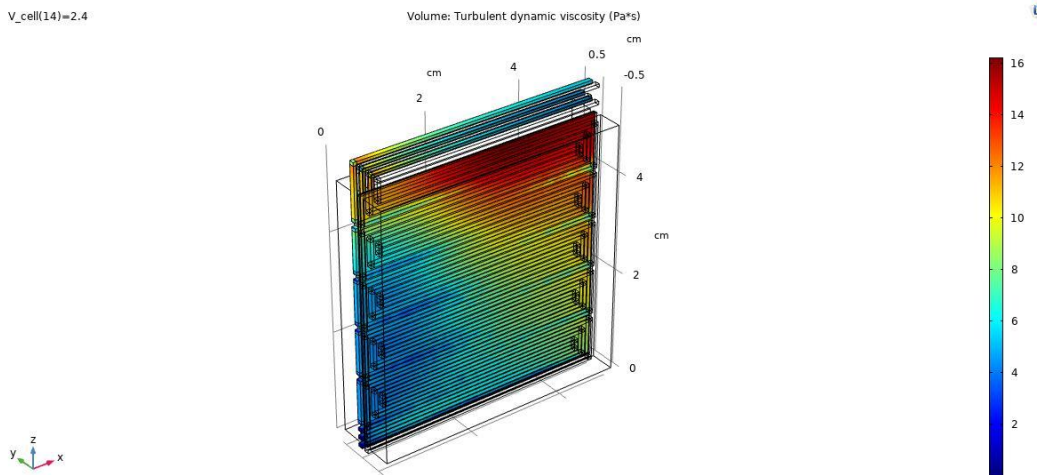


Figure 4. 42 Turbulent dynamic viscosity distribution

When the flow is laminar, the sole mechanism for diffusion inside the flow is molecular movements. The metric to quantify this phenomenon is viscosity, which is a diffusion coefficient.

When the flow becomes turbulent, however, the diffusion process is not only done by molecular movements, but also by eddies motions, which are much enhanced. As a result, while utilizing eddy viscosity models to describe turbulence, we must add turbulent viscosity to the molecular viscosity to increase the diffusion coefficient. Both momentum and heat transfer equations will be affected by this coefficient.

4.5.1 Differences with laminar model

First differences that can be evaluated from the comparison with the laminar model are the velocity and vorticity magnitude distribution in the anodic channels, where the turbulent RANS model is applied.

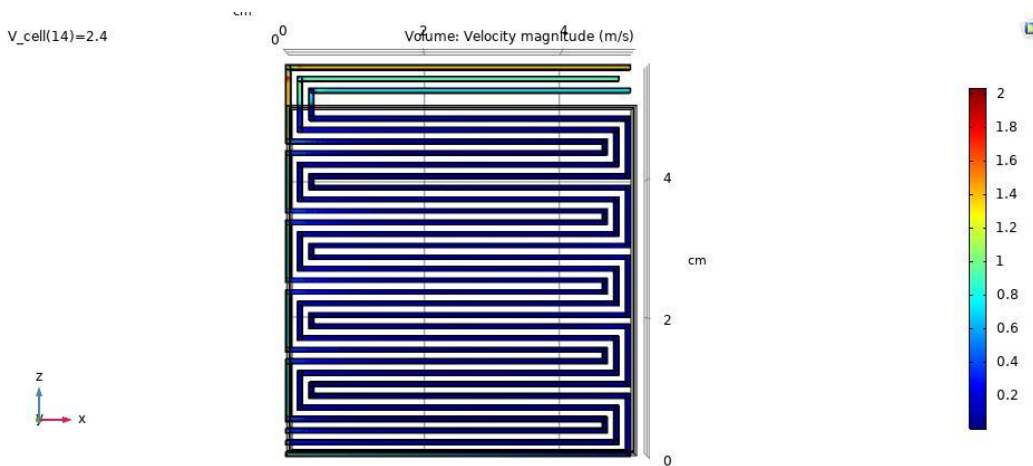


Figure 4. 43 Velocity magnitude distribution in turbulent flow model

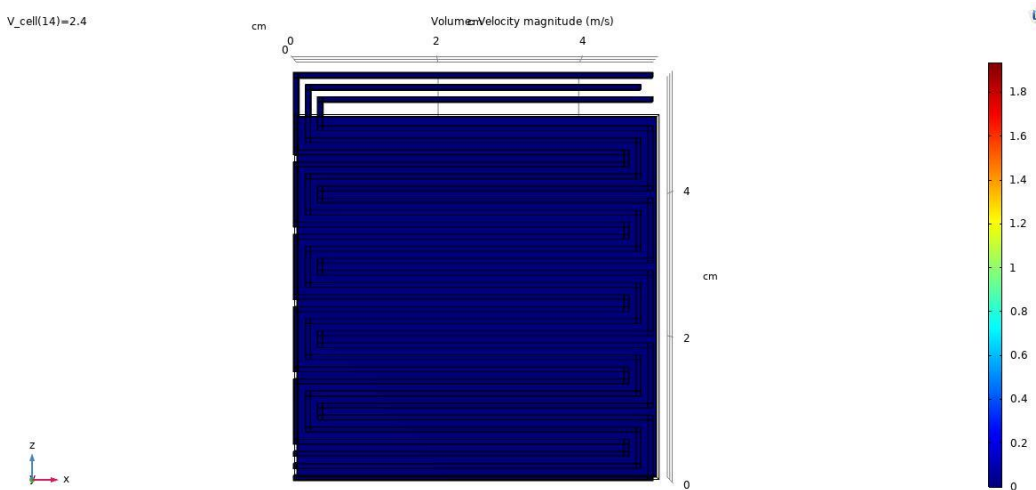


Figure 4. 44 Velocity magnitude distribution in laminar flow model

From the comparison between figures 4.43 and 4.44 it can be noticed that the velocity magnitude is more relevant in the turbulent configuration, especially in proximity of the outlet channels. This is due to the higher amount of kinetic energy in the turbulent flow model and the increase of diffusion processes, caused by the turbulent dynamic viscosity.

Results

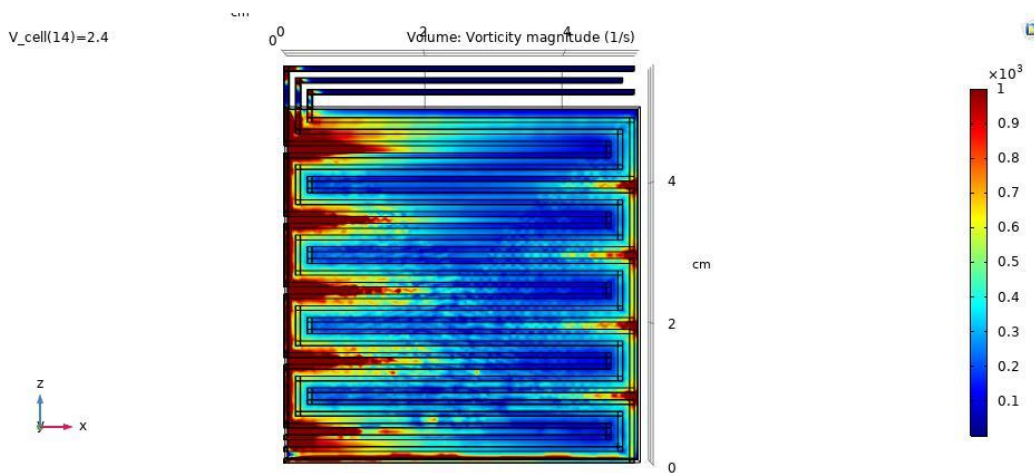


Figure 4.45 Vorticity magnitude distribution in turbulent flow model

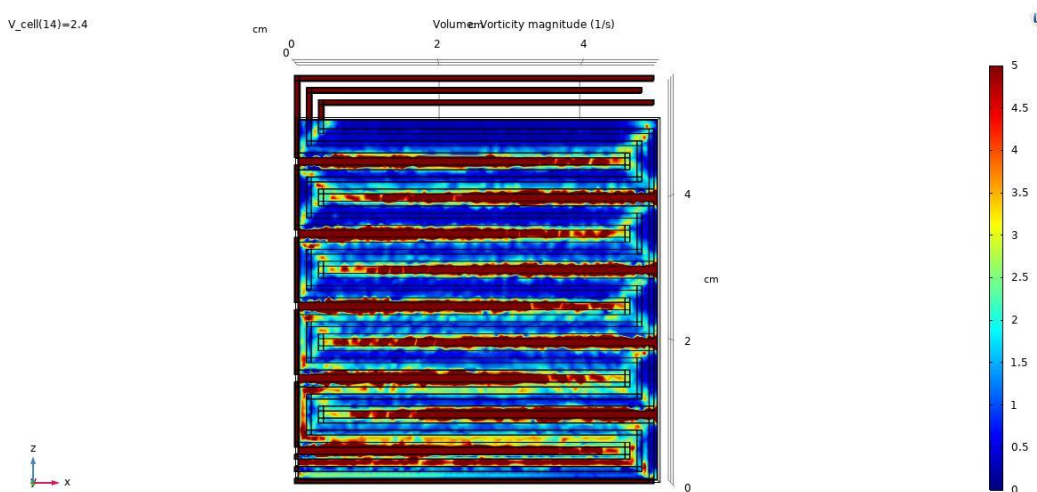


Figure 4.46 Vorticity magnitude distribution in laminar flow model

A comparison of vorticity is reported in figure 4.45 and 4.46.

The vorticity field is twice the rotation rate of fluid particles and is the curl of the velocity field. The vorticity field is a vector field, and vortex lines are calculated using a tangency condition identical to the one used to calculate streamlines in the fluid velocity field.

Vortex lines are transported by the flow and cannot finish inside the fluid, limiting their topology. Vorticity is most often seen near solid borders, where it spreads into the flow due to viscosity.

It can be seen that vorticity is two orders of magnitude higher in the RANS model in comparison with the laminar one, especially in corners and edges.

Regarding concentration, the first difference that can be seen with the laminar model is the oxygen concentration at anode.

Results

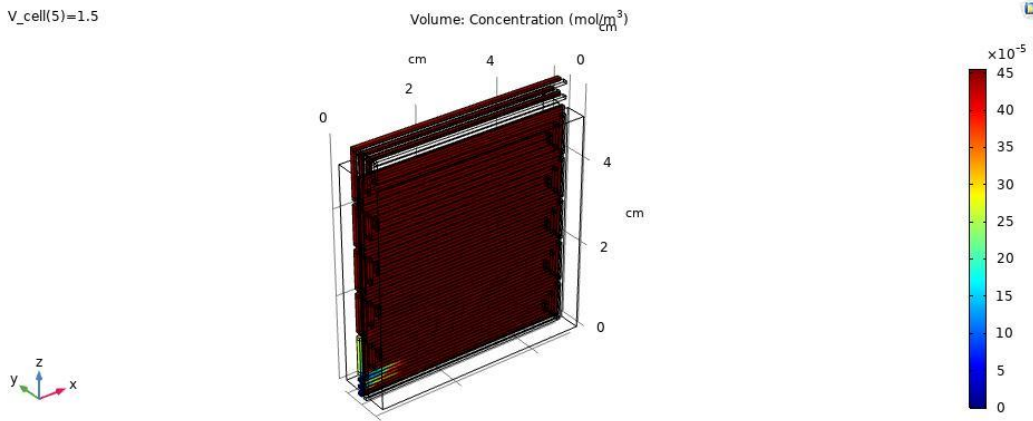


Figure 4. 47 Oxygen concentration in turbulent flow model

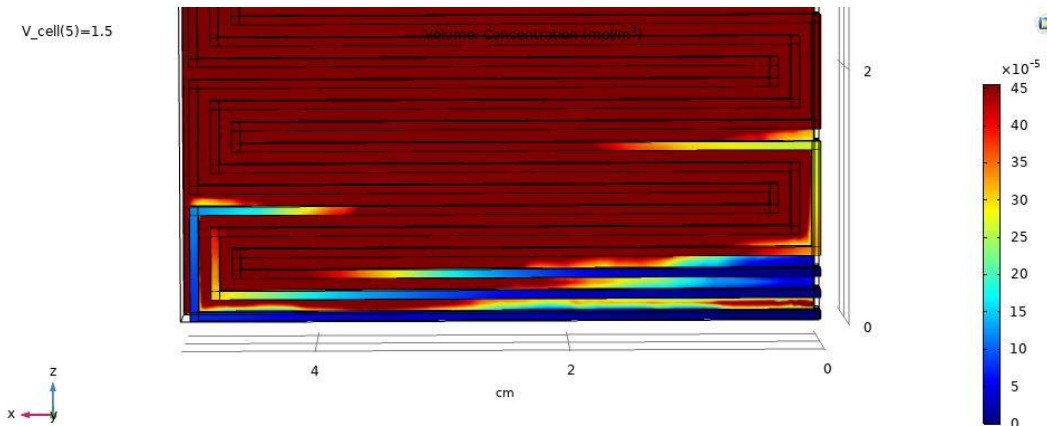


Figure 4. 48 Oxygen concentration in turbulent flow model, inlet closeup

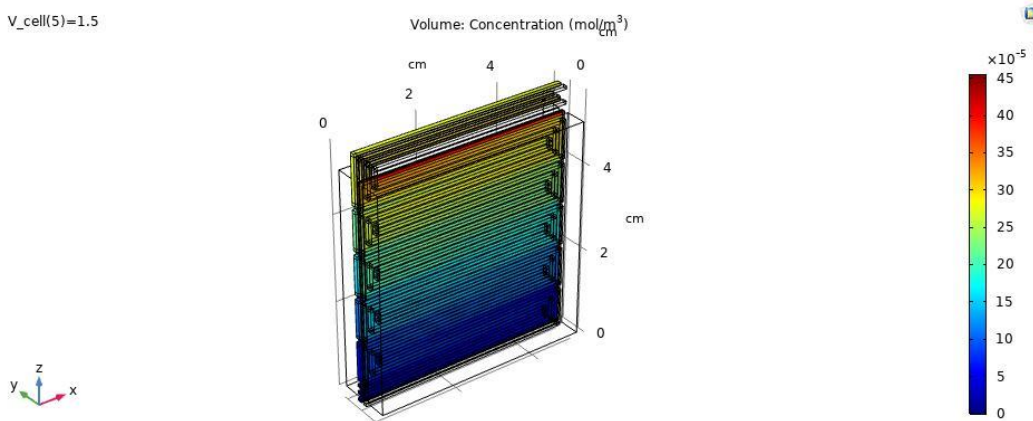


Figure 4. 49 Oxygen concentration in laminar flow model

The turbulent concentration of oxygen has a different distribution in the anodic channel from the laminar flow one: is more uniform and presents different values of concentration at the anode inlet (figure 4.48) caused by the turbulent flow and increase of velocity.

Results

Overall, the concentration of O_2 is higher trough the anodic channel, respect to the laminar model, even if at the interface with the electrolyte (figure 4.50) the concentration has the same trend, when in function of the channel height.

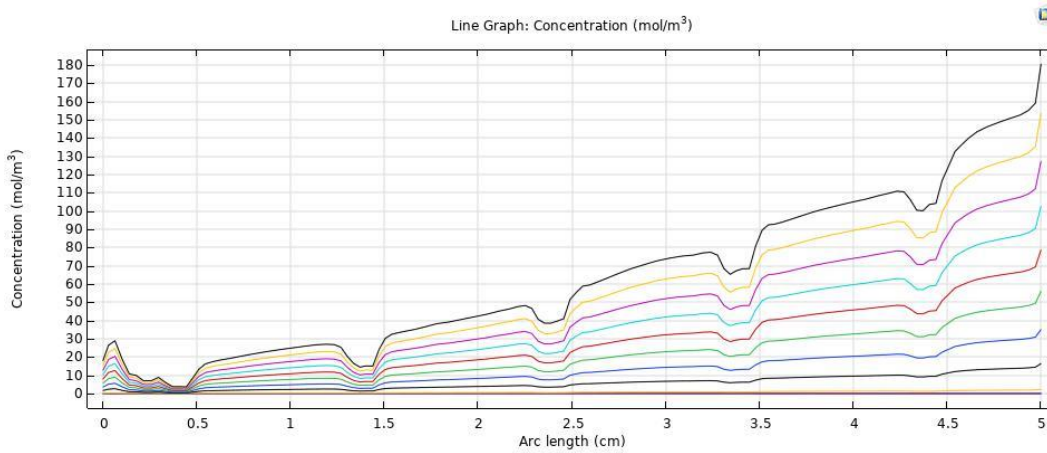


Figure 4. 50 Oxygen concentration at interface, in function of arch length

A similar trend can be observed for the water concentration in the anodic channel:

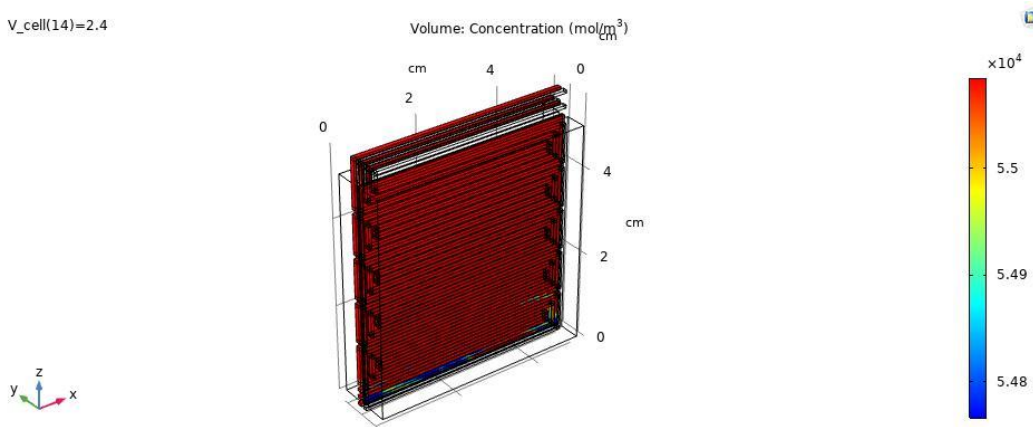


Figure 4. 51 Water concentration at anode, turbulent flow model

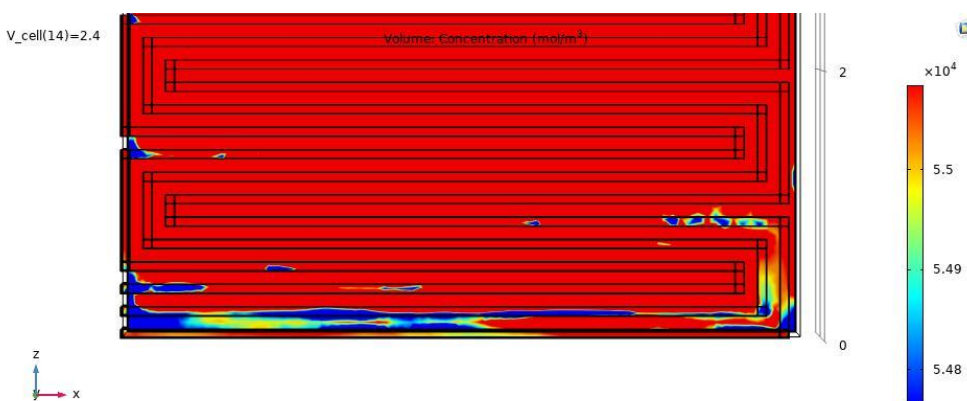


Figure 4. 52 Water concentration at anode, turbulent flow model, inlet closeup

Results

Again, at the anode inlet more spread value of water are evidenced.

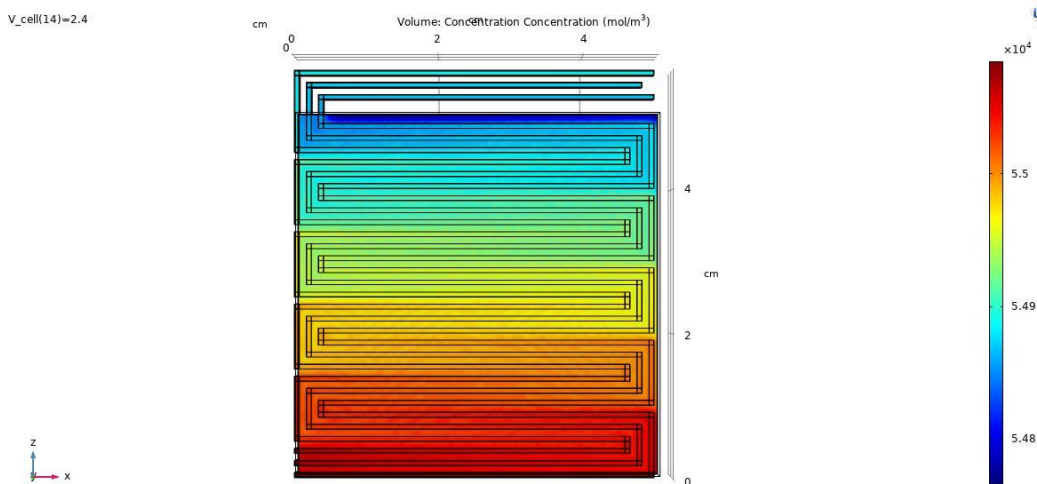


Figure 4. 53 Water concentration at anode, laminar flow model

Respect to the laminar flow model, as for the oxygen concentration, the turbulent flow one has a more uniform water concentration, except for the inlet, where the presence of turbulences and vorticity is higher.

However, the most interesting value is the difference in the concentration of hydrogen:

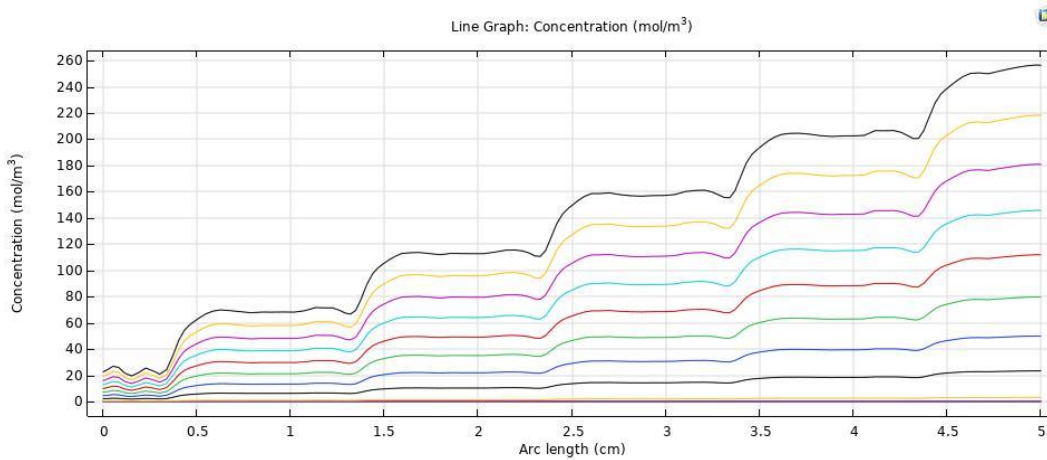


Figure 4. 54 Hydrogen concentration at cathode/membrane interface, turbulent flow model

Results

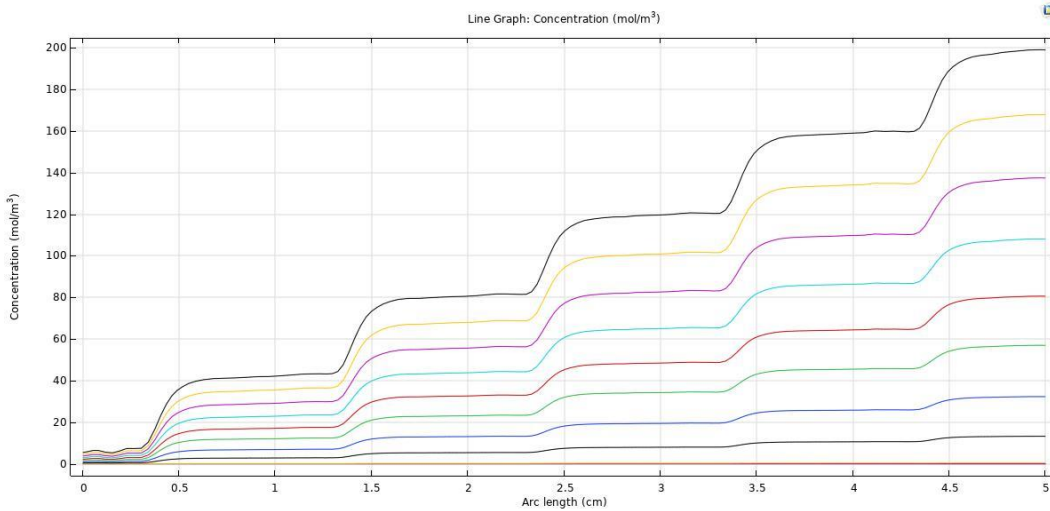


Figure 4. 55 Hydrogen concentration at cathode/membrane interface, laminar flow model

In the Turbulent configuration the hydrogen concentration is 30 % more.

This can be due to the rise of turbulent kinetic energy at the electrode/electrolyte interface which speeds up the electrolysis reaction:

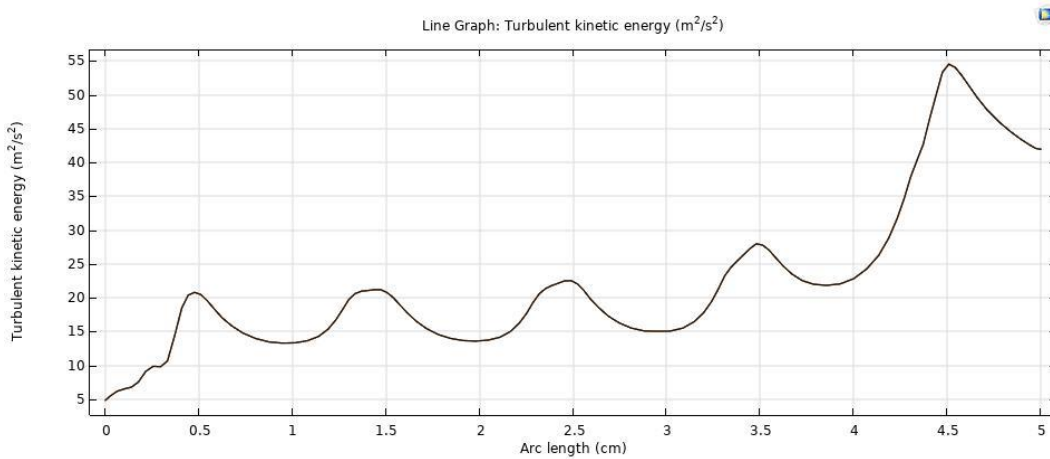


Figure 4. 56 Turbulent kinetic energy distribution at interface, in function of arch length

Results

4.6 3D Laminar Flow Model Open/Closed Cathode Comparison

In this subchapter the main differences between the open cathode configuration and closed cathode one are analysed.

In the closed cathode configuration, as discussed in the experimental part, the water cathode inlet is closed, to have higher temperature and better electrolysis performance.

As seen in subchapter 2.3.1, the results expected in the closed cathode model are:

- Temperature increased, due to lack of water at cathode side
- Mass flow of hydrogen increased, since high temperatures lower the potential needed to break the water molecule
- Resistance decreases since an increase in temperature favours the molecular collisions between ions of the electrolyte.

First result reported is the difference in water concentration at cathode in the two models:

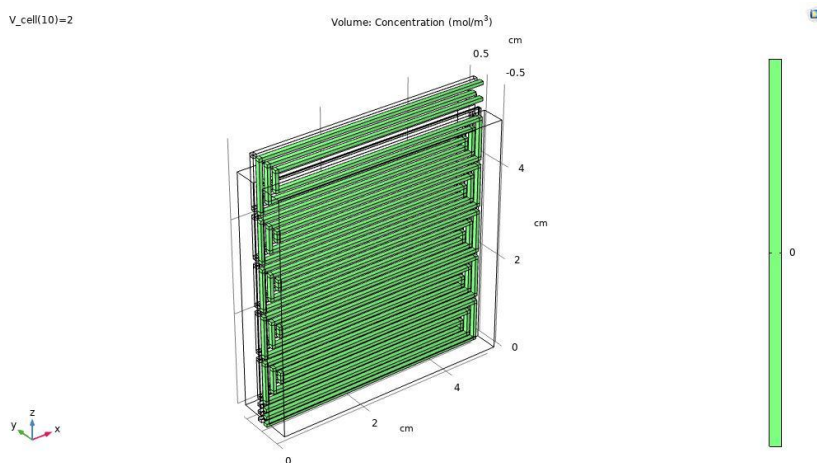


Figure 4. 57 Water concentration at cathode, closed cathode configuration

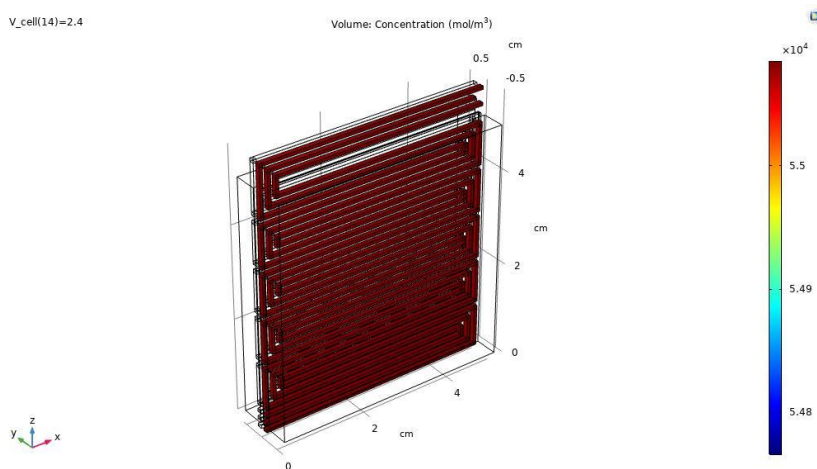


Figure 4. 58 Water concentration at cathode, open cathode configuration

Results

Water concentration is zero at the cathode side, in closed cathode model.

The temperature distribution is now shown:

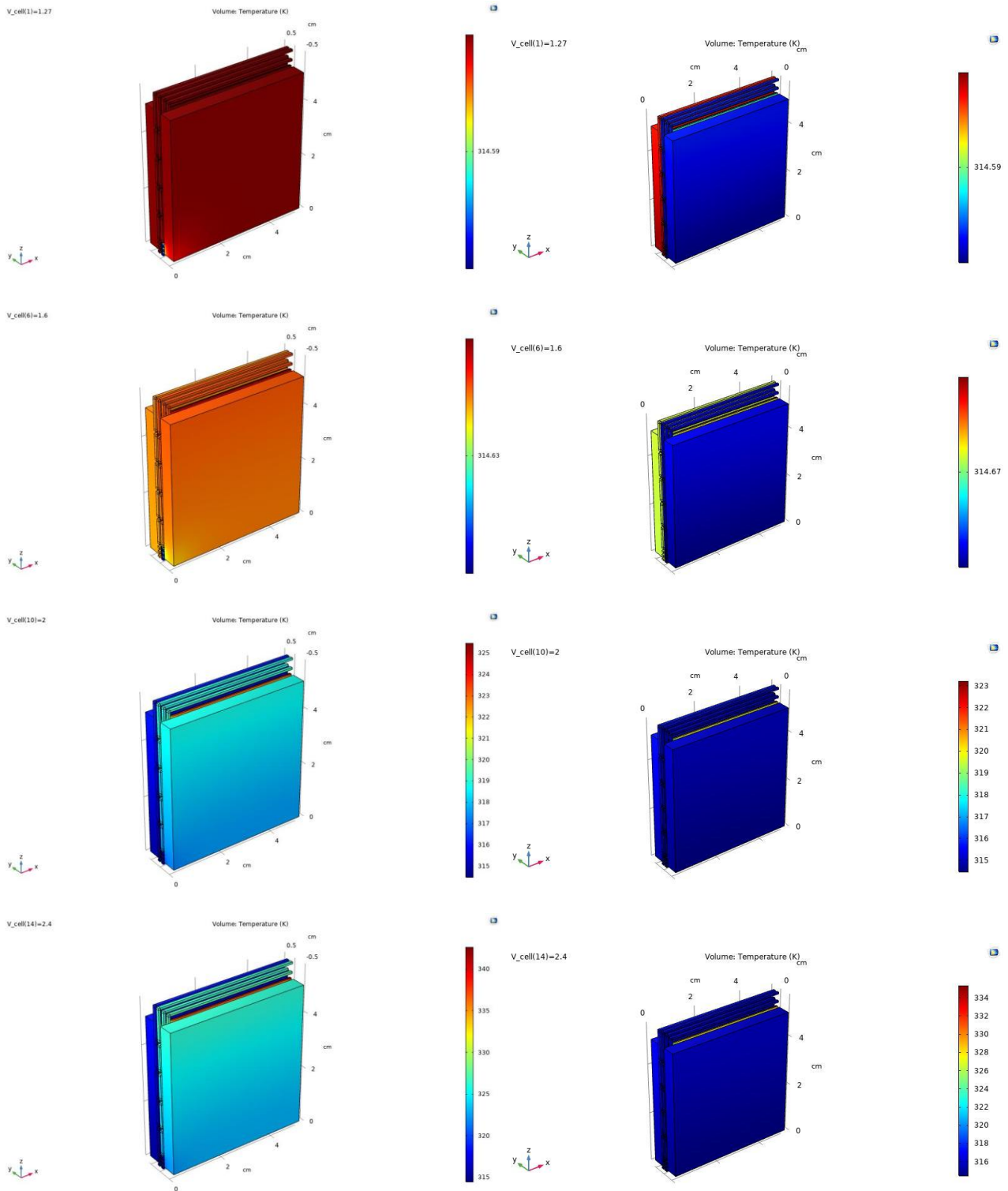


Figure 4.59 Temperature distribution in closed cathode configuration (left) and open (right). Value of voltages, from top to bottom, for each row: 1,27 - 1,6 - 2 - 2,4 V

Results

As expected, the different water concentration at cathode side, whose use is to cool the cell, result in a higher cell temperature in closed cathode configuration, with maximum average temperature difference of $\Delta T = 10^\circ C$ for higher values of voltage.

At interfaces, the temperature is the sequent:

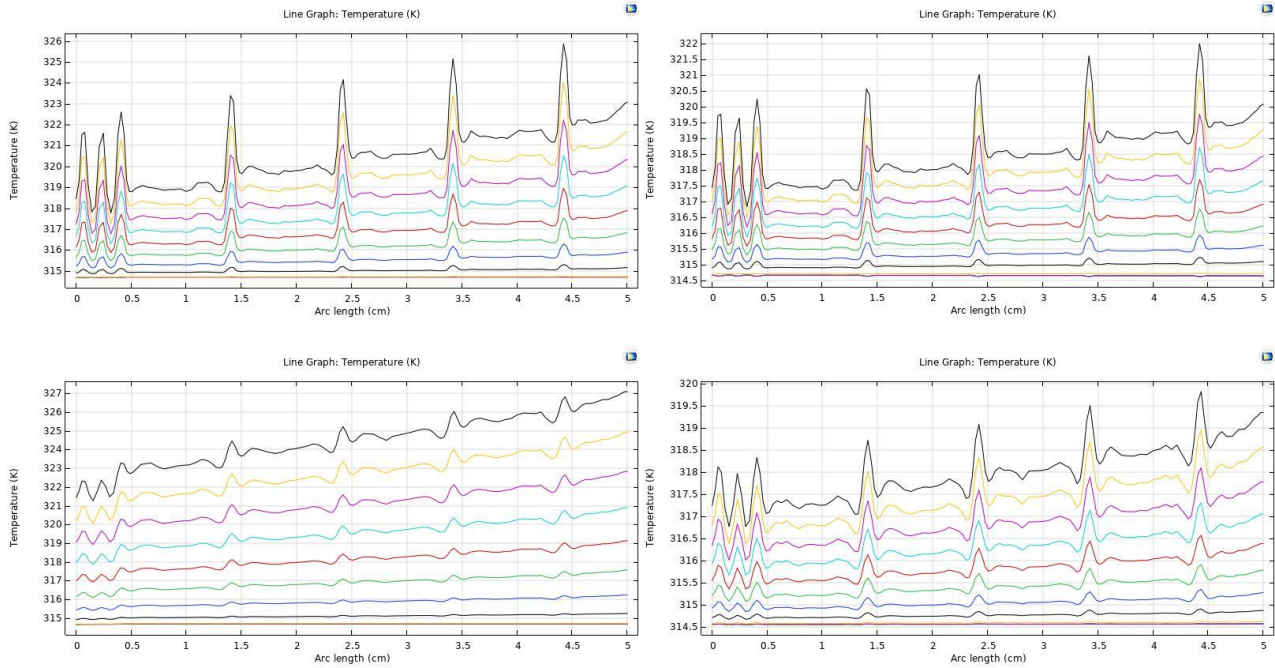


Figure 4. 60 Temperature at interfaces. Left column, closed cathode configuration, right column open one. Top row, temperature at anode/membrane interface, bottom cathode/membrane

In figure 4. 60 the temperature trend can be observed clearer. From the plot comparison, a temperature difference of about $\Delta T = 4^\circ C$ at anode/electrolyte interface is shown, between the open and closed cathode configuration, while in the cathode/electrolyte one differences is of about $\Delta T = 7^\circ C$ for higher value of voltages.

Results

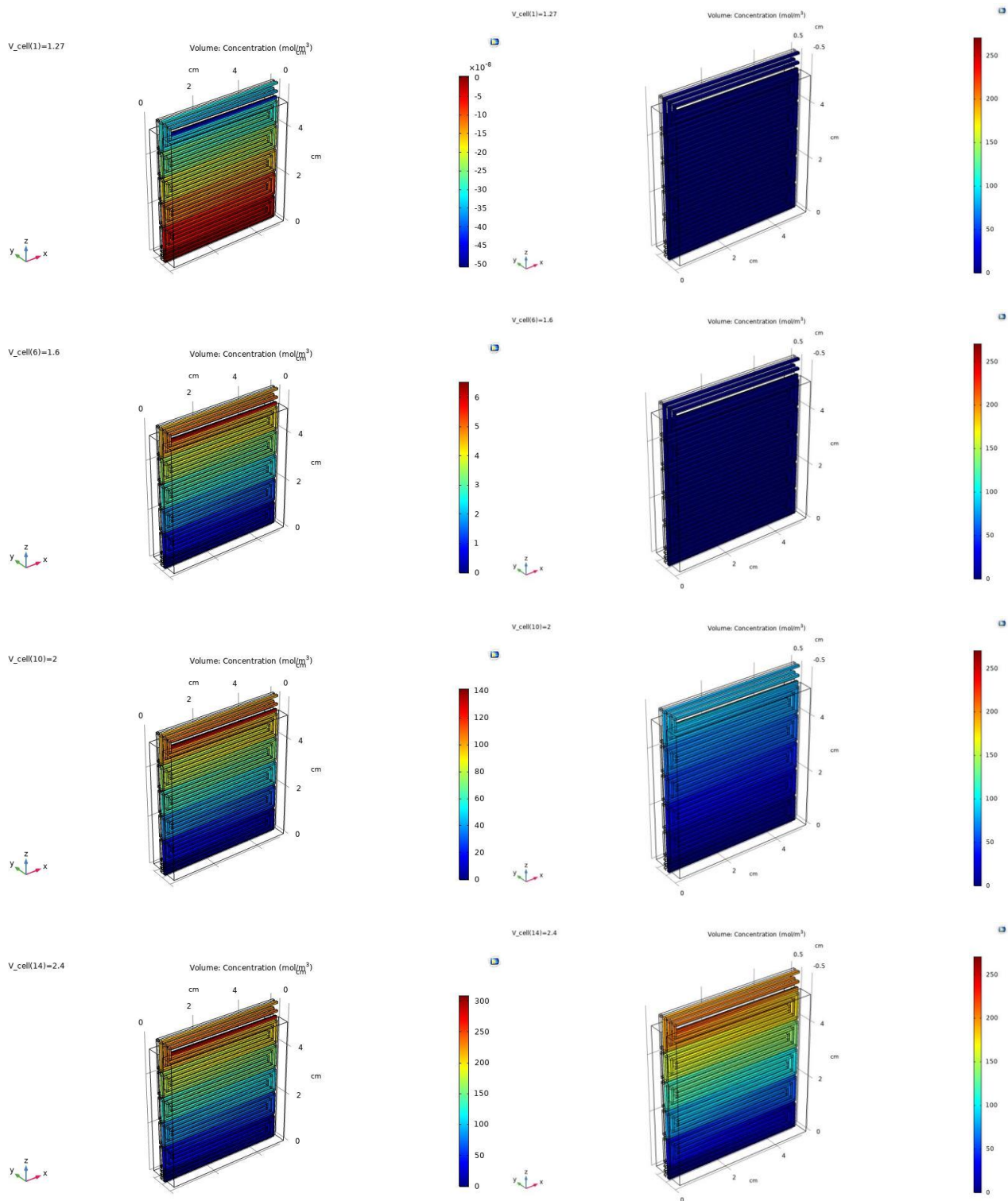


Figure 4.61 Hydrogen concentration in closed cathode configuration (left) and open (right). Value of voltages, from top to bottom, for each row: 1,27 - 1,6 - 2 - 2,4 V

In figure 4.60 the hydrogen concentration in cathode channels is shown.

Overall, the concentration is higher in the closed cathode configuration, again as anticipated.

A better view is proposed below analysing the concentration distribution at cathode/membrane interface in function of the z-coordinate, the height of the cathode channel:

Results

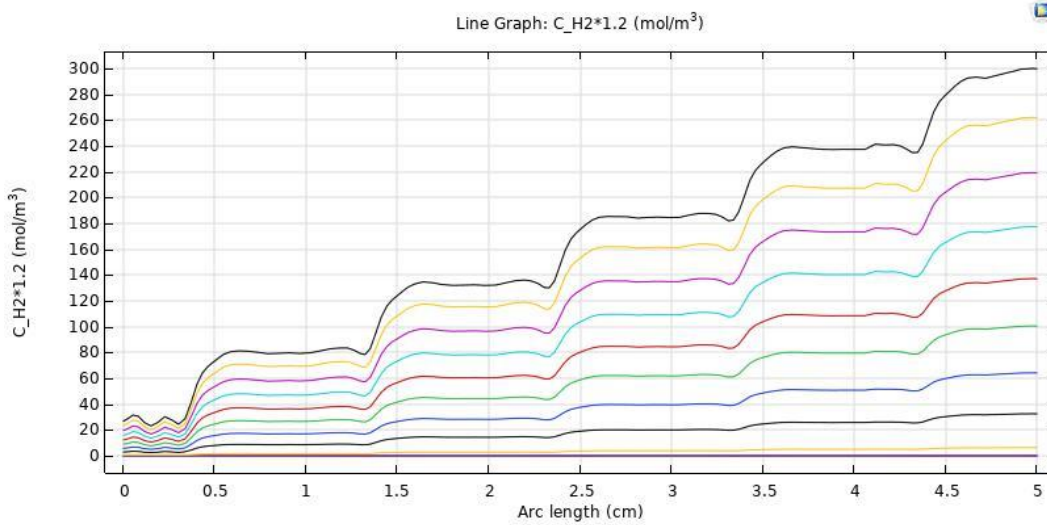


Figure 4. 62 Hydrogen concentration at electrode/electrolyte interface, closed cathode configuration

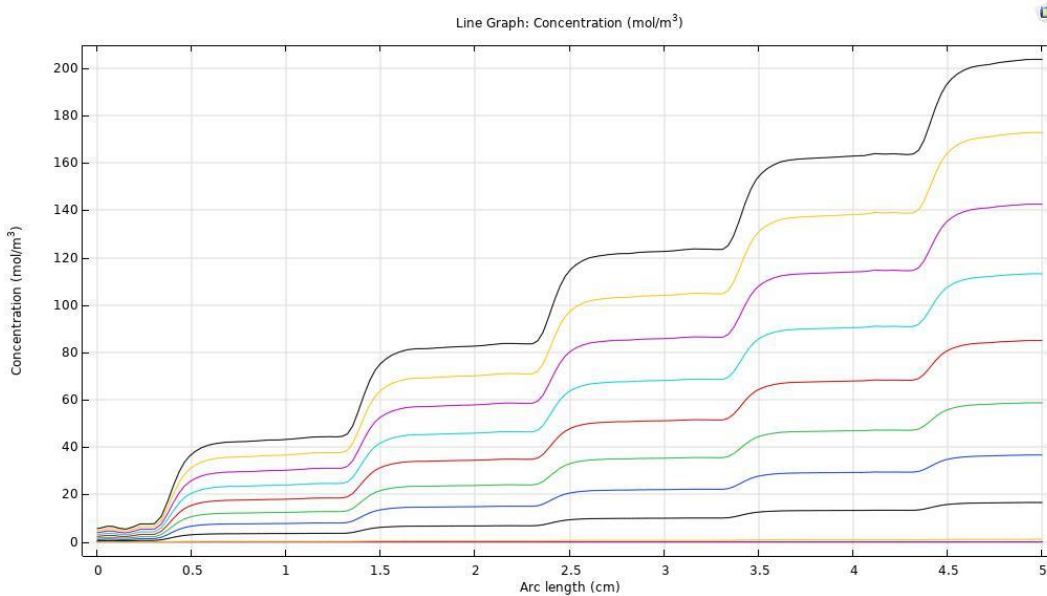


Figure 4. 63 Hydrogen concentration at electrode/electrolyte interface, open cathode configuration

The hydrogen concentration is higher of values between 50 % and 60 % in closed cathode configuration since the temperature rises favours the electrolysis, fastening the breaking of the water molecule.

Results

Lastly, some differences can be noticed in the polarization curve as well:

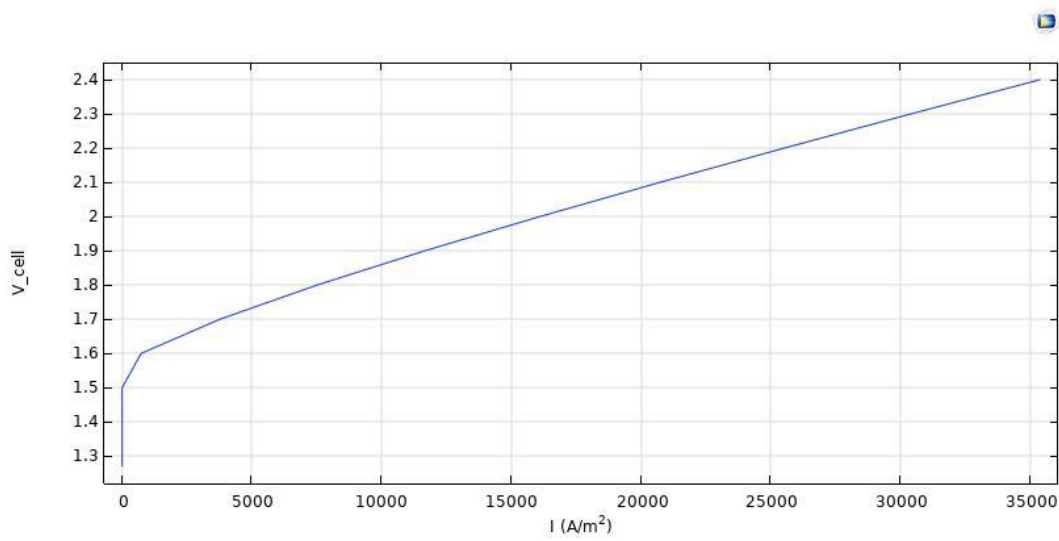


Figure 4.64 Polarization curve, closed cathode configuration, $T = 60^\circ\text{C}$, relative pressure = 0.5 bar

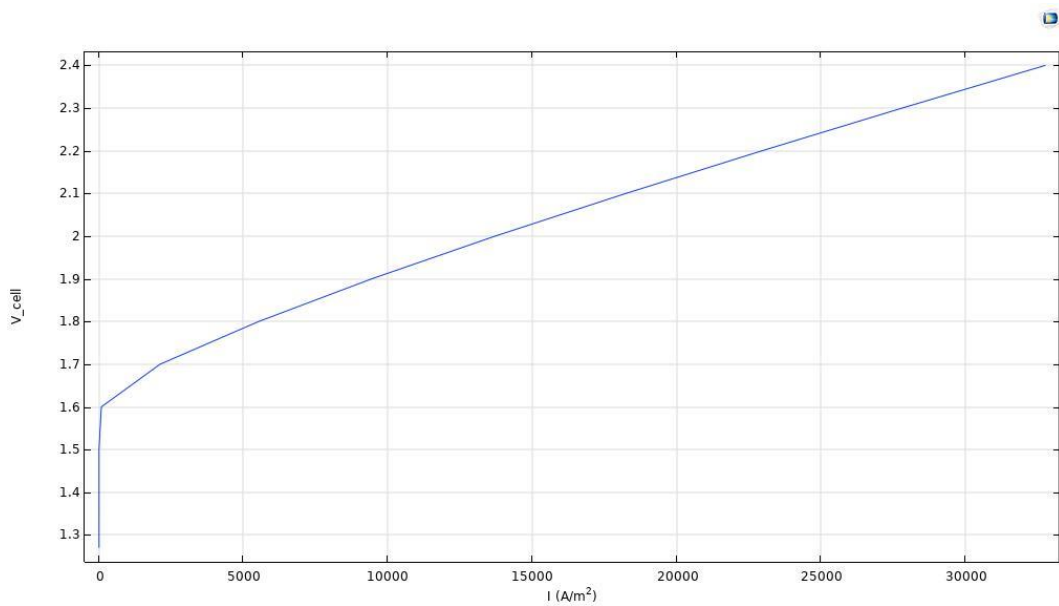


Figure 4.65 Polarization curve, open cathode configuration, $T = 60^\circ\text{C}$, relative pressure = 0.5 bar

For same values of voltages input, higher current density is reached, this is due to the decrease in resistance mentioned above.

Conclusions

The objective of this thesis is to highlight the possibilities of the green hydrogen production through electrolysis using different approaches: experimental and modelling.

In the introduction, the need to accelerate the research on renewable energies due to the imminent global phenomenon represented by climate change is highlighted.

In the literature review, hydrogen is presented as one of the main protagonists in the storage of renewable energies, calling attention to the fact that at the moment the production of hydrogen from renewable sources is very limited. The technology used to produce green hydrogen is represented by the electrolyzer, and after a comparison between the different types, PEM electrolysis is deepened, focusing on the main parameters that influence the reactions inside the cell.

Subsequently, a review on the different types of flow, turbulent and laminar is introduced, with focus on multiphase flow and how the presence of bubbles in a fluid can modify the performance of an electrolyzer.

The experimental work contained in this thesis was carried out entirely at Environment Park, and under collaboration with the Polytechnic of Turin consisting of two parts: preliminary tests on the cell, and degradation test. Preliminary tests were aimed to obtain the polarization curves. In particular attention was paid on the different configuration of open and closed cathode, with different values of operating temperatures and pressures.

The degradation test aimed to report the degradation of the main parameters after several days of non-stop operation. My task during the duration of the test was to supervise the correct functioning of the mass spectrometer and to analyse the data, using Excel and Matlab, in order to obtain satisfactory and comparable data. The main results of this analysis have shown the correct progress of the experiment, as can be seen from the comparisons between the graphs of the percentage of hydrogen, voltage, pressure at cathode side, and discharge of the water tank. It can also be seen in the comparison between the first and last days of degradation test, where a significant decrease in the percentage of hydrogen stands out.

In the modelling section, all the various equations used in the model building are presented. The equations have been divided by physics, inserting through appropriate references assumptions that have been made and the boundary conditions related to each interface.

The main results are related to the in-depth work that is done on the 3D model. The models are validated with the data from the polarization curves obtained in the laboratory. The main parameters have been analysed for the 2D and 3D models. The 2D model is certainly offered to a simpler simulation, as the highly simplified geometry allows the use of more complex interfaces and conditions due to the limited computing power available.

In the 2D model the results concern the laminar single-phase and turbulent multiphase flow, while in the 3D model the laminar single-phase and turbulent single-phase flow, and the open/closed cathode comparison.

In the laminar flow the reported results in the 2D model are the polarization curve, hydrogen and oxygen concentration, water concentration, with analysis on the water in the membrane and its main

concentration factors, potential at the electrodes and at the membrane, local current at the electrodes, temperature distribution, and temperature gradients at anode and cathode.

The main results in the 2D multiphase model are related to the application of the bubbly flow interface in the anode channel and focusing on the parameters arising from having a gas and liquid phase in the same domain. Therefore, the velocities of gaseous and liquid phases, fraction of gaseous volume with respect to the liquid, which is therefore the percentage of volume occupied by bubbles, and the overpotential caused by bubbles are the most important results as they highlight the influence of multiphase flow in an electrolysis process.

In the 3D model the reported results, in addition to those reported for the laminar model in 2D, are focused on the comparison between laminar/turbulent model, and open/closed cathode configuration.

In the 3D turbulent model analysis, the main turbulence variables are presented, such as turbulent kinetic energy, specific dissipation rate and turbulent dynamic viscosity.

The differences with the 3D laminar model are in the different distribution of the velocity field and vorticity in the anodic channels, where the turbulent flow was applied. In the different concentrations of water, oxygen and hydrogen, an important result is that in the turbulent model the concentration of hydrogen as a function of channel height is increased compared to the laminar model, due to the increase and distribution of turbulent kinetic energy at the interface.

Regarding the difference between open/closed cathode configuration, the most important results are in the validation of the assumptions made, namely that a closed cathode configuration, without water in the cathode channels, leads to an increase in temperature due to the absence of cooling fluid, and as a consequence a rise in the production of hydrogen (substantial increase in concentration) and the polarization of the cell.

Possible improvements of this work concern the experimental and modelling part.

Regarding the experimental part, suggestion is building an automatic refilling system, to avoid manual refills during long degradation tests, as well as having a system to control and monitor the pressure in the connection between the mass spectrometer and the rig, to avoid high pressures that cause an interruption of the scan with relative data loss until a new scan is manually performed.

In terms of modelling, a possible improvement would be to deepen the turbulent motion applied to 2D and 3D models in order to gain a better understanding of the multiphase processes present in the cell and considering applying multiphase models to 3D closed cathode configuration.

Bibliography

- [1] 2017 Ipcch, “Global Warming of 1.5 oC,” 2017.
- [2] Enelgreenpower.com, “The climate crisis: the causes, the effects and the solutions” Nov. 25, 2020. “The climate crisis: the causes, the effects and the solutions,” (accessed Feb. 20, 2022).
- [3] McKinsey’s Global Energy Perspective 2019, “Global energy demand Electricity demand/supply Gas demand Oil demand Carbon emissions.”
- [4] Irena, “Renewable Power: Sharply falling generation costs.”
- [5] Rona Rita David, “Renewable Hydrogen: Driver of Green Revolution in Europe?”, *Energy Industry Review*, Aug. 11, 2021.
- [6] Massimiliano Della Pietra, Stephen McPhail, Luca Turchetti, and Giulia Monteleone, “I ‘colori’ dell’idrogeno nella transizione energetica,” *Dipartimento Tecnologie Energetiche e Fonti Rinnovabili, ENEA*, 2020.
- [7] Cheranna Energy, “Hydrogen” Jun. 14, 2021. <https://cherannaenergy.com/hydrogen/> (accessed Feb. 20, 2022).
- [8] F. M. Sapountzi, J. M. Gracia, C. J. (Kees J. Weststrate, H. O. A. Fredriksson, and J. W. (Hans) Niemantsverdriet, “Electrocatalysts for the generation of hydrogen, oxygen and synthesis gas,” *Progress in Energy and Combustion Science*, vol. 58. Elsevier Ltd, pp. 1–35, Jan. 01, 2017. doi: 10.1016/j.pecs.2016.09.001.
- [9] J. Koponen, “Degree Programme in Electrical Engineering Review of water electrolysis technologies and design of renewable hydrogen production systems Examiners: Professor Jero Ahola Associate professor Antti Kosonen.”
- [10] Trasatti S, “Water electrolysis: who first?,” *Journal of Electroanalytical Chemistry*, Oct. 1999.
- [11] Alfredo Ursua; Luis M. Gandia; Pablo Sanchis, “Hydrogen Production From Water Electrolysis: Current Status and Future Trends,” *Proceedings of the IEEE*, vol. 100, no. 2, 2012.
- [12] E. B. J. H. S. H. Schroder V, “Explosion limits of hydrogen/oxygen mixtures at initial pressures up to 200 bar,” *Chemical Engineering & Technology*, 2004.
- [13] E. E. W. Dönitz, “High-temperature electrolysis of water vapor—status of development and perspectives for application,” *International Journal of Hydrogen Energy*, 1985.
- [14] Grubb WT, “Ionic migration in ion-exchange membranes,” *Journal of Physical Chemistry*, 1963.
- [15] Barbir F., “PEM electrolysis for production of hydrogen from renewable energy sources,” *Solar Energy*, vol. 78, 2005.
- [16] K. E. Ayers *et al.*, “Pathways to ultra-low platinum group metal catalyst loading in proton exchange membrane electrolyzers,” *Catalysis Today*, vol. 262, pp. 121–132, Mar. 2016, doi: 10.1016/J.CATTOD.2015.10.019.
- [17] K. Sugarman, “Hydrogen Through Electrolysis,” *Ocean Geothermal Energy Foundation*, Sep. 2016.
- [18] Massimo Santarelli, “Slide from PAES course.” 2020.

Bibliography

- [19] F. Marangio, M. Pagani, M. Santarelli, and M. Cali, "Concept of a high pressure PEM electrolyzer prototype," *International Journal of Hydrogen Energy*, vol. 36, no. 13, pp. 7807–7815, Jul. 2011, doi: 10.1016/j.ijhydene.2011.01.091.
- [20] R. García-Valverde, N. Espinosa, and A. Urbina, "Simple PEM water electrolyzer model and experimental validation," in *International Journal of Hydrogen Energy*, Jan. 2012, vol. 37, no. 2, pp. 1927–1938. doi: 10.1016/j.ijhydene.2011.09.027.
- [21] M. E. Lebbal and S. Lecœuche, "Identification and monitoring of a PEM electrolyzer based on dynamical modelling," *International Journal of Hydrogen Energy*, vol. 34, no. 14, pp. 5992–5999, Jul. 2009, doi: 10.1016/J.IJHYDENE.2009.02.003.
- [22] Z. Liang, M. A. Ioannidis, and I. Chatzis, "Permeability and electrical conductivity of porous media from 3D stochastic replicas of the microstructure."
- [23] P. Choi, N. H. Jalani, and R. Datta, "Thermodynamics and Proton Transport in Nafion," *Journal of The Electrochemical Society*, vol. 152, no. 3, p. E123, 2005, doi: 10.1149/1.1859814.
- [24] "File:PEM electrolysis loss breakdown.pdf - Wikipedia." https://en.wikipedia.org/wiki/File:PEM_electrolysis_loss_breakdown.pdf (accessed Feb. 21, 2022).
- [25] A. Alanazi, E. Ogungbemi, A. Wilberforce, O. S. Ijaodola, P. Vichare, and A.-G. Olabi, "State-of-the-Art Manufacturing Technologies of PEMFC Components," Jul. 2017, pp. 189–198. doi: 10.18690/978-961-286-054-7.17.
- [26] J. Mališ, P. Mazúr, M. Paidar, T. Bystron, and K. Bouzek, "Nafion 117 stability under conditions of PEM water electrolysis at elevated temperature and pressure," *International Journal of Hydrogen Energy*, vol. 41, no. 4, pp. 2177–2188, Jan. 2016, doi: 10.1016/j.ijhydene.2015.11.102.
- [27] M. Carmo, D. L. Fritz, J. Mergel, and D. Stolten, "A comprehensive review on PEM water electrolysis," *International Journal of Hydrogen Energy*, vol. 38, no. 12, pp. 4901–4934, Apr. 22, 2013. doi: 10.1016/j.ijhydene.2013.01.151.
- [28] P. Millet, S. A. Grigoriev, and V. I. Porembskiy, "Development and characterisation of a pressurized PEM bi-stack electrolyzer," *International Journal of Energy Research*, vol. 37, no. 5, pp. 449–456, Apr. 2013, doi: 10.1002/er.2916.
- [29] S. A. Grigoriev, P. Millet, S. A. Volobuev, and V. N. Fateev, "Optimization of porous current collectors for PEM water electrolyzers," *International Journal of Hydrogen Energy*, vol. 34, no. 11, pp. 4968–4973, Jun. 2009, doi: 10.1016/j.ijhydene.2008.11.056.
- [30] P. Millet, R. Ngameni, S. A. Grigoriev, and V. N. Fateev, "Scientific and engineering issues related to PEM technology: Water electrolyzers, fuel cells and unitized regenerative systems," 2010, doi: 10.1016/j.ijhydene.2010.06.106.
- [31] J. O. Majasan, J. I. S. Cho, I. Dedigama, D. Tsaoulidis, P. Shearing, and D. J. L. Brett, "Two-phase flow behaviour and performance of polymer electrolyte membrane electrolyzers: Electrochemical and optical characterisation," *International Journal of Hydrogen Energy*, vol. 43, no. 33, pp. 15659–15672, Aug. 2018, doi: 10.1016/j.ijhydene.2018.07.003.
- [32] S. Siracusano, V. Baglio, F. Lufrano, P. Staiti, and A. S. Aricò, "Electrochemical characterization of a PEM water electrolyzer based on a sulfonated polysulfone membrane," *Journal of Membrane Science*, vol. 448, pp. 209–214, Dec. 2013, doi: 10.1016/J.MEMSCI.2013.07.058.
- [33] S. P. S Badwal S Giddey F T Ciacchi, "Hydrogen and oxygen generation with polymer electrolyte membrane (PEM)-based electrolytic technology," *Ionics*, vol. 12, pp. 7–14, 2006, doi: 10.1007/s11581-006-0002-x.

Bibliography

- [34] S. Shiva Kumar et al, “Phosphorus-doped graphene supported palladium (Pd/PG) electrocatalyst for the hydrogen evolution reaction in PEM water electrolysis,” Aug. 2018.
- [35] S. Trasatti and G. Buzzanca, “Ruthenium dioxide: A new interesting electrode material. Solid state structure and electrochemical behaviour,” *Journal of Electroanalytical Chemistry and Interfacial Electrochemistry*, vol. 29, no. 2, pp. A1–A5, Feb. 1971, doi: 10.1016/S0022-0728(71)80111-0.
- [36] X. Sun *et al.*, “A study of strain-rate effect and fiber reinforcement effect on dynamic behavior of steel fiber-reinforced concrete,” *Construction and Building Materials*, vol. 158, pp. 657–669, Jan. 2018, doi: 10.1016/J.CONBUILDMAT.2017.09.093.
- [37] “What is Turbulent Flow? Computational Fluid Dynamics | SimScale.” <https://www.simscale.com/docs/simwiki/cfd-computational-fluid-dynamics/what-is-turbulent-flow/> (accessed Feb. 21, 2022).
- [38] “Laminar v turbulent - Questions and Answers in MRI.” <https://mriquestions.com/laminar-v-turbulent.html> (accessed Feb. 21, 2022).
- [39] F. M. White, “Fluid mechanics,” p. 862, 2011.
- [40] “What is Turbulent Flow - Definition.” <https://www.thermal-engineering.org/what-is-turbulent-flow-definition/> (accessed Feb. 21, 2022).
- [41] C. E. (Christopher E. Brennen, “Fundamentals of multiphase flow,” p. 345, 2005.
- [42] “Two-phase flow”, Hewitt. 1961
- [43] P. B. Whalley, “Boiling, condensation, and gas-liquid flow,” p. 291, 1987.
- [44] D. Barnea, O. Shoham, Y. Taitel, and A. E. Dukler, “Flow pattern transition for gas-liquid flow in horizontal and inclined pipes. Comparison of experimental data with theory,” *International Journal of Multiphase Flow*, vol. 6, no. 3, pp. 217–225, Jun. 1980, doi: 10.1016/0301-9322(80)90012-9.
- [45] J. Mo, Z. Kang, G. Yang, W. Barnhill, F. Y. Zhang, and D. Talley, “Visualization on rapid and micro-scale dynamics of oxygen bubble evolution in PEMECs,” *2017 IEEE 12th International Conference on Nano/Micro Engineered and Molecular Systems, NEMS 2017*, pp. 101–105, Aug. 2017, doi: 10.1109/NEMS.2017.8016983.
- [46] Y. Li *et al.*, “In-situ investigation of bubble dynamics and two-phase flow in proton exchange membrane electrolyzer cells,” *International Journal of Hydrogen Energy*, vol. 43, no. 24, pp. 11223–11233, Jun. 2018, doi: 10.1016/J.IJHYDENE.2018.05.006.
- [47] M. Li, K. Duan, N. Djilali, and P. C. Sui, “Flow sharing and turbulence phenomena in proton exchange membrane fuel cell stack headers,” *International Journal of Hydrogen Energy*, vol. 44, no. 57, pp. 30306–30318, Nov. 2019, doi: 10.1016/J.IJHYDENE.2019.09.140.
- [48] “Home page - Environment Park.” <https://www.envipark.com/> (accessed Feb. 21, 2022).
- [49] “Hiden HPR-20 QIC R&D for Advanced Research.” [Online]. Available: www.HidenAnalytical.com
- [50] “MASsoft Professional Version 7 Training Manual.”
- [51] “Electrochemical Systems - John Newman, Karen E. Thomas-Alyea - Google Libri.” <https://books.google.it/books?hl=it&lr=&id=eyj4MRa7vLAC&oi=fnd&pg=PR3&dq=J.+Newman+and+K.+Thomas-Alyea,+%E2%80%9CElectrochemical+Systems%E2%80%9D&ots=QjE99V2yGs&sig=Tzmt4FkW Nbn8avIMe6T9fLx4roI#v=onepage&q=J.%20Newman%20and%20K.%20Thomas-Alyea%2C%20%E2%80%9CElectrochemical%20Systems%E2%80%9D&f=false> (accessed Feb. 23, 2022).

Bibliography

- [52] E. N. Fuller, P. D. Schettler, and J. C. Giddings, “An easily applied method for predicting binary gas-phase diffusivities is based on the use of special diffusion volumes coupled with extensive experiment and nonlinear least squares analysis of the data. Comparison with eight other correlations demonstrates the relative reliability and simplicity of the new method. A NEW METHOD FOR PREDICTION OF BINARY GAS-PHASE DIFFUSION COEFFICIENTS.”
- [53] R. S. Brokaw, “Approximate Formulas for the Viscosity and Thermal Conductivity of Gas Mixtures. II,” *The Journal of Chemical Physics*, vol. 42, no. 4, p. 1140, Jul. 2004, doi: 10.1063/1.1696093.
- [54] H.-J. Kretzschmar, W. Wagner, and W. Wagner, *International steam tables : properties of water and steam based on the industrial formulation IAPWS-IF97 : tables, algorithms, and diagrams : all of the equations of IAPWS-IF97 including a complete*, 3rd edition. Berlin Germany: Springer Vieweg, 2019.
- [55] M. W. Chase, “NIST-JANAF Thermochemical Tables for Oxygen Fluorides,” *Journal of Physical and Chemical Reference Data*, vol. 25, no. 2, p. 551, Oct. 2009, doi: 10.1063/1.555992.
- [56] D. Ferrero and M. Santarelli, “Investigation of a novel concept for hydrogen production by PEM water electrolysis integrated with multi-junction solar cells,” *Energy Conversion and Management*, vol. 148, pp. 16–29, Sep. 2017, doi: 10.1016/J.ENCONMAN.2017.05.059.
- [57] D. A. G. Bruggeman, “Berechnung verschiedener physikalischer Konstanten von heterogenen Substanzen. I. Dielektrizitätskonstanten und Leitfähigkeiten der Mischkörper aus isotropen Substanzen,” *Annalen der Physik*, vol. 416, no. 7, pp. 636–664, 1935, doi: 10.1002/andp.19354160705.
- [58] M. le BARS and M. G. WORSTER, “Interfacial conditions between a pure fluid and a porous medium: implications for binary alloy solidification,” *Journal of Fluid Mechanics*, vol. 550, no. 1, p. 149, Feb. 2006, doi: 10.1017/S0022112005007998.
- [59] F. R. Menter, “Two-equation eddy-viscosity turbulence models for engineering applications,” *AIAA Journal*, vol. 32, no. 8, pp. 1598–1605, Aug. 1994, doi: 10.2514/3.12149.
- [60] R. Codina, “A discontinuity-capturing crosswind-dissipation for the finite element solution of the convection-diffusion equation,” *Computer Methods in Applied Mechanics and Engineering*, vol. 110, no. 3–4, pp. 325–342, Dec. 1993, doi: 10.1016/0045-7825(93)90213-H.
- [61] P. v. Danckwerts, “Continuous flow systems: Distribution of residence times,” *Chemical Engineering Science*, vol. 2, no. 1, pp. 1–13, Feb. 1953, doi: 10.1016/0009-2509(53)80001-1.
- [62] B. Gurappa, R. P. Chhabra, J. M. (John M. Coulson, and J. F. (John F. Richardson, “Coulson and Richardson’s chemical engineering. Volume 2A, Particulate systems and particle technology”.
- [63] “Transport Processes in Chemically Reacting Flow Systems - Daniel E. Rosner - Google Libri.” https://books.google.it/books?hl=it&lr=&id=CmVw7fn_cKIC&oi=fnd&pg=PP1&dq=Transport+Processes+in+Chemically+Reacting+Flow+Systems&ots=DIXVJZOJuv&sig=SOLC94VpHudcVi2KxjLU4Qi58ec#v=onepage&q=Transport%20Processes%20in%20Chemically%20Reacting%20Flow%20Systems&f=false (accessed Feb. 27, 2022).
- [64] Jacob. Bear, “Dynamics of fluids in porous media,” p. 764.
- [65] R. J. Millington and J. P. Quirk, “Permeability of porous solids,” *Transactions of the Faraday Society*, vol. 57, no. 0, pp. 1200–1207, Jan. 1961, doi: 10.1039/TF9615701200.
- [66] R. B. Bird, “Transport phenomena,” *Applied Mechanics Reviews*, vol. 55, no. 1, pp. R1–R4, Jan. 2002, doi: 10.1115/1.1424298.
- [67] Y. S. Wu, K. Pruess, and P. Persoff, “Gas Flow in Porous Media With Klinkenberg Effects,” *Transport in Porous Media* 1998 32:1, vol. 32, no. 1, pp. 117–137, 1998, doi: 10.1023/A:1006535211684.

Bibliography

- [68] Ö. Akgiray and A. M. Saatçi, “A new look at filter backwash hydraulics,” *Water Science and Technology: Water Supply*, vol. 1, no. 2, pp. 65–72, 2001, doi: 10.2166/WS.2001.0022.
- [69] “Geodynamics - Donald L. Turcotte, Gerald Schubert - Google Libri.” https://books.google.it/books?hl=it&lr=&id=-nCHIVuJ4FoC&oi=fnd&pg=PR11&dq=D.L.+Turcotte+and+G.+Schubert,+Geodynamics&ots=LqUSvXB6UY&sig=am_gqL6RTFITsOlwgB1UjZrAYOU#v=onepage&q=D.L.%20Turcotte%20and%20G.%20Schubert%2C%20Geodynamics&f=false (accessed Feb. 28, 2022).
- [70] N. H. Sleep and K. (Kazuya) Fujita, *Principles of geophysics*. Malden Mass. USA: Blackwell Science, 1997.
- [71] “Groundwater in geologic processes, 2nd edition.” <https://pubs.er.usgs.gov/publication/70178403> (accessed Feb. 28, 2022).
- [72] “Hydraulics of Groundwater - Jacob Bear - Google Libri.” https://books.google.it/books?hl=it&lr=&id=yQogKirZW-MC&oi=fnd&pg=PP1&dq=J.+Bear,+Hydraulics+of+Groundwater&ots=iihe7TSgt0&sig=QdBne_otMYLAwrlxxS4WYW0OLLS#v=onepage&q=J.%20Bear%2C%20Hydraulics%20of%20Groundwater&f=false (accessed Feb. 28, 2022).
- [73] M. A. Badri, P. Jolivet, B. Rousseau, S. le Corre, H. Digonnet, and Y. Favennec, “Vectorial finite elements for solving the radiative transfer equation,” *Journal of Quantitative Spectroscopy and Radiative Transfer*, vol. 212, pp. 59–74, Jun. 2018, doi: 10.1016/J.JQSRT.2018.03.024.
- [74] R. G. Carbonell and S. Whitaker, “Heat and Mass Transfer in Porous Media,” in *Fundamentals of Transport Phenomena in Porous Media*, Dordrecht: Springer Netherlands, 1984, pp. 121–198. doi: 10.1007/978-94-009-6175-3_3.
- [75] D. A. Nield and A. Bejan, *Convection in porous media*. Springer International Publishing, 2017. doi: 10.1007/978-3-319-49562-0.
- [76] D. Lacasse, É. Turgeon, and D. Pelletier, “On the judicious use of the k – ε model, wall functions and adaptivity,” *International Journal of Thermal Sciences*, vol. 43, no. 10, pp. 925–938, Oct. 2004, doi: 10.1016/J.IJTHERMALSCI.2004.03.004.
- [77] D. C. Wilcox, “Formulation of the k - w Turbulence Model Revisited,” *AIAA Journal*, vol. 46, no. 11, pp. 2823–2838, Nov. 2008, doi: 10.2514/1.36541.
- [78] A. Nouri-Khorasani, E. Tabu Ojong, T. Smolinka, and D. P. Wilkinson, “Model of oxygen bubbles and performance impact in the porous transport layer of PEM water electrolysis cells,” *International Journal of Hydrogen Energy*, vol. 42, no. 48, pp. 28665–28680, Nov. 2017, doi: 10.1016/j.ijhydene.2017.09.167.